Levels of the Autophagy Related 5 Protein Affect Progression and Metastasis of Pancreatic Tumors in Mice

Kivanc Görgülü[1], Kalliope N. Diakopoulos[1]*, Jiaoyu Ai[1], Benjamin Schoeps[2], Derya Kabacaoglu[1], Angeliki-Faidra Karpathaki[1], Katrin J. Ciecielski[1], Ezgi Kaya-Aksoy[1], Dietrich A. Ruess[1], Alexandra Berninger[1], Marlena Kowalska[1], Marija Stevanovic[1], Sonja M. Wörmann[1], Thomas Wartmann[3], Yue Zhao[3], Walter Halangk[3], Svetlana Voronina[4], Alexey Tepikin[4], Anna Melissa Schlitter[5], Katja Steiger[5,6], Anna Artati[7], Jerzy Adamski[7, 10, A], Michaela Aichler[8], Axel Walch[8], Martin Jastroch[9], Götz Hartleben[10], Christos S. Mantzoros[11], Wilko Weichert[5], Roland M. Schmid[1], Stephan Herzig[10], Achim Krüger[2], Bruno Sainz Jr[12], Marina Lesina[1*] and Hana Algül[1*]*

[1]Klinik und Poliklinik für Innere Medizin II, Klinikum rechts der Isar, Technische Universität München, Munich, Germany; [2]Institute of Molecular Immunology and Experimental Oncology, Klinikum rechts der Isar, Technische Universität München, Munich, Germany; [3]Klinik für Chirurgie Bereich Experimentelle Operative Medizin, Universitätsklinikum Magdeburg, Magdeburg, Germany; [4]Institute of Translational Medicine, University of Liverpool, Liverpool, UK; [5]Institute of Pathology, Technische Universität München, Munich, Germany and German Cancer Consortium (DKTK), partner site Munich; [6]Comparative Experimental Pathology (CEP) Institute of Pathology, Technische Universität München, Munich, Germany; [7]Institute of Experimental Genetics, Genome Analysis Centre, Helmholtz Zentrum München, Neuherberg, Germany; [8]Research Unit Analytical Pathology, Helmholtz Zentrum München, Neuherberg, Germany; [9]Helmholtz Diabetes Center & German Diabetes Center (DZD), Helmholtz Zentrum München, Neuherberg, Germany; [10]Institute for Diabetes and Cancer, German Center for Diabetes Research (DZD), Neuherberg, Germany; [11]Division of Endocrinology, Diabetes, and Metabolism, Beth Israel Deaconess Medical Centre, Harvard Medical School, Boston, Massachusetts; [12]Department of Biochemistry, School of Medicine, Autónoma University of Madrid, Madrid, Spain and, [A]Lehrstuhl für Experimentelle Genetik, Technische Universität München, 85350 Freising-Weihenstephan, Germany

* Authors contributed equally to this work

SHORT TITLE:

Atg5 levels in pancreatic carcinogenesis

GRANT SUPPORT:

This study was supported in part by the Mildred-Scheel-Professur der Deutschen Krebshilfe 111464, DFG AL 1174/6-1 to H.A., DFG DI 2299/1-1 to K.N.D., DFG SFB1321 (S01) to K.S. and W.W., and the German Federal Ministry of Education and Research to the German Center for Diabetes Research (DZD e.V.) to J.A..

ABBREVIATIONS:

PDAC, Pancreatic Ductal Adenocarcinoma; PanIN, Pancreatic Intraepithelial Neoplasia; Atg5, Autophagy related gene 5; ADM, Acinar-to-Ductal Metaplasia; ER, Endoplasmic Reticulum; OCR, Oxygen Consumption Rate; ECAR, Extracellular Acidification Rate; GLDH, Glutamate Dehydrogenase; CTSB, Cathepsin B; CTSD, Cathepsin D; CTSL, Cathepsin L; NES, Normalized Enrichment Score; ES, Enrichment Score.

CORRESPONDING AUTHORS:

Professor Dr. Hana Algül, MD, MPH.
Klinik und Poliklinik für Innere Medizin II, Klinikum rechts der Isar,
Technische Universität München, 81675 Munich, Germany
Phone: +49-89-4140-5215
Fax: +49-89-4140-7869
Email: hana.alguel@mri.tum.de

Dr. Marina Lesina, PhD
Klinik und Poliklinik für Innere Medizin II, Klinikum rechts der Isar,
Technische Universität München, 81675 Munich, Germany
Phone: +49-89-4140-6792
Fax: +49-89-4140-7869
Email: marina.lesina@tum.de

CONFLICT OF INTEREST DISCLOSURE STATEMENT:

The authors declare no potential conflicts of interest

TRANSCRIPT PROFILING:

Microarray data are available in the ArrayExpress database at EMBL-EBI (https://www.ebi.ac.uk/arrayexpress/) under accession number E-MTAB-6275.

ACKNOWLEDGEMENTS:

The authors thank Gabriele Mettenleiter (electron microscopy), Marion Mielke (IHC), the tissue bank of the Institute of Pathology of the TUM (MTBIO), and Franziska Braun (cathepsin, GLDH-measurements) for technical assistance. The authors want to deeply acknowledge Prof. Walter Halangk, who in the course of the revision of this manuscript passed away. The authors are grateful for his very valuable contribution. Thus, the authors want to dedicate this manuscript to him.

AUTHOR CONTRIBUTIONS:

K.G. and K.N.D. designed and performed experiments, analyzed data, and prepared the manuscript; J.A., M.S., D.K., A.F.K., K.J.C, E.K.A., D.A.R., A.B., M.K., S.M.W., M.L. provided experimental support; B.S. provided *Atg5*-knockdown cell lines; T.W., Y.Z., and W.H. performed cathepsin and GLDH measurements; S.V. and A.T. performed Ca^{2+} measurements; A.M.S., K.S., W.W. supplied human PDAC samples and performed ATG5 scoring; A.A. and J.A. performed metabolomic experiments; M.A. and A.W. performed electron microscopy; M.J. carried out mitochondrial respiratory measurements; G.H. conducted Cyto-ID experiments; A.K., C.S.M, S.H., B.S. Jr., and R.M.S revised the manuscript; H.A. and M.L. designed experiments, analyzed data, and revised the manuscript.

Background and Aims: Cells in pancreatic ductal adenocarcinoma (PDAC) undergo autophagy, but its effects vary with tumor stage and genetic factors. We investigated the consequences of varying levels of the autophagy related 5 (Atg5) protein on pancreatic tumor formation and progression.

Methods: We generated mice that express oncogenic Kras in primary pancreatic cancer cells and have homozygous disruption of *Atg5* (*A5;Kras*) or heterozygous disruption of *Atg5* (*A5+/-;Kras*), and compared them with mice with only oncogenic *Kras* (controls). Pancreata were analyzed by histology and immunohistochemistry. Primary tumor cells were isolated and used to perform transcriptome, metabolome, intracellular calcium, extracellular cathepsin activity, and cell migration and invasion analyses. The cells were injected into wildtype littermates, and orthotopic tumor growth and metastasis were monitored. *Atg5* was knocked down in pancreatic cancer cell lines using small hairpin RNAs; cell migration and invasion were measured, and cells were injected into wildtype littermates. PDAC samples were obtained from independent cohorts of patients and protein levels were measured on immunoblot and immunohistochemistry; we tested the correlation of protein levels with metastasis and patient survival times.

Results: *A5+/-;Kras* mice, with reduced Atg5 levels, developed more tumors and metastases, than control mice, whereas *A5;Kras* mice did not develop any tumors. Cultured *A5+/-;Kras* primary tumor cells were resistant to induction and inhibition of autophagy, had altered mitochondrial morphology, compromised mitochondrial function, changes in intracellular Ca2+ oscillations, and increased activity of extracellular cathepsin L and D. The tumors that formed in *A5+/-;Kras* mice contained greater numbers of type 2 macrophages than control mice, and primary *A5+/-;Kras* tumor cells had upregulated expression of cytokines that regulate macrophage chemoattraction and differentiation into M2 macrophage. Knockdown of *Atg5* in pancreatic cancer cell lines increased their migratory and invasive capabilities, and formation of metastases following injection into mice. In human PDAC samples, lower levels of ATG5 associated with tumor metastasis and shorter survival time.

Conclusions: In mice that express oncogenic Kras in pancreatic cells, heterozygous disruption of *Atg5* and reduced protein levels promotes tumor development, whereas homozygous disruption of *Atg5* blocks tumorigenesis. Therapeutic strategies to alter autophagy in PDAC should consider the effects of ATG5 levels to avoid the expansion of resistant and highly aggressive cells.

Key words: Atg5-levels, pancreatic carcinogenesis, Ca2+, mitochondria, cathepsins

INTRODUCTION:

Pancreatic ductal adenocarcinoma (PDAC), the most common type of pancreatic cancer, frequently exhibits mutations in the *KRAS* oncogene leading to constitutive activation of the KRAS-signaling pathway. Oncogenic KRAS has been shown to promote tumorigenesis through cell-autonomous (proliferation, migration, survival) and non-cell autonomous (tumor microenvironment) effects. In addition, it has also recently been associated with pro-tumorigenic alterations in cell metabolism, protein synthesis, cell growth, and stimulation of autophagy [1].

Autophagy is a central regulator of metabolism and cell homeostasis [2, 3]. During baseline or cell stress/ nutrient starvation-triggered autophagy, cytoplasmic constituents are engulfed into double membrane autophagosomes and delivered to lysosomes for degradation and recycling. Autophagy typically orchestrates detoxification, release of nutrients, and restoration of cell homeostasis. Multiple autophagy genes (Atg) are involved in autophagosome formation. An important player is Atg5, which binds to Atg12-Atg16 and mediates conjugation of LC3 I to phosphatidylethanolamine (PE), forming LC3 II. LC3 II is attached to the autophagosomal membrane and interacts with multiple adaptor proteins (e.g., *Sqstm1*/ p62) shuttling cargo molecules to autophagosomes.

Atg5 is required for formation of LC3 II-positive autophagosomes and maintenance of autophagic flux. Inhibition of autophagy by deletion of *Atg5* in the context of oncogene activation/ tumor suppressor gene inhibition has been performed in multiple tissue types to study the role of autophagy during various stages of carcinogenesis [3]. Surprisingly, *Atg5*-deletion in the pancreas [4, 5] and lung [6] has been shown to increase tumor initiation but decrease tumor progression indicating a tumor stage-dependent action of autophagy. The underlying mechanisms of these phenotypes were proposed to be increased DNA-damage, cell stress, apoptosis, and metabolic deficiencies.

Here we describe for the first time the opposing functions that varying levels of Atg5 have during pancreatic carcinogenesis. With the help of well-established models of *in vitro* and *in vivo* pancreatic carcinogenesis we show that stages of pancreatic carcinogenesis critically depend on the levels of Atg5. Complete loss of *Atg5* in the pancreas during embryogenesis accelerates tumor initiation but blocks tumor progression, while monoallelic loss significantly increases tumor incidence and metastasis rate. Importantly, deletion of one *Atg5*-allele and reduction of Atg5 protein levels increases PDAC aggressiveness through cell-autonomous and non-cell autonomous effects, collectively enhancing tumor malignancy. ShRNA-mediated knockdown of *Atg5* further highlights that the exact association of Atg5-levels with PDAC phenotype follows a non-linear pattern. Thus, our results not only provide novel

evidence on the role of autophagy during PDAC development and progression but also highlight the importance of exercising caution when blocking autophagy in PDAC.

MATERIALS AND METHODS:

All authors had access to the study data and reviewed and approved the final manuscript.

Mice

The *Atg5*$^{flox/flox}$ [7], *Ptf1a-cre*^{ex1} [8], *LSL-Kras*^{G12D} knock-in [9] strains were interbred to generate compound mutant *Atg5*$^{flox/flox}$; *Ptf1a-cre*^{ex1}*; LSL-Kras*^{G12D} (termed *A5;Kras*), *Atg5*$^{flox/+}$*;Ptf1a-cre*^{ex1}*; LSL-Kras*^{G12D} (termed *A5+/-;Kras*), and *Ptf1a-cre*^{ex1}*; LSL-Kras*^{G12D} (termed *Kras*) control animals. *TG(CAG-EGFP/Map1lc3b)53Nmz* transgenic mice (termed *GFP-LC3*) [10] interbred with *A5+/-;Kras* mice to generate *A5;Kras* (termed *GFP-LC3;A5;Kras)*, *A5+/-;Kras* (termed *GFP-LC3;A5+/-;Kras)* or *Kras* (termed *GFP-LC3;Kras*) mice with concomitant GFP-LC3 expression were used for autophagosome detection. Littermate animals without *Ptf1a-cre*^{ex1} expression were used for orthotopic transplantation and tail vein injections. For all the experiments, mice were housed under specific pathogen-free conditions. All animal procedures were reviewed and approved by the Zentrum für Präklinische Forschung of the Technische Universität München, which follows the federal German guidelines for ethical animal treatment (Regierung von Oberbayern).

Statistical Analysis

Data are displayed as mean ± standard deviation (SD). Student t test was performed to compare the parameters for the groups by using GraphPad Prism. An appropriate and statistical significance was set at $*P<0.05$, $**P<0.01$, and $***P<0.001$. Survival rates were calculated and displayed by the Kaplan–Meier method. Survival curves were compared by log-rank test using GraphPad Prism.

RESULTS:

Monoallelic loss of *Atg5* influences metastatic load

Autophagy can be visualized in the pancreas as GFP-LC3 positive autophagosomes using *GFP-LC3* transgenic mice (Figure 1A). Under normal fed conditions, GFP-LC3 puncta are visible in acinar cells. During pancreatic carcinogenesis, autophagosomes are detectable in pre-malignant acinar-to-ductal metaplasias (ADM), pancreatic intraepithelial neoplasias (PanIN), as well as in full-blown pancreatic tumors and metastasis (liver) of *GFP-LC3;Kras* mice. In addition, cells isolated from pancreatic tumors and their metastases are positive for GFP-LC3 autophagosomes (data not shown). Interestingly, PanIN-adjacent normal acinar cells lack GFP-LC3-positive puncta, despite harboring the oncogenic $Kras^{G12D}$ mutation (white star, Figure 1A). With complete loss of *Atg5* however, only a diffuse staining is visible (Supplementary Figure 1A). Autophagy is therefore present in each stage of pancreatic tumor formation and metastasis.

To elucidate the role of autophagy during PDAC, we generated mice with homozygous (*A5;Kras*) and heterozygous (*A5+/-;Kras*) deletion of *Atg5* and compared them to autophagy proficient *Kras* mice. As previously shown [4], complete loss of *Atg5* accelerates tumor initiation by significantly enhancing ADM (Supplementary Figure 1A, B, D) and increasing pancreas/body weight index at 4-weeks of age (Supplementary Figure 1C); however, *A5;Kras* mice only progress to PanIN-1 at 9-weeks of age (Supplementary Figure 1B, E) and do not develop more malignant stages of the disease (Supplementary Figure 1E). In fact *A5;Kras* mice have reduced survival (Supplementary Figure 1F) associated with severe pancreatic degeneration as shown by a significantly lower relative pancreatic weight starting at 18 weeks of age (Supplementary Figure 1C). *A5+/-;Kras* mice did not differ in ADM/ PanIN formation, pancreas/ body weight ratio or survival compared to *Kras* mice (Supplementary Figure 1B, C, D, E, F). Of note, pancreatitis responses and pancreatitis-associated progression of ADM/ PanIN-lesions were not different in all mouse lines (data not shown). Surprisingly however, monoallelic loss of *Atg5* significantly increased tumor and metastasis incidence, determined at the time of sacrifice, compared to autophagy proficient and autophagy deficient genotypes (Figure 1B, C, D, Supplementary Table 1). As shown in Figure 1B, primary tumors formed in *A5+/-;Kras* mice were characterized by a high degree of histologic malignancy; at the same time multiple metastatic foci were visible in target tissues, a phenotype normally not present in autophagy proficient *Kras* mice.

Therefore, monoallelic and not biallelic loss of *Atg5* critically influences pancreatic tumor initiation, progression, and metastasis.

Autophagy is constitutively active after monoallelic loss of *Atg5* influencing survival *in vitro*.

To mechanistically examine the effect of monoallelic *Atg5*-loss on PDAC, we firstly evaluated how monoallelic *Atg5*-loss influences autophagy. As autophagic flux can be readily analyzed *in vitro*, we isolated primary pancreatic cancer cells from *Kras* and *A5+/-;Kras* mice. During our study, one *A5;Kras* mouse from all *A5;Kras* mice analyzed (n=24, Supplementary Figure 1B) stochastically developed PDAC. This cell line could not be propagated *in vitro* (data not shown) and was used only as a control for Atg5 protein expression analysis. Figure 2A shows Atg5 protein expression, detected as a complex with Atg12, in the cell line lysates. Importantly, reduction in Atg5 protein was evident in *A5+/-;Kras* cells and in *A5+/-;Kras* mice (Figure 2A). Cell morphology and cell proliferation capacities were not influenced (Figure 2B). Interestingly however, while autophagic flux was not different between *Kras* and *A5+/-;Kras in vitro* and *in vivo* (Figure 2A, 2D), autophagy regulation after treatment with autophagy activators or inhibitors was influenced. Specifically, starvation with HBSS functionally affected *Kras* cells by significantly reducing colony numbers compared to 10% FCS-containing medium (Figure 2C). Colony formation in *A5+/-;Kras* cells was not compromised. FCS-starvation led to an accumulation of LC3-II, which was even more evident in *Kras* versus *A5+/-;Kras* cells after co-treatment with chloroquine (Figure 2D). Autophagic flux inhibition was validated by elevated p62 protein levels in both cell types, specifically however in *Kras* cells after co-treatment with chloroquine (Figure 2D). AMPKalpha phosphorylation was slightly increased in *A5+/-;Kras* cells, suggesting that AMPKalpha remains responsive to starvation in *A5+/-;Kras* cells (Figure 2D). In addition, increasing chloroquine treatment significantly affected colony formation only in *Kras* cells (Figure 2D). Finally, Cyto-ID-mediated quantification of autophagosomes after FCS-starvation showed an elevation in autophagosome numbers only in *Kras* cells (Figure 2E). Of note, treatment of *Kras* and *A5+/-;Kras* cells with various metabolic regulators (10% FCS, 6-AA, rotenone, galactose/ glutamine, high glucose) did not differentially affect the colony forming capacities of *Kras* and *A5+/-Kras* cells (Supplementary Figure 2A-E).

Thus, monoallelic loss of *Atg5* and reduced Atg5 protein levels lead to specific changes in autophagic regulation, making *A5+/-;Kras* cell lines more resistant to standard autophagy stimulation and inhibition.

Monoallelic loss of *Atg5* increases metastatic properties of cancer cells *in vitro* and *in vivo*.

As *A5+/-;Kras* mice had a higher tumor and metastasis incidence we aimed to analyze in more detail the effect of *Atg5*-monoallelic loss on tumor and metastasis formation. *In vitro* experiments with *Kras* and *A5+/-;Kras* cells revealed significantly increased anoikis

resistance (Figure 3A), migration, invasion, and cell spreading in *A5+/-;Kras* cells (Figure 3B), all of which influence metastatic capacities of tumor cells. Filopodia formation, an indicator of cell spreading, was also clearly detectable in *A5+/-;Kras* cells while *Kras* cells displayed only small protrusions (Figure 3B). Tumor formation after orthotopic transplantation was similar in *Kras* and *A5+/-;Kras* cell lines, with both cell lines forming CK19-positive ductal tumors, morphologically resembling primary tumors (Supplementary Figure 3A). However, metastasis incidence (%) after orthotopic transplantation was significantly increased in *A5+/-;Kras* cells, with cells metastasizing to sites including lymph nodes, liver, lung, and spleen (Supplementary Figure 3B). In a second model for target tissue colonization, significantly more lung tumors (%) were formed after tail vein injection of wildtype mice with *A5+/-;Kra*s versus *Kras* cells (Figure 3C). Body weight of mice, as an indicator of cachexia, was also reduced after injection with *A5+/-;Kras* cells (Supplementary Figure 3C). In addition to lung tumor formation, some mice exhibited liver and spleen metastasis, implying higher aggressiveness of pancreatic tumor cells after monoallelic loss of *Atg5* (Supplementary Figure 3D). Proliferation of lung tumors (Figure 3C), as well as *in vitro* proliferation of *A5+/-;Kras* cell lines after re-isolation from lung tumors (Supplementary Figure 3D), was also increased.

To elucidate the association between *Atg5* expression levels and PDAC-malignancy, we knocked down *Atg5* in *Kras* cell lines using shRNAs with various knockdown efficiencies (54%, 58%, 81%, 86%, and 94%). All shRNAs were able to affect *Atg5* expression levels with the aforementioned efficiency at the mRNA (data not shown) and protein level (Figure 3D). As 58% *Atg5* knock down resembles the situation after monoallelic loss of *Atg5* we continued with these cells for further analyses. We also utilized 94% *Atg5* knock down cells, to determine, whether the levels at which *Atg5* influences PDAC phenotype coincide with a certain percentage. Importantly, knock down of *Atg5* by 58% or 94% significantly enhanced migration and invasion *in vitro* (Figure 3E) as well as lung metastasis *in vivo* (Figure 3F). Colony formation after cultivation in 10% FCS-containing medium was not affected (Supplementary Figure 3E).

Therefore, our data suggest that monoallelic loss of *Atg5* during embryonic development as well as shRNA-mediated *Atg5*-dosage reduction increase metastatic capacities and aggressiveness of cells *in vitro* and *in vivo*.

Monoallelic loss of *Atg5* is sufficient to induce transcriptional and metabolic changes.

Autophagy is known to regulate transcription [11]. In addition, the autophagy-lysosomal pathway is controlled on a transcriptional level in PDAC [12]. To investigate how monoallelic loss of *Atg5* increases tumor cell metastasis and aggressiveness, we therefore performed transcriptomic analyses in *Kras* and *A5+/-;Kras* pancreatic tumor cells. Surprisingly, loss of

one allele of *Atg5* was sufficient to change transcriptomic pathway regulation on a large scale. Gene enrichment analysis revealed that loss of one allele of *Atg5* led to a reduction in the number of upregulated pathways by half (Figure 4A). Functional classification of the most significantly regulated genes (Supplementary Figure 4C) identified multiple cellular functions affected by monoallelic loss of *Atg5* (Figure 4B). Most importantly, an increase was seen in metabolism, immunity, development, and vesicular trafficking/homeostasis associated cellular functions; a decrease was seen in adhesion and cell cycle associated cellular functions (Figure 4B). Classification of KEGG-pathways confirmed the increase in inflammation and the decrease in proliferation/ synthesis-associated pathways in *A5+/-;Kras* cells (Figure 4C, Supplementary Figure 4B). Interestingly, the gene set associated with lysosomal function was enriched in *A5+/-;Kras* cells (Figure 4C, Supplementary Figure 4B) further supporting a deregulation in vesicular homeostasis. Of note, gene enrichment analysis using the Transcription Factor Binding Motif database further supported the enrichment of development and inflammation-associated gene sets and the downregulation of proliferation-associated gene sets in *A5+/-;Kras* cells (Supplementary Figure 4A, 4B).

Because autophagy influences metabolic pathways, we performed non-targeted metabolic profiling in *Kras* and *A5+/-;Kras* cell lines and their supernatants (Figure 4D). Importantly, *A5+/-;Kras* cells contained increased amounts of nucleotides and spermidine, representing deregulated proliferation, elevated amounts of oxidative and cell stress-associated metabolites (e.g., *S*-nitrosoglutathione, hypotaurine, S-lactoylglutathione, involved in oxidative stress, and ADP-ribose connected with cell stress), increased 3/2-phosphoglycerate implicated in glucose metabolism, and changes in the amounts of fatty acids engaged in energy metabolism (e.g., myristoylcarnitine, valerylcarnitine). Supernatants of *A5+/-;Kras* cells showed changes in lysolipids (e.g., 1-Stearoyl-GPE) and other lipids (e.g., polyunsaturated fatty acids), indicative of changes in membrane composition/ signaling; arginine, suggesting an influence on the immune microenvironment (macrophages); and 6-phosphogluconate, a metabolite associated with the pentose phosphate pathway.

Thus, monoallelic loss of *Atg5* is sufficient to induce global transcriptomic and metabolomic changes, mostly in pathways associated with metabolism, inflammation, and vesicle homeostasis.

Monoallelic loss of *Atg5* reduces mitochondrial functionality.

To gain further insight into the effect of monoallelic *Atg5*-loss on metabolism, we performed a series of experiments related to mitochondrial functionality and cell stress. Electron microscopy revealed changes in mitochondrial morphology. In particular, there was an increase in mitochondrial fission and differences in cristae stacking between *Kras* and *A5+/-;Kras* cells (Figure 5A). Protein expression analyses illustrated slight increases in oxidative

phosphorylation associated mitochondrial proteins (COX II/ IV, ATP Core 2), in mitochondrial stress-associated SOD2, and in endoplasmic reticulum (ER)-stress associated BiP (Supplementary Figure 5A). ER-stress was also indicated by an elevation in the spliced form of *Xbp1* (Supplementary Figure 5A). Expression of p53 however was not influenced (data not shown). Mitochondrial function was further assessed by detailed comparison of oxidative and glycolytic capacities in *Kras* and *A5+/-;Kras* cell lines (Figure 5B-D). We detected a decrease in oxidative capacity, as evidenced by cellular respiration rate, mitochondrial respiration rate, and maximum substrate oxidation rate, at the expense of mitochondrial ATP production (Figure 5B). In addition *A5+/-;Kras* cells showed a reduction in glycolysis, as evidenced by decreased cellular acidification rates, maximum glycolytic capacity, and baseline acidification rate (Figure 5C). Mitochondrial coupling efficiency did not show any significant change (Supplementary Figure 5B). Figure 5D verifies these results in an oxygen consumption rate versus extracellular acidification plot (OCR/ ECAR), showing a weakening in metabolic activity in *A5+/-;Kras* cells. This is indicated by the movement of the *A5+/-;Kras* cell line measurements towards both, lower OCR and lower ECAR, demonstrating decreased ATP turnover. Interestingly, cellular fractionation experiments revealed a displacement in the mitochondrial fraction as detected by GLDH-activity. In particular, mitochondria were shifted towards the autophagosomal fraction, indicating decreased integrity of mitochondria (Figure 5E). Finally, mRNA expression levels of *Nrf1* and mitochondrial *Sod2* were increased corroborating the elevated mitochondrial stress (Figure 5F); *Nrf2* and cytosolic *Sod1* were not changed (Supplementary Figure 5C).

Concluding, monoallelic loss of *Atg5* affects cellular homeostasis by altering mitochondrial morphology and compromising mitochondrial function.

***Atg5* level influences intracellular Ca2+ flux and extracellular cathepsin activity.**

Mitochondria play an important role in buffering intracellular Ca2+ levels and are thus closely linked to Ca2+ fluctuations. In addition, Ca2+ responses influence mitochondrial function/ morphology, gene transcription [13-15], vesicle trafficking, cellular migration, and lamellipodia formation at the front of migrating cells [16]. Thus, we examined in more detail cellular Ca2+ responses as a putative mechanism connecting our observations. In support, Ca2+ responses of *Kras* and *A5+/-;Kras* cells after treatment with 0.01 or 0.05% FBS were significantly different (Figure 6A). Cytosolic Ca2+ responses in *A5+/-;Kras* cells were characterized by higher amplitudes and only one peak of Ca2+ elevation. Moreover the number of FBS-responding cells was slightly elevated in *A5+/-;Kras* versus *Kras* cells (Supplementary Figure 6A). S100a4, a Ca2+ - binding protein associated with increased metastatic capacities, was found highly expressed in *A5+/-;Kras* tumors compared to only a

low-level expression in *Kras* tumors. The higher PanIN orders and established PDAC-structures were particularly positive for S100a4 expression (Figure 6B).

Lysosomal trafficking and exocytosis of lysosomal cathepsins is also regulated by intracellular Ca2+ fluctuations [17]. Quantification of lysosomal cathepsin activities in cell culture supernatants revealed a significantly higher activity of cathepsin L and cathepsin D (Figure 6C), whereas cathepsin B was not affected (Supplementary Figure 6B). Protein levels of the respective pro-cathepsins also showed a tendency towards increased amounts in *A5+/-;Kras* cells (Supplementary Figure 6B). In addition, copy number of genes associated with lysosomes indicated a difference in regulation between normal pancreas and pancreatic cancer samples (Supplementary Figure 6D).

Furthermore, we functionally evaluated the importance of extracellular cathepsin activity in cell spreading and invasion. For this we treated *Kras* and *A5+/-;Kras* cells with the cathepsin inhibitor E64d, and quantified the number of filopodia per sphere (Figure 6D) and the number of matrigel invaded cells (Figure 6E). While the number of colonies formed by *Kras* and *A5+/-;Kras* cells did not change after E64d-treatment (Supplementary Figure 6C), cell spreading and invasive capacities were significantly reduced in *A5+/-;Kras* cells (Figure 7D, 7E). Of note, E64d did not affect filopodia formation and invasive capacities of *Kras* cells (data not shown).

In summary, levels of *Atg5* significantly influence cellular Ca2+ responses and lysosomal enzyme activities, which are required for increased cell spreading and invasion.

Monoallelic loss of *Atg5* induces pro-tumorigenic inflammation

Changes in inflammation have been shown to promote tumorigenesis and cancer cell invasion/ metastasis. Our transcriptomic results identified alterations in inflammatory pathways. Moreover, extracellular arginine levels, known to influence pro-tumorigenic- versus pro-inflammatory M1-macrophages, were increased in *A5+/-;Kras* versus *Kras* cells. Thus, we aimed to elucidate the effect of *Atg5*-monoallelic loss on macrophage-mediated inflammation. Firstly, we examined the cytokine/ chemokine profile of *Kras* and *A5+/-;Kras* cells in cell culture supernatants (Supplementary Figure 7A). Quantification of dot plot-pixel intensity revealed upregulation of cytokines involved in macrophage chemoattraction (CXCL1, CXCL12), M2-differentiation (M-CSF, CXCL12, IL10, CXCL2, IL1ra, CXCL10), and tumor progression/ metastasis (TNFa) in *A5+/-;Kras* versus *Kras* cells, while cytokines important for M1-polarization (GM-CSF), M1-chemoattraction (sICAM-1), and granulocyte attraction (G-CSF) were downregulated. To analyze in more detail the effect of *Kras* and *A5+/-;Kras* cells on the inflammatory microenvironment, we treated undifferentiated macrophages with the cell culture supernatants of *Kras* and *A5+/-;Kras* cells and characterized the changes in macrophage morphology, as described previously [18].

Supernatants from *Kras* cells induced macrophage differentiation into the M1-subtype; supernatants form *A5+/-;Kras* cells on the other hand shifted differentiation towards the M2-subtype, (increased cell elongation, Supplementary Figure 7B), confirmed by elevated levels of Arginase 1 expression (Supplementary Figure 7B). Moreover, we assessed the *in vivo* ability of *Kras* and *A5+/-;Kras* cells to attract macrophages by quantifying F4/80 and CD206 in the original pancreatic tumor tissues of these mice (Supplementary Figure 7C). Importantly, F4/80- and CD206-macrophage numbers were clearly elevated in *A5+/-;Kras* tumors, indicating more CD206 and thus M2-macrophages after monoallelic loss of *Atg5*. More F4/80 and Arginase 1-positive M2-macrophages were also attracted into the lungs of mice after tail vein injection of *A5+/-;Kras* compared to *Kras* cells (Supplementary Figure 7D), further supporting the *in vitro* and *in vivo* results (Supplementary Figure 7B, C).

To determine if macrophages critically influence the metastatic capabilities of *A5+/-;Kras* cells, we depleted macrophages in wildtype mice using liposomal-clodronate. Subsequently, we performed tail vein injection of *A5+/-;Kras* cells and analyzed lung tissue metastasis. Clodronate treatment was able to deplete most on the macrophages, as shown by F4/80 immunohistochemistry (Supplementary Figure 7E, right). Interestingly, macrophage depletion significantly reduced metastasis of *A5+/-;Kras* cells compared to control liposome-treated mice, highlighting the importance of infiltrating macrophages in potentiating metastasis.

Consequently, monoallelic loss of *Atg5* induces changes in cytokine/ chemokine secretion from tumor cells resulting in accumulation of M2-macrophages ultimately shaping the inflammatory microenvironment to critically favor tumor aggressiveness and promote tumor metastasis.

Levels of ATG5 are correlated to human pancreatic cancer aggressiveness

To establish a connection between the mouse model results and human pancreatic cancer we analyzed ATG5 protein levels in three independent patient cohorts (Supplementary Tables 2, 3, 4). ATG5-ATG12 protein expression in lysates from pancreatic tumor patients (Cohort 1) was different between the samples (Figure 7A, top). Grouping the patients into ATG5 high versus ATG5 low-moderate expression indicated a trend towards reduced survival in the low-moderate ATG5-expression group (Figure 7A, bottom). Due to the variations in tumor cellularity and the limitations of western blotting, we performed ATG5 immunohistochemistry (Cohort 2 and Cohort 3). As expected and already described (ProteinAtlas), ATG5 is expressed not only in the pancreatic epithelial tumor structures but also in other cell types (e.g., endothelial and islet cells) in the tissue (Figure 7B). After establishing an ATG5-expression score (Score 1, Score 2, Score 3), we divided the patients into low-moderate (Score 1, Score 2) and high (Score 3) ATG5 expression (Figure 7B). Applying this analysis on a small distant metastatic patient cohort (Cohort 2) showed a higher

metastasis incidence in the low-moderate ATG5 expressing patients (Figure 7C). Furthermore, we could significantly correlate reduced survival with lower ATG5 expression in a larger cohort of patients undergoing pancreatic cancer resection (Cohort 3, Figure 7D). Because lymph node and resection status was not different between the groups, ruling out important confounding factors (Figure 7D), these analyses very likely reflect the re-occurrence of metastases and thus aggressiveness of the tumors. Of note, metastatic relapse in resected patients determines survival. Finally, TCGA-databank analysis identified a reduction in *ATG5* copy numbers between pancreatic cancer samples and normal human pancreas (Figure 7D).

Thus, lower levels of ATG5 are associated with increased pancreatic cancer metastasis and patient survival.

DISCUSSION:

Autophagy has been shown to play a dual role in tumorigenesis of different tissue types [3, 19]. Particularly, autophagy seems to accelerate tumor initiation while blocking progression of pre-neoplastic lesions, as exemplified in PDAC [2]. Studies have mainly made use of models with complete loss of autophagic function, a fact that is rarely seen in human patients. Therefore, we aimed to analyze the effect of varying levels of Atg5 on PDAC development. Surprisingly, complete loss of *Atg5* blocks tumorigenesis, while monoallelic loss of *Atg5* promotes tumorigenesis and metastasis. We suggest cell intrinsic changes in mitochondrial homeostasis, Ca2+ responses, autophagy regulation, and lysosomal cathepsin activation as well as changes in the inflammatory tumor microenvironment to be crucial for aggressiveness of pancreatic cancer. Importantly, shRNA-mediated *Atg5*-dosage regulation also increased metastatic capabilities of pancreatic cancer cells, indicating that a simple decrease in Atg5 levels is sufficient to influence PDAC metastasis. The clinical significance of this observation is supported by the analysis of three independent human pancreatic cancer cohorts verifying an association between ATG5 levels, PDAC metastasis and patient survival.

Autophagy is closely connected with PDAC and multiple pathways influence this interaction, e.g., ROS-levels, ER-stress, hypoxia, mitochondrial metabolism, and the surrounding tumor microenvironment [2]. Past studies have shown that the interplay between oncogenic *Kras* and autophagy during PDAC progression is also regulated by other genetic alterations, but contradictory results did not enable clear conclusions [4, 5]. Our initial analysis of sequential pancreatic cancer stages implicated targeted induction of autophagy during PDAC development, confirming past results on gradual elevation of baseline autophagy during carcinogenesis [2]. The importance of autophagy in pancreatic cancer progression was further verified by homozygous deletion of *Atg5*, confirming past results [4]. Along the same line, whole-body inhibition of autophagy was recently shown to control tumor cell growth via intrinsic and extrinsic mechanisms in mice [20]. Unlike complete loss of *Atg5*, however, monoallelic loss resulted in a higher tumor incidence and metastasis occurrence. *Atg5*-dosage regulation through shRNA-mediated knock down also enhanced metastatic capabilities of pancreatic cancer cells, indicating that although there is a clear phenotypic difference between complete presence, partial presence, and complete absence of *Atg5*, the phenotypic effect follows *Atg5*-dosage in a non-linear fashion. So far, only one published study has uncovered a connection between monoallelic deletion of *Atg5* and increased metastasis in melanoma supporting our results [21]. Nonetheless, the underlying mechanisms for the phenotype in melanoma are still obscure.

Atg5, as apart of the Atg-conjugation system, is required for autophagic flow. Atg-mediated closure of autophagosomes is necessary for subsequent lysosomal degradation and recycling of membrane components [22]. Upon complete loss of *Atg5* in the pancreas, autophagosomes accumulate in acinar cells and degradation is blocked [11]. However, the impact of *Atg5* monoallelic loss on autophagic flux remains unclear. In *A5+/-;Kras* cells and tumors we detected decreased Atg5 protein expression. Interestingly, reduced protein amounts did not result in an apparent negative consequence on autophagy as *A5+/-;Kras* cells were more resistant to autophagy inhibitors or activators and functionally not affected. Multiple non-canonical autophagy and intracellular degradation pathways exist that might compensate for monoallelic loss of *Atg5* (e.g., microautophagy, chaperone-mediated autophagy, non-canonical autophagy independent of various core autophagy proteins, selective autophagy, macropinocytosis) [23, 24]. In order to fully illuminate the effect of monoallelic *Atg5*-loss on autophagy-associated pathways and to extent pancreatic tumor progression, more future studies are required. Therefore, our present results show that monoallelic loss of *Atg5* enhanced autophagy levels in a cell-intrinsic manner, indicating active adaptation of pancreatic cancer cells.

Loss of one allele of *Atg5* significantly changed not only autophagy regulation, but also tumor cell behavior by enhancing migration and invasion. Importantly, *Atg5*-heterozygous cell lines could form tumors in hosts and had a higher capacity to metastasize to distant organs. Metastasis is a multistep process involving a plethora of cellular adaptations [25]. Mitochondria [26], Ca2+ oscillations [27], extracellular matrix degradation [28], and the tumor microenvironment [29] have been shown to determine tumor malignancy and dissemination. Interestingly, we could detect changes in mitochondrial homeostasis with loss of one allele of *Atg5*. Specifically, mitochondrial function was reduced, while distinct mitochondrial stress markers were upregulated. Mitochondrial turnover was also affected as more fission events could be documented along with an increase of mitochondrial mass in the autophagosomal fraction, indicating uptake of damaged mitochondria. Past studies have shown that increased mitochondrial fission and fragmentation supports tumor cell growth, invasion, and migration [26]. Moreover, mitochondrial metabolism is necessary to support cancer cell dissemination, while a certain degree of cell stress is required for tumor cells to alter their mitochondrial programming and promote cellular adaptation [30-32]. Mitochondria are also known to influence Ca2+ signaling amplitude and propagation rate by sequestering Ca2+. Especially in polarized pancreatic acinar cells, where a considerable portion of mitochondria are localized in the apical part of the cell, Ca2+ transients are effectively confined and spatially regulated [13]. Interestingly, intracellular Ca2+ fluctuations are involved in tumor cell dissemination influencing migration and vesicle trafficking [16, 33]. Along these lines, monoallelic loss of *Atg5* influenced FBS-mediated migration/ invasion, FBS-induced Ca2+ responses as well as

expression of Ca2+ handling proteins. In support, *Atg5* expression was recently linked to heightened tumor cell metastasis via disrupting the V1Vo ATPase, which is closely connected to cytosolic Ca2+, indicating a pathway through which a autophagy-related gene can promote metastasis in an autophagy-independent manner [34]. Therefore, monoallelic loss of *Atg5* might establish an intermediate stress level in tumor cells disturbing mitochondrial homeostasis and to a certain extent Ca2+ signaling, heightening their aggressive and metastatic potential.

Tumor cell invasion further requires digestion of extracellular matrix, which can be achieved through lysosomal cathepsins [28]. Lysosomes are highly responsive to changes in intracellular Ca2+ fluxes via expression of Ca2+ channels. One such channel is TRPM2, which is specifically activated by intracellular adenosine diphosphoribose (ADPR) [35]. ADPR was elevated in *A5+/-;Kras* compared to *Kras* cells. Lysosomal Ca2+ signaling is connected to the autophagy process [36]. In addition, lysosomes contain cysteine cathepsins, which are not only responsible for degradation, but also play a role in autophagy, metabolism, and lysosome-mediated cell death. Cathepsins regulate the numbers of autophagosomes and lysosomes [37]. Our data pointed to a heightened level of autophagy in *A5+/-;Kras* cells. *A5+/-;Kras* cells exhibited enhanced extracellular cathepsin activation. Importantly, cathepsin activation in the extracellular medium was required and sufficient to enable invasion of cancer cells. Monoallelic loss of *Atg5* may in this scenario initiate multiple cellular changes starting with mitochondrial and Ca2+ homeostasis. Affected Ca2+ homeostasis may influence lysosomal numbers and fusions with autophagosomes, aggravated even further by the direct effects of *Atg5* on autophagy levels. In addition, it was shown that the interaction of Atg5-Atg12 with the tethering factor TECPR1 (Tectonin Beta-Propeller Repeat Containing 1) is crucially involved in the initiation of autophagosomal/ lysosomal fusion to promote autophagic flux [38]. In this context monoallelic loss of *Atg5* could be tightly interrelated to impaired lysosomal biogenesis and fusion. A hindered autolysosomal maturation process may thus lead to an accidental activation of pro-cathepsins and subsequently their release into the extracellular medium ultimately promoting migration, invasion, and metastasis.

Lysosomal homeostasis can also affect the immune system and cytokine secretion, especially in conjunction with cathepsin activities [39]. The inflammatory tumor microenvironment is crucial in facilitating spontaneous PDAC development and amplifying the metastatic process. Anti-inflammatory M2-macrophages, regulatory lymphocytes, and neutrophils have been shown to potentiate PDAC [29, 40]. Interestingly, we saw a shift in the cytokine profile of *A5+/-;Kras* cells towards cytokines involved in promoting pro-tumorigenic M2-macrophages. In support of all these data we also detected more M2-macrophages in the original *A5+/-;Kras* primary pancreatic tumors as well as in the lung tumors formed after tail vein injection of *A5+/-;Kras* cell lines. Importantly, depleting macrophages significantly

reduced *A5+/-;Kras* cell metastasis *in vivo*, highlighting the importance of macrophages in potentiating metastasis. Consequently, monoallelic loss of *Atg5* leads to cell-intrinsic changes, which ultimately affect the tumor microenvironment favoring metastatic spread.

So far, only the autophagy protein Beclin-1 has been found monoallelically deleted in a variety of cancer types, such as breast, ovarian, and prostate cancer. In support of these findings *Beclin-1* heterozygous mice display frequent spontaneous malignancies [41]. Our study expands the spectrum of monoallelically affected autophagy genes to *Atg5*, correlating ATG5 protein expression with metastasis and survival in three independent human pancreatic cancer cohorts. Clinical trials on pancreatic cancer patients are currently evaluating autophagy inhibitors such as chloroquine in adjuvant therapies combined with gemcitabine (NCT01777477 [42]). However, autophagy inhibitors are not only less specific, but very likely to only partially impede autophagic flux [43]. As we have shown that monoallelic loss of *Atg5* leads to chloroquine resistance and higher metastatic spread, administration of chloroquine may thus generate resistant cancer cell clones with heightened aggressiveness. Therefore, our data alert towards increased awareness when applying autophagy blockers in clinical trials for pancreatic cancer patients.

REFERENCES:

1. Zeitouni D, Pylayeva-Gupta Y, Der CJ, et al. KRAS Mutant Pancreatic Cancer: No Lone Path to an Effective Treatment. Cancers (Basel) 2016;8.
2. New M, Van Acker T, Long JS, et al. Molecular Pathways Controlling Autophagy in Pancreatic Cancer. Front Oncol 2017;7:28.
3. Santana-Codina N, Mancias JD, Kimmelman AC. The Role of Autophagy in Cancer. Annual Review of Cancer Biology 2017;1:19-39.
4. Rosenfeldt MT, O'Prey J, Morton JP, et al. p53 status determines the role of autophagy in pancreatic tumour development. Nature 2013;504:296-300.
5. **Yang A, Rajeshkumar NV**, Wang X, et al. Autophagy is critical for pancreatic tumor growth and progression in tumors with p53 alterations. Cancer Discov 2014;4:905-13.
6. Rao S, Tortola L, Perlot T, et al. A dual role for autophagy in a murine model of lung cancer. Nat Commun 2014;5:3056.
7. Hara T, Nakamura K, Matsui M, et al. Suppression of basal autophagy in neural cells causes neurodegenerative disease in mice. Nature 2006;441:885-9.
8. **Nakhai H, Sel S**, Favor J, et al. Ptf1a is essential for the differentiation of GABAergic and glycinergic amacrine cells and horizontal cells in the mouse retina. Development 2007;134:1151-60.
9. Jackson EL, Willis N, Mercer K, et al. Analysis of lung tumor initiation and progression using conditional expression of oncogenic K-ras. Genes Dev 2001;15:3243-8.
10. Mizushima N, Yamamoto A, Matsui M, et al. In vivo analysis of autophagy in response to nutrient starvation using transgenic mice expressing a fluorescent autophagosome marker. Mol Biol Cell 2004;15:1101-11.
11. Diakopoulos KN, Lesina M, Wormann S, et al. Impaired autophagy induces chronic atrophic pancreatitis in mice via sex- and nutrition-dependent processes. Gastroenterology 2015;148:626-638 e17.
12. Perera RM, **Stoykova S, Nicolay BN**, et al. Transcriptional control of autophagy-lysosome function drives pancreatic cancer metabolism. Nature 2015;524:361-5.
13. Gunter TE, Yule DI, Gunter KK, et al. Calcium and mitochondria. FEBS Lett 2004;567:96-102.
14. Gomes LC, Scorrano L. Mitochondrial morphology in mitophagy and macroautophagy. Biochim Biophys Acta 2013;1833:205-12.
15. Boland ML, Chourasia AH, Macleod KF. Mitochondrial dysfunction in cancer. Front Oncol 2013;3:292.
16. Tsai FC, Meyer T. Ca2+ pulses control local cycles of lamellipodia retraction and adhesion along the front of migrating cells. Curr Biol 2012;22:837-42.

17. Settembre C, Fraldi A, Medina DL, et al. Signals from the lysosome: a control centre for cellular clearance and energy metabolism. Nat Rev Mol Cell Biol 2013;14:283-96.
18. **McWhorter FY, Wang T,** Nguyen P, et al. Modulation of macrophage phenotype by cell shape. Proc Natl Acad Sci U S A 2013;110:17253-8.
19. Guo JY, White E. Autophagy, Metabolism, and Cancer. Cold Spring Harb Symp Quant Biol 2016;81:73-78.
20. Yang A, Herter-Sprie G, Zhang H, et al., **Kwok-Kin Wong and Alec C. Kimmelman.** Autophagy Sustains Pancreatic Cancer Growth through Both Cell-Autonomous and Nonautonomous Mechanisms. Cancer Discov 2018;8:276-287.
21. Garcia-Fernandez M, Karras P, Checinska A, et al. Metastatic risk and resistance to BRAF inhibitors in melanoma defined by selective allelic loss of ATG5. Autophagy 2016;12:1776-1790.
22. Koyama-Honda I, Tsuboyama K, Mizushima N. ATG conjugation-dependent degradation of the inner autophagosomal membrane is a key step for autophagosome maturation. Autophagy 2017;13:1252-1253.
23. Dupont N, Nascimbeni AC, Morel E, et al. Molecular Mechanisms of Noncanonical Autophagy. Int Rev Cell Mol Biol 2017;328:1-23.
24. Recouvreux MV, Commisso C. Macropinocytosis: A Metabolic Adaptation to Nutrient Stress in Cancer. Front Endocrinol (Lausanne) 2017;8:261.
25. Pachmayr E, Treese C, Stein U. Underlying Mechanisms for Distant Metastasis - Molecular Biology. Visc Med 2017;33:11-20.
26. Chen H, Chan DC. Mitochondrial Dynamics in Regulating the Unique Phenotypes of Cancer and Stem Cells. Cell Metab 2017;26:39-48.
27. White C. The Regulation of Tumor Cell Invasion and Metastasis by Endoplasmic Reticulum-to-Mitochondrial Ca2+ Transfer. Front Oncol 2017;7:171.
28. Fonovic M, Turk B. Cysteine cathepsins and extracellular matrix degradation. Biochim Biophys Acta 2014;1840:2560-70.
29. Nielsen MF, Mortensen MB, Detlefsen S. Key players in pancreatic cancer-stroma interaction: Cancer-associated fibroblasts, endothelial and inflammatory cells. World J Gastroenterol 2016;22:2678-700.
30. Altieri DC. Mitochondria on the move: emerging paradigms of organelle trafficking in tumour plasticity and metastasis. Br J Cancer 2017;117:301-305.
31. Amoedo ND, Rodrigues MF, Rumjanek FD. Mitochondria: are mitochondria accessory to metastasis? Int J Biochem Cell Biol 2014;51:53-7.
32. Porporato PE, Payen VL, Perez-Escuredo J, et al. A mitochondrial switch promotes tumor metastasis. Cell Rep 2014;8:754-66.

33. Okeke E, Parker T, Dingsdale H, et al. Epithelial-mesenchymal transition, IP3 receptors and ER-PM junctions: translocation of Ca2+ signalling complexes and regulation of migration. Biochem J 2016;473:757-67.
34. Guo H, Chitiprolu M, Roncevic L, et al. Atg5 Disassociates the V1V0-ATPase to Promote Exosome Production and Tumor Metastasis Independent of Canonical Macroautophagy. Dev Cell 2017;43:716-730 e7.
35. Lange I, Yamamoto S, Partida-Sanchez S, et al. TRPM2 functions as a lysosomal Ca2+-release channel in beta cells. Sci Signal 2009;2:ra23.
36. Di Paola S, Scotto-Rosato A, Medina DL. TRPML1: The Ca(2+)retaker of the lysosome. Cell Calcium 2017.
37. Man SM, Kanneganti TD. Regulation of lysosomal dynamics and autophagy by CTSB/cathepsin B. Autophagy 2016;12:2504-2505.
38. Chen D, Fan W, Lu Y, et al. A mammalian autophagosome maturation mechanism mediated by TECPR1 and the Atg12-Atg5 conjugate. Mol Cell 2012;45:629-41.
39. Nabar NR, Kehrl JH. The Transcription Factor EB Links Cellular Stress to the Immune Response. Yale J Biol Med 2017;90:301-315.
40. Wormann SM, Diakopoulos KN, Lesina M, et al. The immune network in pancreatic cancer development and progression. Oncogene 2014;33:2956-67.
41. Qu X, Yu J, Bhagat G, et al. Promotion of tumorigenesis by heterozygous disruption of the beclin 1 autophagy gene. J Clin Invest 2003;112:1809-20.
42. **Wolpin BM, Rubinson DA,** Wang X, et al. Phase II and pharmacodynamic study of autophagy inhibition using hydroxychloroquine in patients with metastatic pancreatic adenocarcinoma. Oncologist 2014;19:637-8.
43. Mizushima N, Yoshimori T, Levine B. Methods in mammalian autophagy research. Cell 2010;140:313-26.

Author names in bold designate shared co-first authorship

Figure 1: Monoallelic loss of *Atg5* influences metastatic load.

(A) Autophagy in the pancreas of *GFP-LC3* transgenic mice under normal conditions and during PDAC progression in *GFP-LC3*;*Kras* mice. Tumor and liver metastasis are shown; white square/ white asterisk indicate ADM/ PanIN-adjacent acinar cells (DA=DAPI). (B) Representative pictures of pancreatic, liver, and lung tumors from *Kras* and *A5+/-;Kras* mice; black arrowheads/ asterisk point to metastatic focus in liver/ lung respectively. (C) Tumor incidence (%) in *Kras* (n=54), *A5+/-;Kras* (n=12), and *A5;Kras* (n=24) mice. (D) Metastasis incidence (%) in *Kras* (n=31) and *A5+/-;Kras* (n=10) mice. Scale bars equal 50μm.

Figure 2: Monoallelic loss of *Atg5* affects cellular responses to autophagy activators and inhibitors.

(A) Immunohistochemistry and scoring (score 1 (faint) - score 3 (strong)) of Atg5, LC3, and p62 in *Kras* and *A5+/-;Kras* mouse tumors; asterisks highlight tumor structures and arrowheads tumor microenvironment; Atg5-detection in primary pancreatic tumor cells isolated from *Kras*, *A5+/-;Kras*, and *A5;Kras* mice. (B) Morphology of *A5+/-;Kras* and *Kras* cells (left); *Kras* and *A5+/-;Kras* proliferation curve showing cell number x10^4 versus time (hours) after seeding (n=3) (right). (C) Colony formation assay in *Kras* and *A5+/-;Kras* cells after cultivation in 10% FCS-containing medium (F)/ HBSS-starvation (H) (n=3) (left); representative picture of colony formation capacity in *Kras* and *A5+/-;Kras* cells after HBSS-starvation (right). (D) Phospho-AMPKa, LC3-I/ LC3-II, and p62 expression in *Kras* and *A5+/-;Kras* cells, after FCS-starvation, with/ without chloroquine treatment (CQ) (left); representative picture of colony formation capacity in *Kras* and *A5+/-;Kras* cells after CQ-treatment (right). (E) Cyto-ID fluorescence in *Kras* and *A5+/-;Kras* cells after cultivation in medium with/ without FCS (n>3). Mean±SD, **P*<0.05, ****P*<0.001. Scale bars equal 50µm

Figure 3: Monoallelic loss of *Atg5* increases metastatic properties of cancer cells *in vitro* and *in vivo*.

(A) Anoikis assay with *Kras* and *A5+/-;Kras* cells (%). (B) Quantification of migration (left), invasion (middle), and filopodia numbers/ sphere with representative picture of cell spreading/ filopodia formation in *Kras* and *A5+/-;Kras* cells (right). (C) Lung tumors after tail vein injection (i.v.) of *Kras* and *A5+/-;Kras* cells; black arrowheads indicate tumors or BrdU-positive cells (top); quantification of lung metastasis (% area) after i.v. of *Kras* and *A5+/-;Kras* cells (n=6) (bottom). (D) Western blot of Atg5-Atg12 and LC3I/II in *Kras*, *A5+/-;Kras* and *Kras* cells after 54, 58, 81, 86, 94% shRNA-mediated knockdown of *Atg5*. (E) Migration (left), invasion (right) of *Kras* versus *Kras* cells with 58, 94% knockdown (KD) of *Atg5*. (F) Quantification of lung tumor formation after tail vein injection (i.v.) of *Kras* and *Kras* cells with 58, 94% knockdown (KD) of *Atg5* (% area); representative H&E pictures are included. Mean±SD (n>3), ****P*<0.001, ***P*<0.01. Scale bars equal 50µm.

Figure 4: Monoallelic loss of *Atg5* leads to global changes in metabolism, inflammation, and vesicle homeostasis.

(A) Normalized enrichment score (NES) versus significance plot illustrating gene sets, identified by GSEA, enriched in either *Kras* or *A5+/-;Kras* pancreatic tumor cells (n=3); enriched pathways are localized beneath dotted line. (B) Functional classification of most highly regulated genes identified by GSEA in *Kras* and *A5+/-;Kras* cells (% of all significantly upregulated genes; Supplementary Figure 4C). (C) Classification of significantly enriched gene sets into categories for *Kras* (left) and *A5+/-;Kras* (right) cells (*P* value 0.0 indicates *P*<0.001). (D) Classification of significantly upregulated metabolites in *Kras* and *A5+/-;Kras* cells (left) and their supernatants (media, right); amino acids/ peptides=red, lipids=black, nucleotides/ carbohydrates=purple; Mean±SD (n=3).

Figure 5: Monoallelic loss of *Atg5* reduces mitochondrial functionality and increases ER-stress.

(A) TEM pictures of *Kras* and *A5+/-;Kras* cells (4000x, 20000x); asterisk/ black arrowhead indicate mitochondria/ mitochondrial fission. (B) Oxidative capacity (pmolO2/min) of *Kras* and *A5+/-;Kras* cells normalized to protein or DNA (ng) (n≥30). (C) Glycolytic capacity (mpH/min) of *Kras* and *A5+/-;Kras* cells normalized to protein or DNA (ng) (n=9). (D) Oxygen consumption rate (pmolO2/min/ng DNA) versus extracellular acidification rate (mpH/min/ng DNA) for *Kras* and *A5+/-;Kras* cells. (E) Mean glutamate dehydrogenase activity (GLDH, mU/mg protein) distribution into density fractions (with decreasing density from 22 to 46) in *Kras* and *A5+/-;Kras* cell extracts (n=4). (F) qRT-PCR of *Nrf1* and *Sod2* normalized to *cyclophilin* (n=3). Mean±SD, **P*<0.05, ***P*<0.01.

Figure 6: *Atg5*-dependent changes in Ca2+ signaling, extracellular cathepsin levels and filopodia formation: determinants of metastatic potential.

(A) Representative recordings (left) and amplitude (right) of cytosolic Ca2+ responses (as described in Supplementary Methods) in *Kras* and *A5+/-;Kras* cells after FBS-stimulation (at 200sec, marked with black arrowhead) (n>170). (B) S100a4 immunohistochemistry in *Kras* and *A5+/-;Kras* mice. (C) Cathepsin L (CTSL) and Cathepsin D (CTSD) extracellular activity (% extracellular activity versus total activity) as measured from supernatants of *Kras* and *A5+/-;Kras* cells (n=15). (D) Quantification of filopodia numbers/ sphere in *A5+/-;Kras* cells after E64d treatment compared to no treatment (NT) (n>3) (left); representative bright field picture of cell spreading and filopodia (right). (E) Quantification of invaded *A5+/-;Kras* cells after E64d treatment or no treatment (NT) (n>3) (left); representative picture of invaded cells (right). Mean±SD, **P*<0.05, ***P*<0.01, ****P*<0.001. Scale bars equal 50μm.

Figure 7: Lower levels of *ATG5* gene and protein levels correlate with human pancreatic cancer aggressiveness.

(A) ATG5-ATG12 protein levels in human pancreatic cancer samples (top); Kaplan-Meier survival analysis (months) with Cohort 1 patients separated into high (ATG5/ β-Actin ratio equal/ above 0,5; n=22, median survival 20,5 months) versus low-moderate (ATG5/ β-Actin ratio below 0,5; n=34, median survival 12,5 months) ATG5 expression groups (*P*=0.4479). (B) Representative ATG5 immunohistochemistry in primary human PDAC tissues separated into Score 1/ 2 (low-moderate) and Score 3 (high); asterisk/ arrowhead/ circle mark epithelial cancer/ endothelial/ islet cells. (C) Distant metastasis incidence (%) in n=23 Cohort 2 patients separated into high (n=6) versus low-moderate (n=23) ATG5 expression groups according to (B). (D) Kaplan-Meier survival analysis (days) with Cohort 3 patients separated into high (n=23, median survival 407 days) versus low-moderate (n=56, median survival 358,5 days) ATG5 expression groups according to (B) (**P*=0.0396, top); table shows lymph node infiltration (%, pN0, pN1) and resection status (%, R0, R1) (bottom). (E) Illustration of autophagy-associated DNA copy number gain (red) or loss (blue) (TCGA data) in normal versus pancreatic cancer (PC) samples; blue bars correlate to less than hemizygous, white to hemizygous, and red to more than hemizygous levels. Scale bars equal 50µm.

Figure 1:

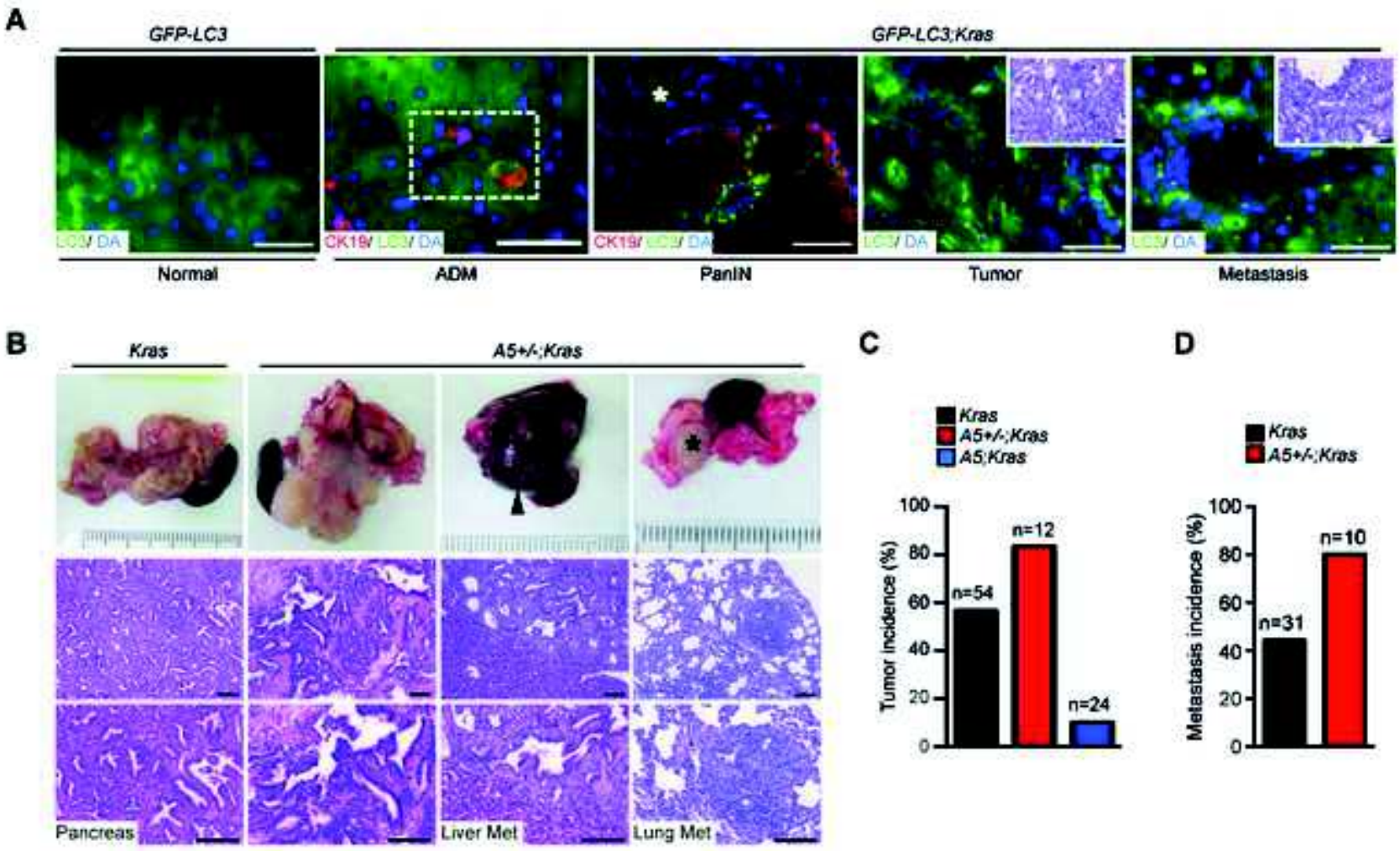

Figure

Click here to access/download;Figure;Figure 2.jpg

Figure 2:

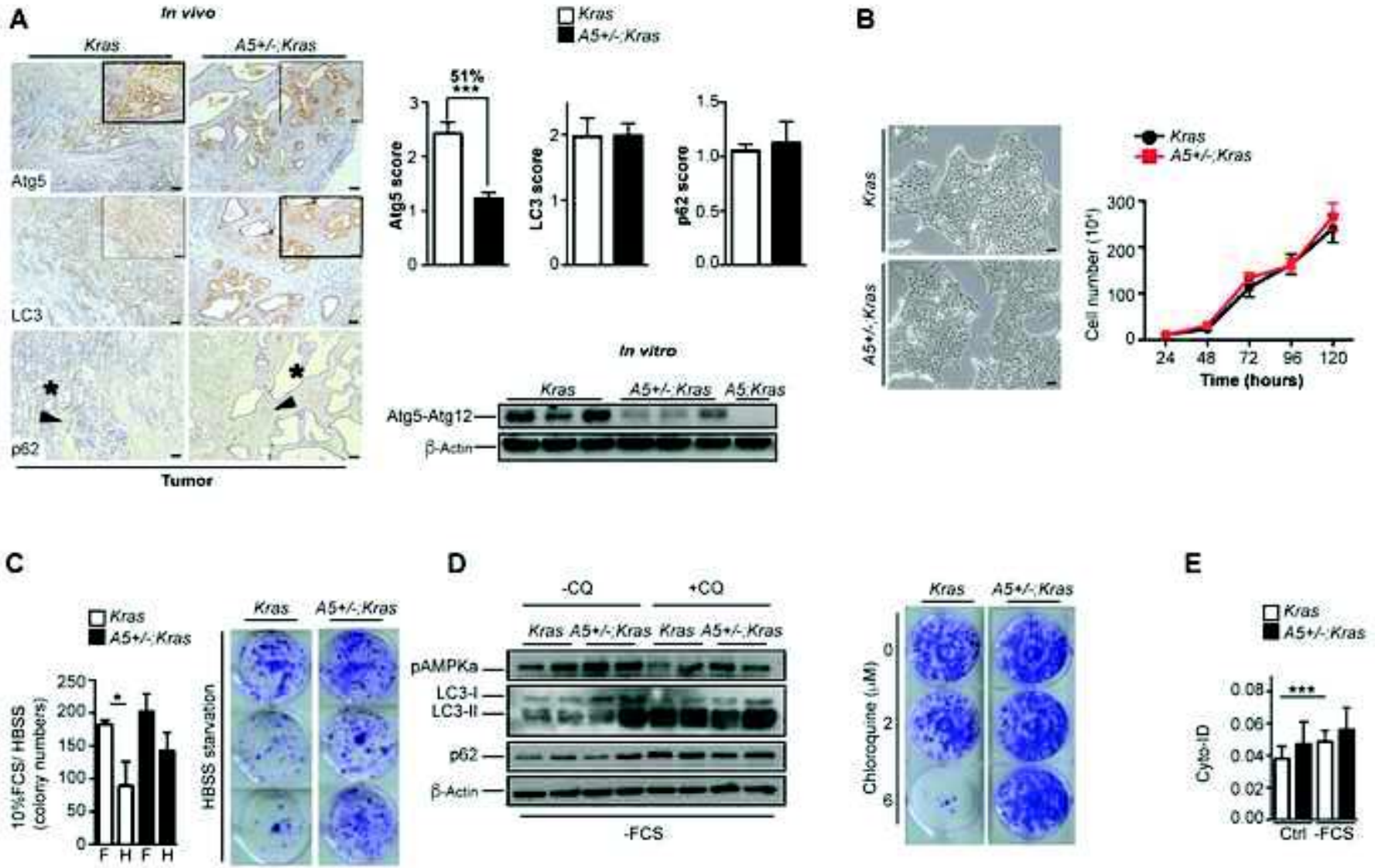

Figure 3:

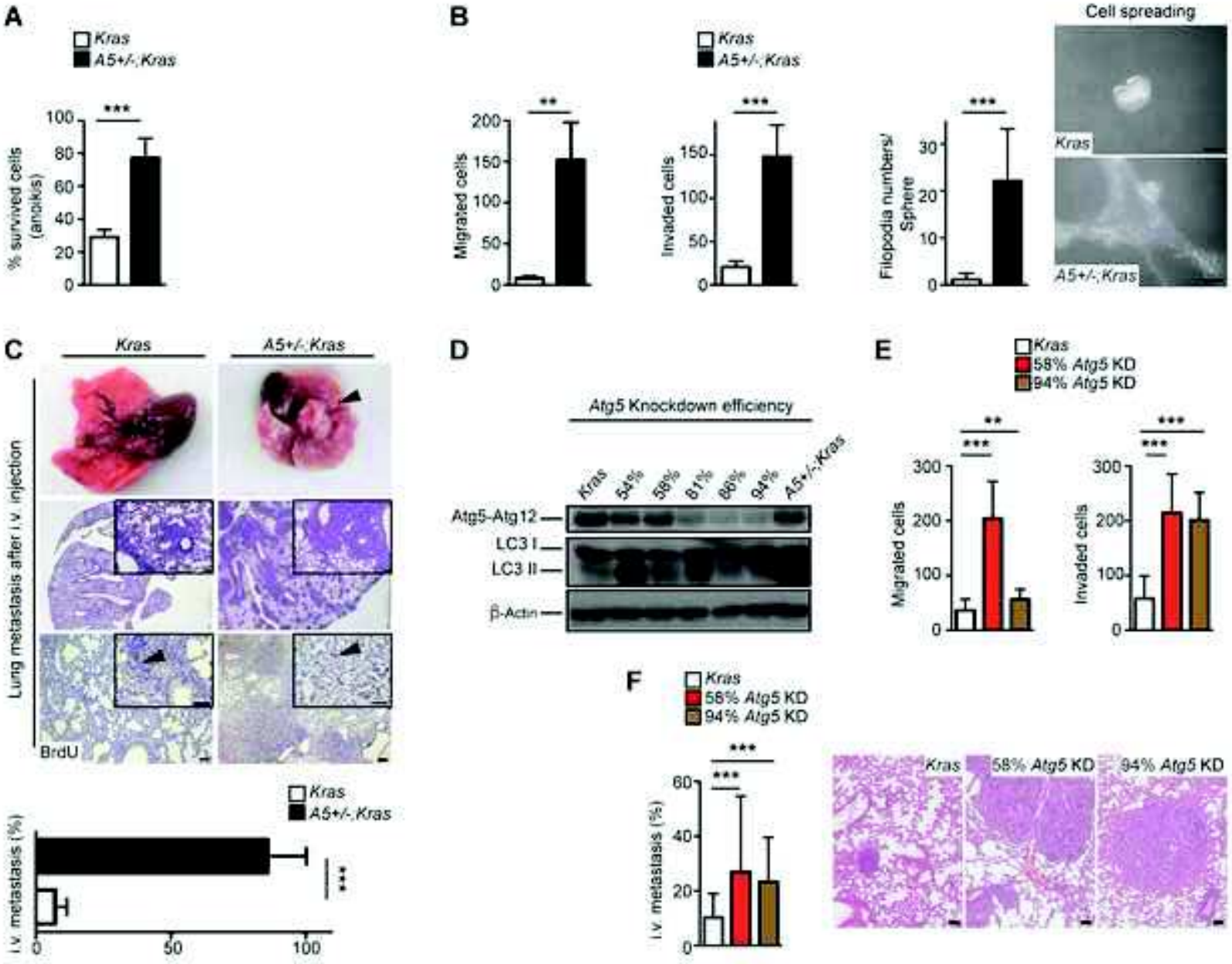

Figure

Click here to access/download;Figure;Figure 4.jpg

Figure 4:

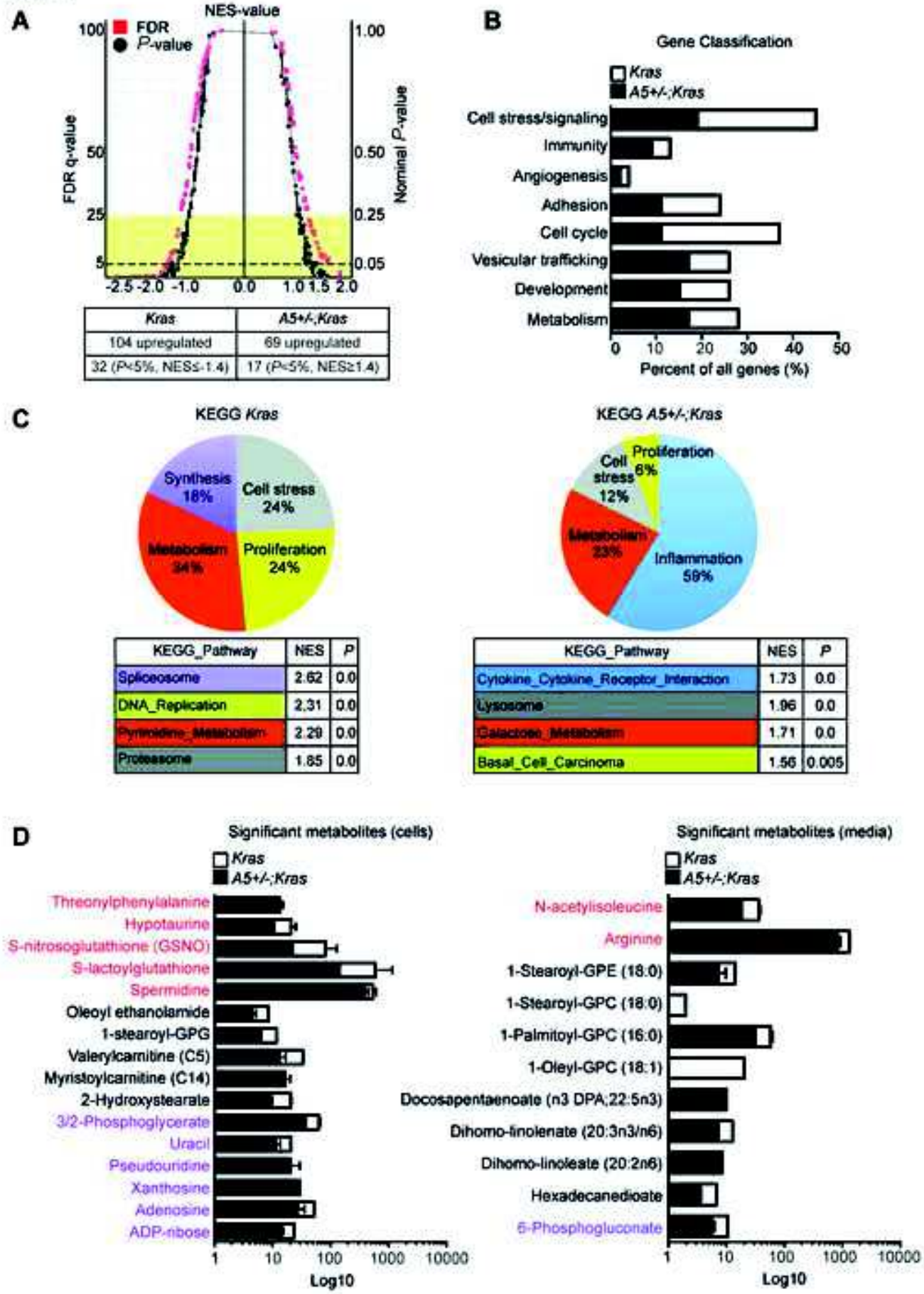

Figure

Click here to access/download;Figure;Figure 5.jpg

Figure 5:

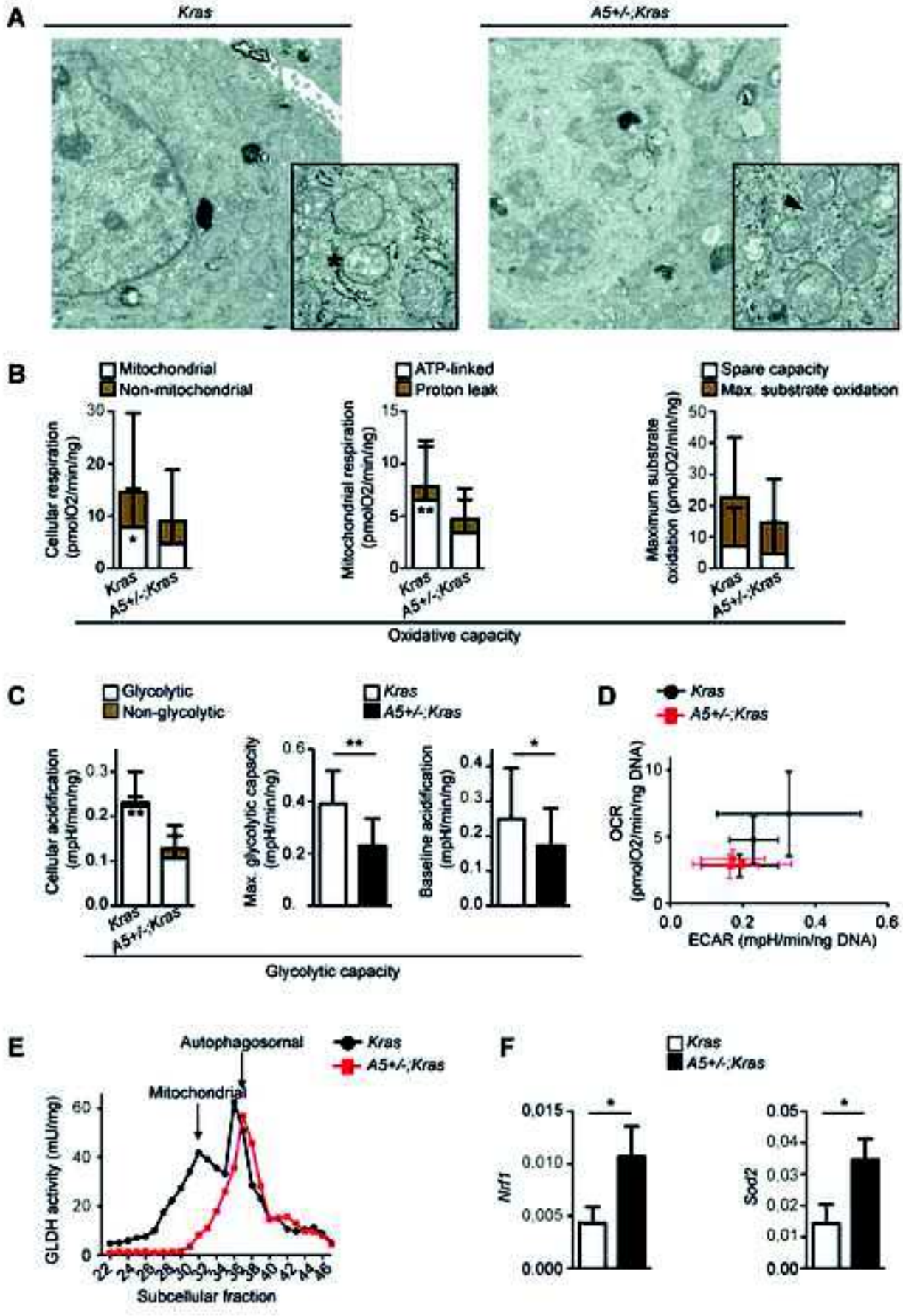

Figure 6:

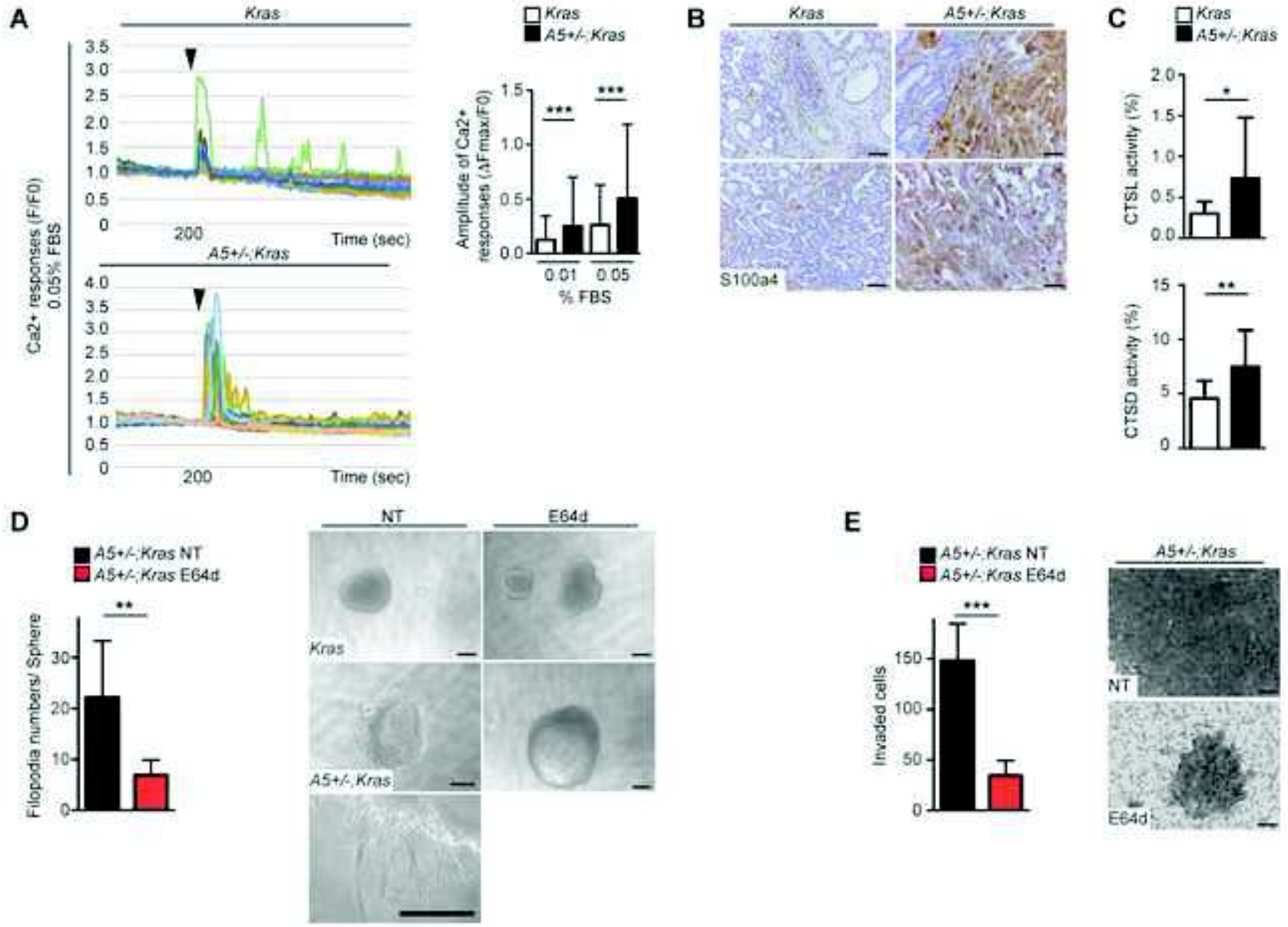

Figure 7

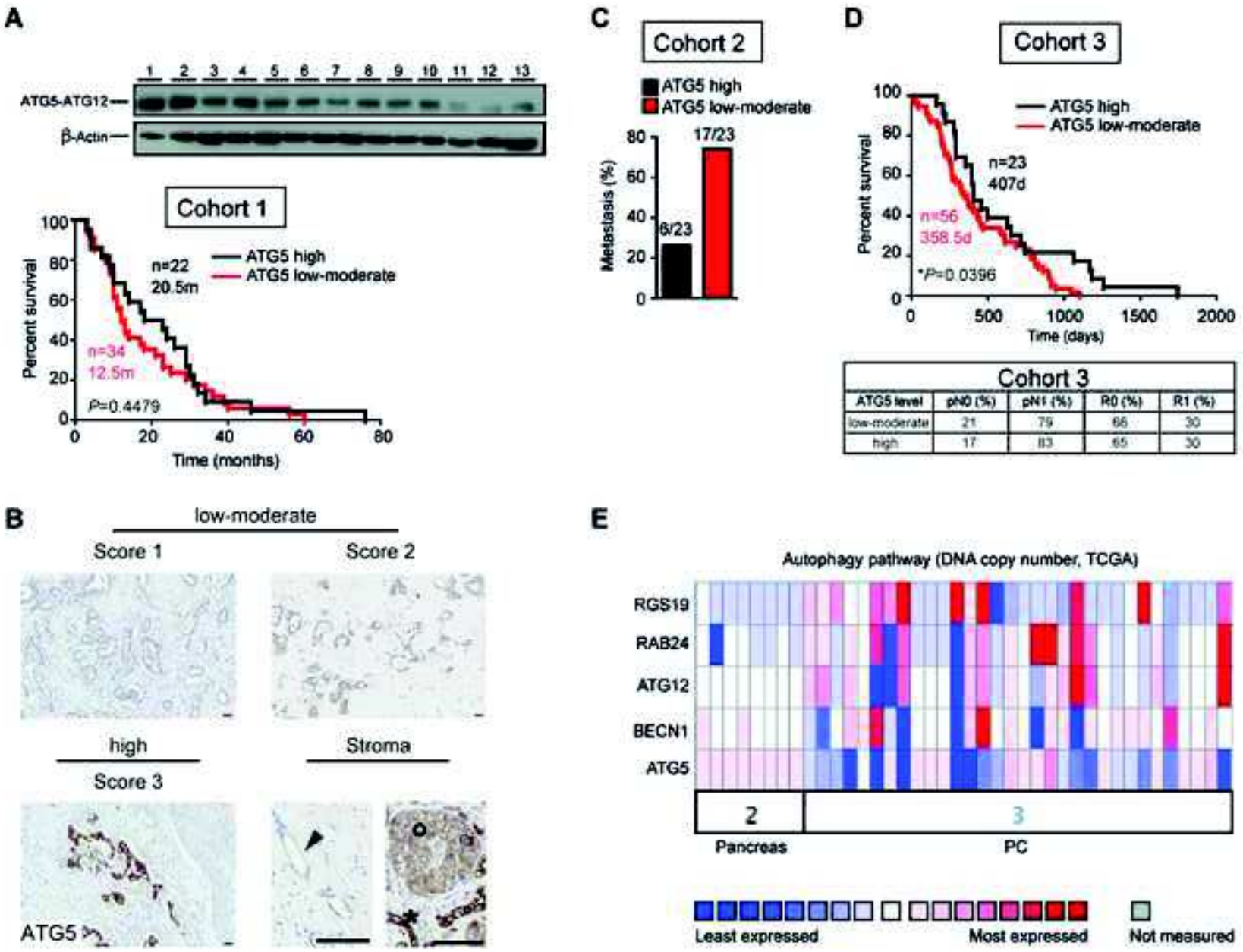

“What You Need to Know”:

Background and Context: Autophagy is considered a therapeutic target in PDAC. As the effect of autophagy pathway inhibition remains unclear, the authors investigated the role of *Atg5*, an important autophagy regulator, in PDAC.

New Findings: The authors correlate PDAC-malignancy with *Atg5* levels in mice and patients. Reduced *Atg5* levels enhance PDAC-aggressiveness *in vitro* and *in vivo* through mechanisms including cathepsin activation and pro-tumorigenic M2-macrophage infiltration.

Limitations: Reduction of *Atg5*-levels influences a multitude of cellular functions collectively promoting PDAC-progression and -metastasis. Future studies may need to analyze the exact contribution of each of these pathways in PDAC.

Impact: Autophagy pathway inhibitors are utilized in PDAC-treatment. However, caution is required as the authors for the first time correlate reduced levels of an autophagy pathway regulator with metastasis/ patient survival.

“Lay Summary”:

Monoallelic loss of *Atg5* in PDAC enhances metastatic capacities of cancer cells through activating extracellular cathepsins and attracting pro-tumorigenic M2-macrophages collectively favoring PDAC malignancy.

Supplementary Figure 1: Relating to Figure 1

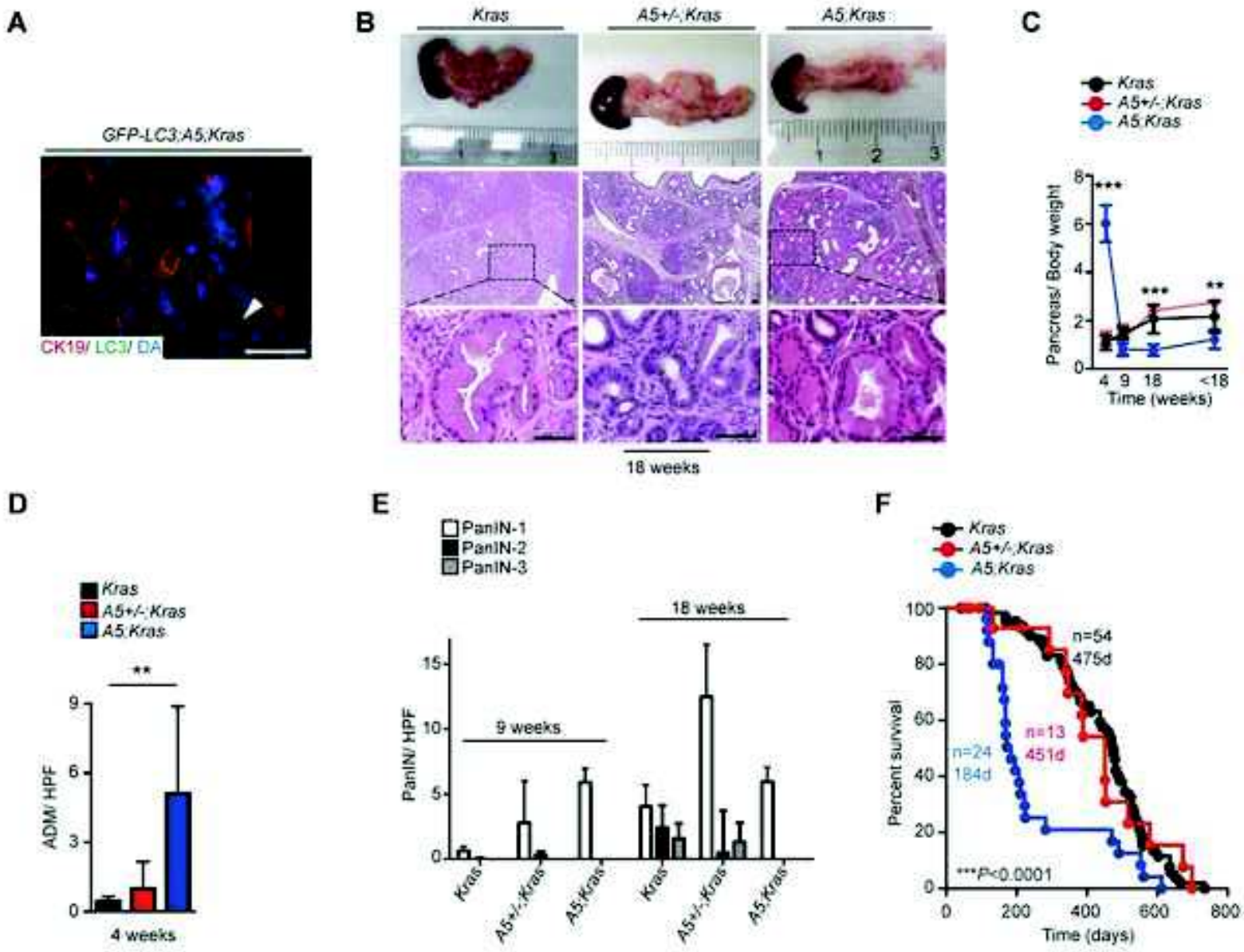

Supporting Document

Click here to access/download;Supporting Document;Supplementary Figure 2.jpg

Supplementary Figure 2: Relating to Figure 2

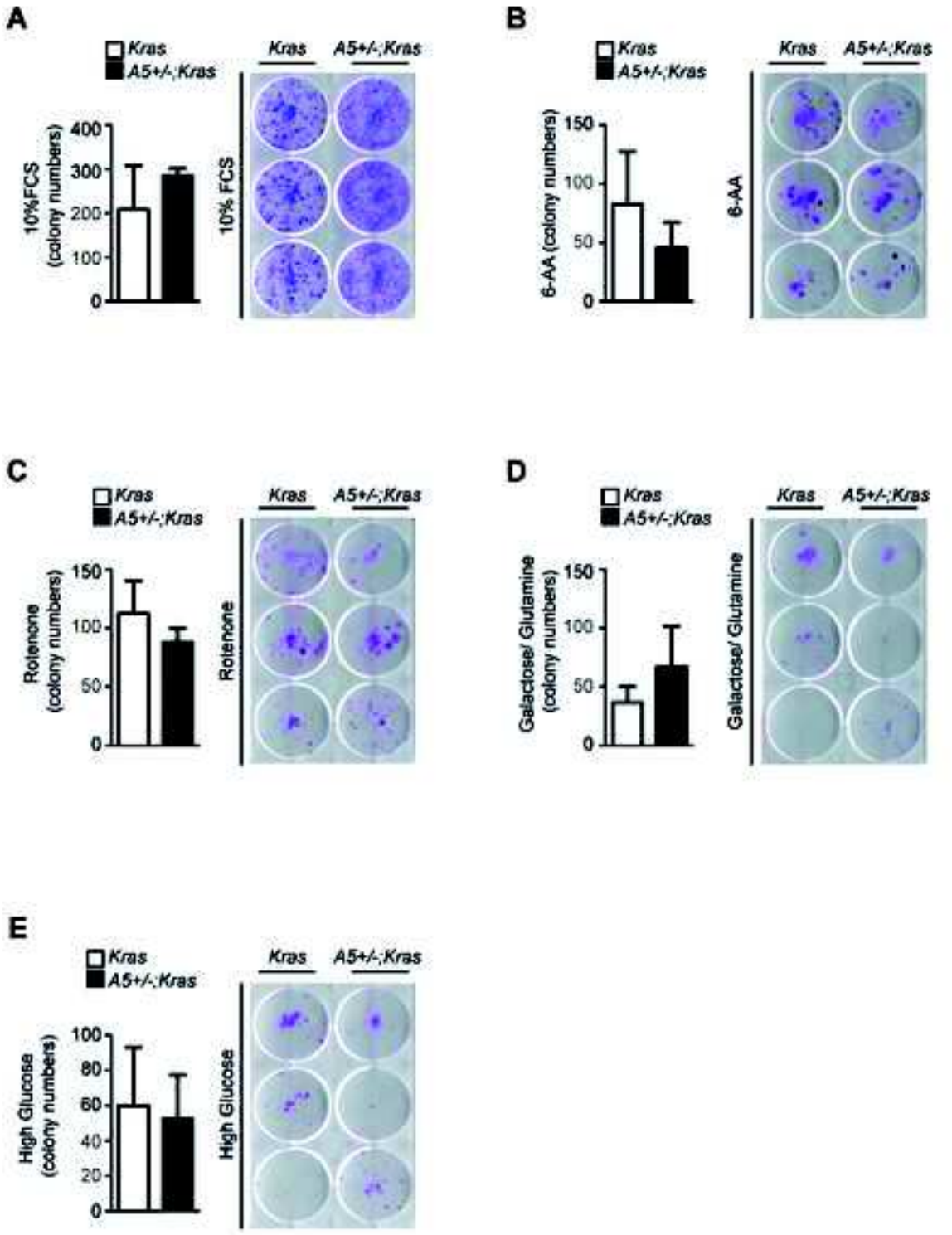

Supporting Document

Click here to access/download;Supporting Document;Supplementary Figure 3.jpg

Supplementary Figure 3: Relating to Figure 3

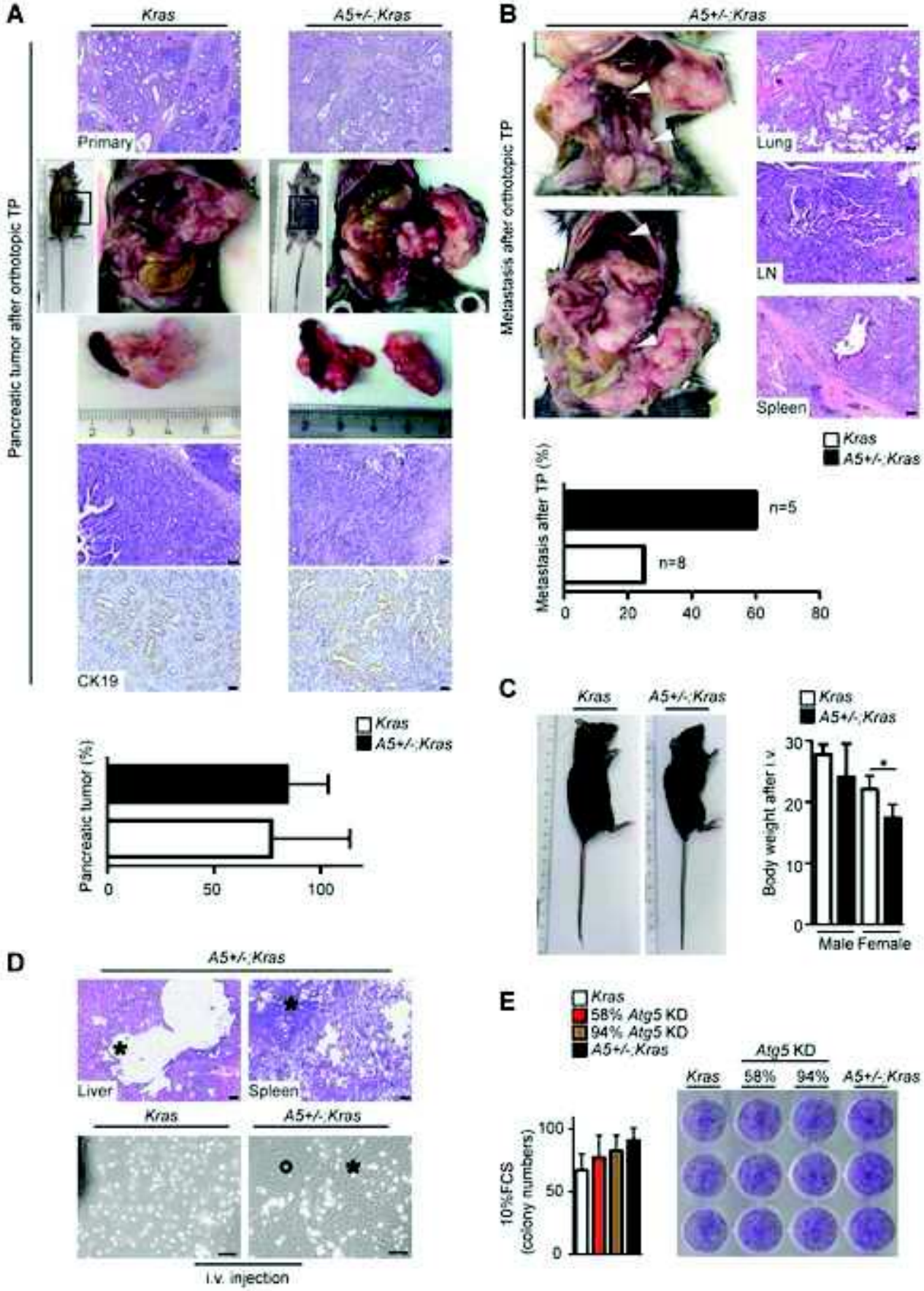

Supporting Document

Click here to access/download;Supporting Document;Supplementary Figure 4.jpg

Supplementary Figure 4: Relating to Figure 4

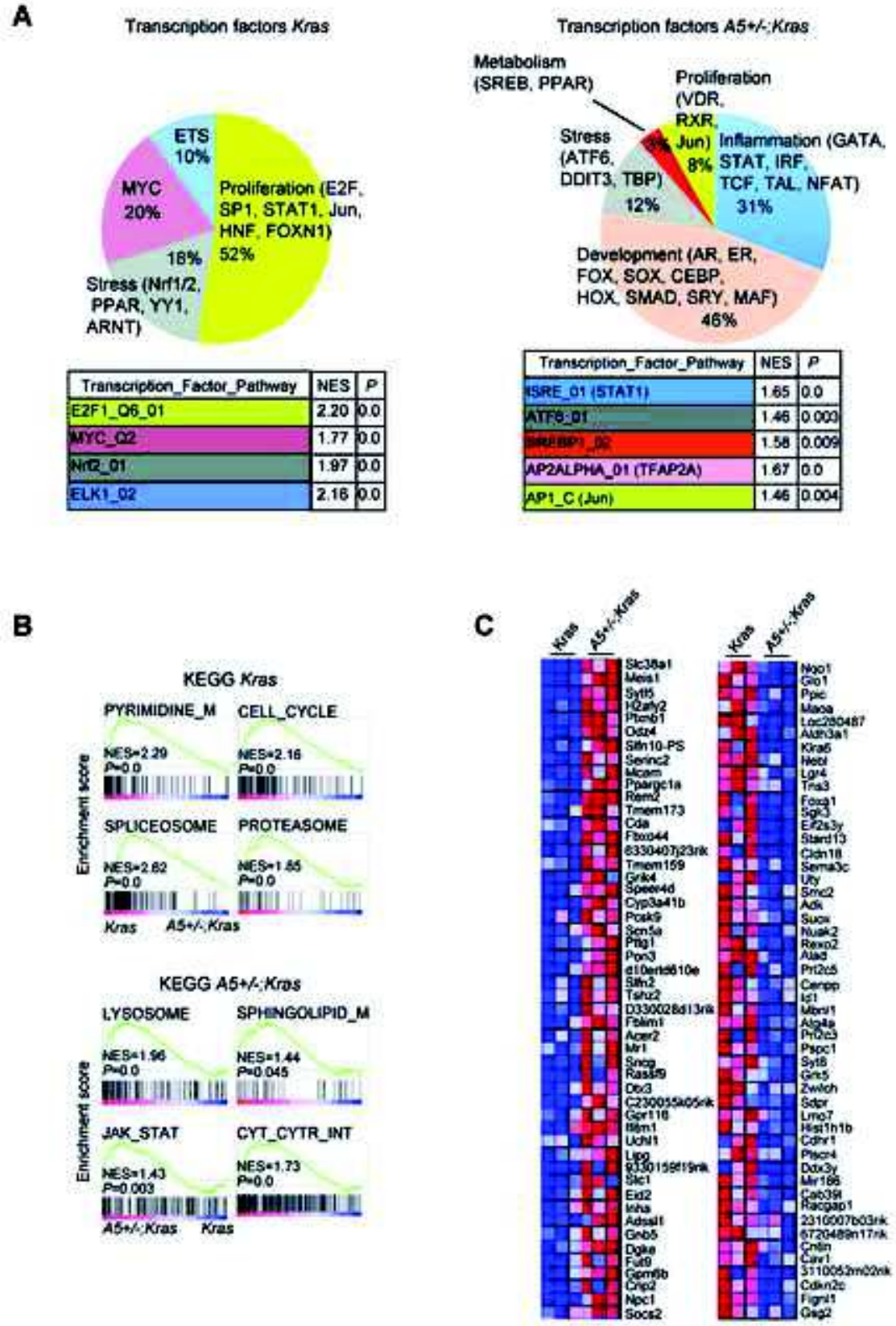

Supplementary Figure 5: Relating to Figure 5

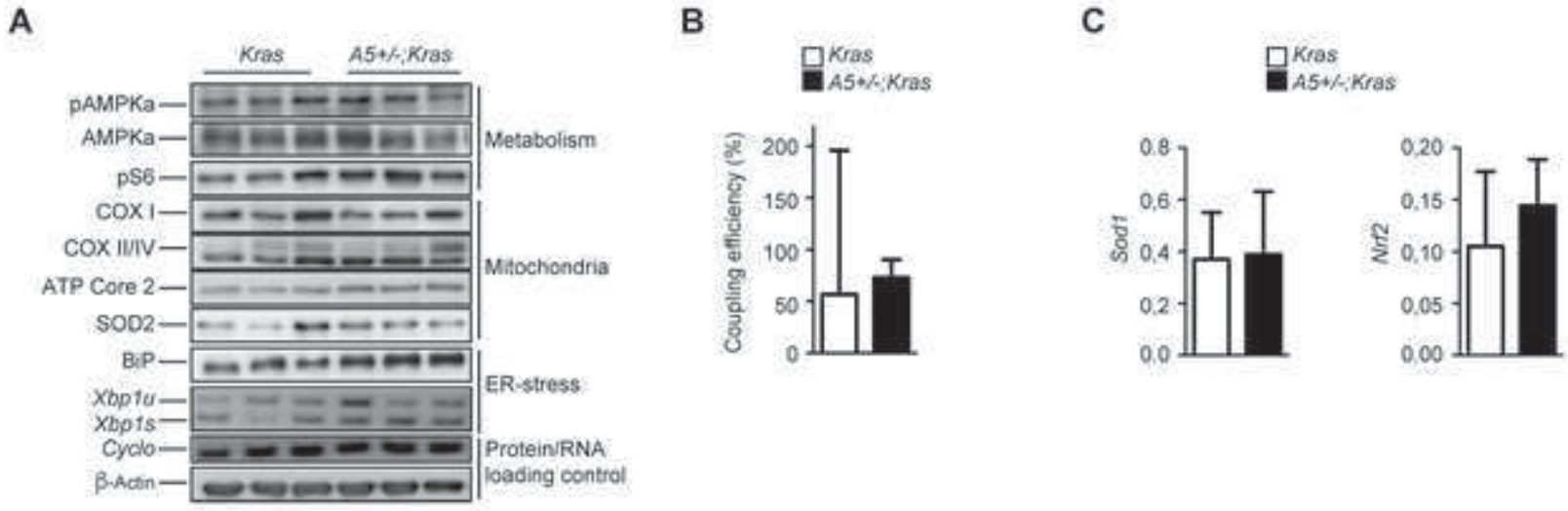

Supporting Document

Click here to access/download;Supporting Document;Supplementary Figure 6.jpg

Supplementary Figure 6: Relating to Figure 6

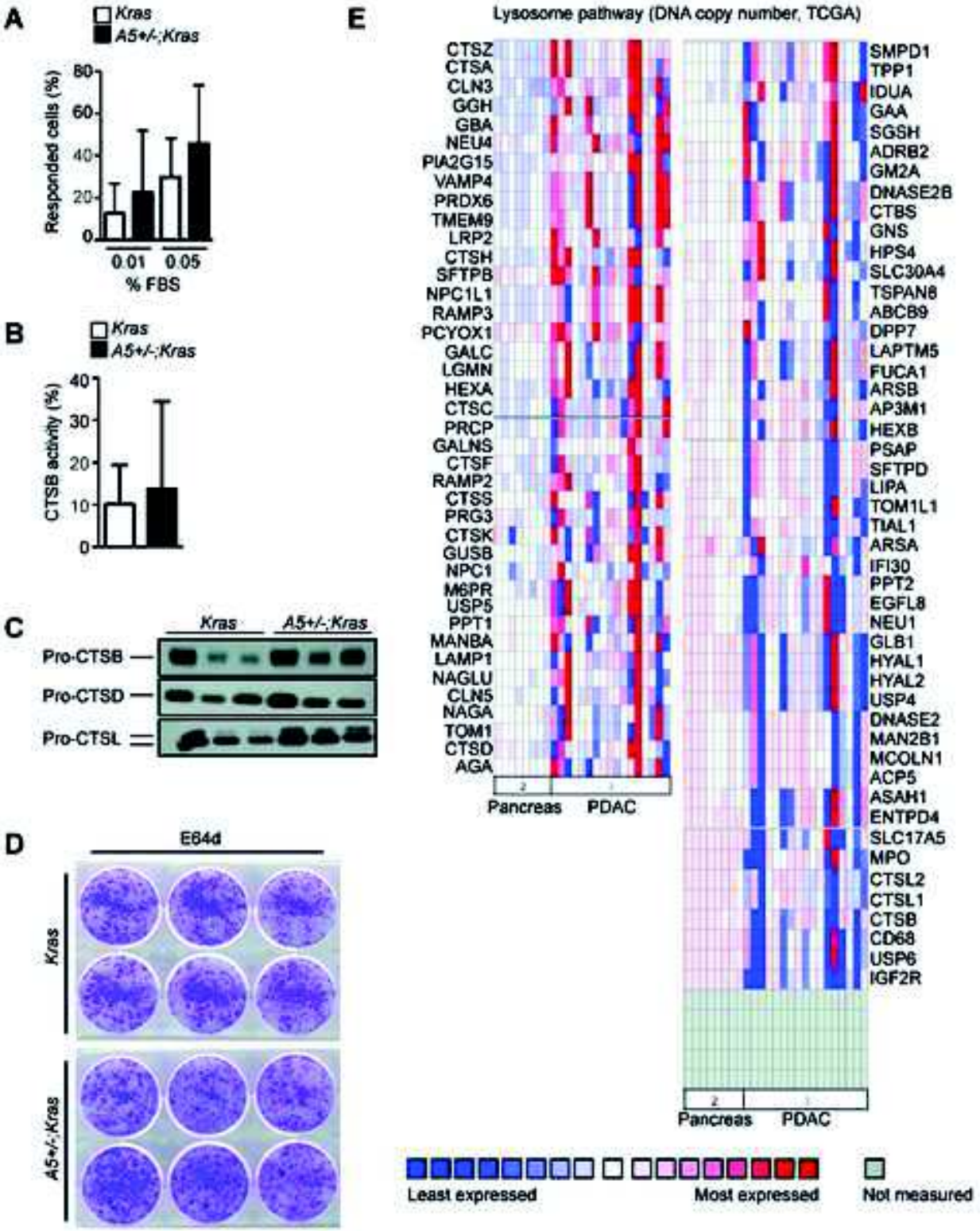

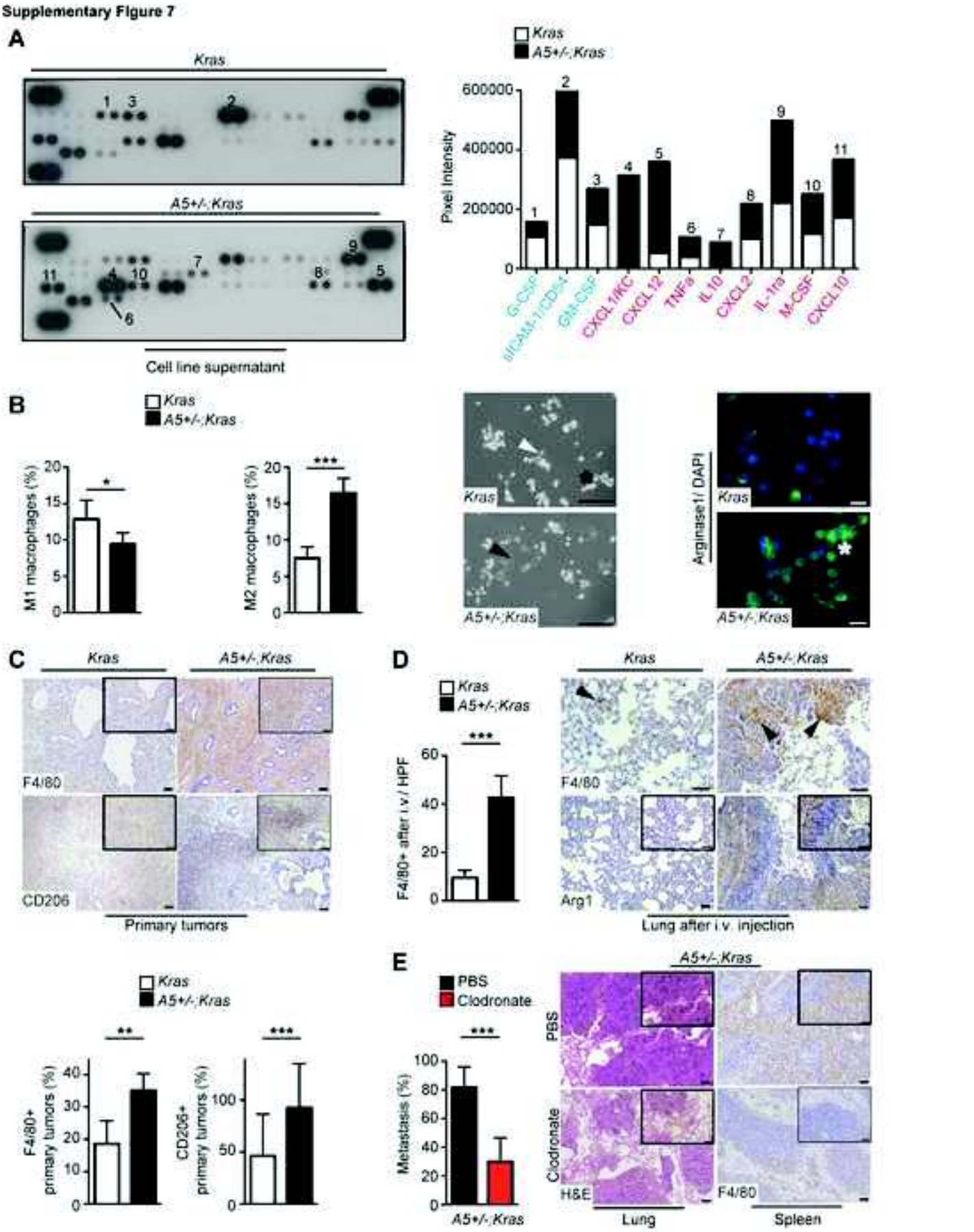

SUPPLEMENTARY MATERIALS AND METHODS:

Quantification of relative pancreatic weight, tumor incidence, and metastasis incidence

Kras, *A5+/-; Kras*, and *A5; Kras* mice were sacrificed at 4, 9, and 18 weeks of age or at the time point of sickness. Relative pancreatic weight was calculated from the pancreas and body weight obtained during sacrifice (pancreas weight/ body weight). Tumor incidence and metastasis incidence (% of tumor or metastasis-positive mice relative to all mice sacrificed) was calculated after histological examination. Metastasis-positive mice were mice with metastasis in liver, lung, or diaphragm from the pool of pancreatic tumor-positive mice. Ascites, lymph node, spleen, or kidney infiltration was also evaluated (see Supplementary Table 1).

Detection of GFP-LC3 puncta

GFP-LC3 mice with or without concomitant *Kras* expression were sacrificed after standard fed conditions. Pancreas was snap frozen in freezing medium (Tissue-Tek O.C.T. Compound, Weckert Labortechnik, Germany) and 7-10μm thick cryo-sections were mounted on adhesive-coated slides. Sections were air dried, fixed in 100% ethanol for 8 minutes at RT, washed with PBS and covered with DAPI containing mounting medium (H-1200 Vector Laboratories, CA). Sections were processed and kept in the dark until analysis. Puncta formation was detected by analysis of green fluorescence (EX/EM 470/525nm) with fluorescence microscopy (Zeiss Axiovert 200M).

Tumor cell isolation and cultivation

Primary pancreatic tumor cell lines were established from isolated murine pancreatic tumors. To establish the cell lines, pieces of pancreatic tumor tissue from *Kras*, *A5+/-; Kras*, and *A5; Kras* mice were placed in full culture medium (see below) and tumor cells were allowed to grow out of the tissue. Cell lines were routinely cultured under standard conditions (5% CO_2, 37 C) in culture media (Dulbecco's modified Eagle medium (DMEM) supplemented with 10%FBS (#10082147; Gibco), 1% PenStrep (#1500-063; Gibco), 1% Non-Essential-Amino-Acids (NEAA #11140050; Gibco)). On average, cells were passaged 5 times prior to any experiments.

Knockdown of mAtg5

Experimental procedures were followed as described previously [1]. Briefly:

Transfection of 293T cells for production of lentiviral particles

5 x 10^6 293T cells were seeded in 10 cm dishes. After one day, media was replaced and co-transfection of transfer plasmids purchased from Sigma Aldrich (TRCN0000327456 (54% knockdown, validated), TRCN0000327358 (58% knockdown, validated), TRCN0000363558 (81% knockdown, validated), TRCN0000375754 (86% knockdown, validated), and TRCN0000099432 (94% knockdown, validated)) with lentiviral packaging plasmids (pMD.GP, pRSV-rev, pMD.G) was performed using lipofectamine 2000 (Thermo Fisher Scientific). shRNA that does not target any known human or mouse gene (shNT) was used as a control. Two days later, lentiviral particles were harvested from the supernatant and frozen at -80°C.

Transduction of target cells with mATG5 knockdown constructs

Target *Kras* cells were seeded in 6 cm dishes. One day later, media was aspirated and 1 ml of lentiviral suspension was added to cells in presence of 8 µg/ml Polybrene (Sigma Aldrich). After 2 h at 37°C, 4 ml media was added. Selection of transduced cells was performed using 10 µg/ml puromycin.

Experimental analysis

Cells were tested in western blotting for Atg5, LC3, and β-Actin expression (as described below) and the knockdown percentage was confirmed. Cells with 54%, 58%, 81%, 86%, and 94% mAtg5-knockdown were further used in colony formation (full medium, 10% FCS), Boyden Chamber migration, invasion, and tail vein injection experiments as described below. Experiments were performed in triplicates.

In vitro *cathepsin activity measurements*

Activities of cathepsins B, L, and D were intra- and extracellularly assessed in cell lysates and culture media of primary pancreatic tumor cell lines. Tumor cells were separated from culture media by centrifugation at 1000 g for 10 min. Then, cell pellet and culture medium were snap frozen. After thawing tumor cells were subsequently resuspended in ice-cold homogenization buffer (5 mM MOPS pH 6.5, 250 mM sucrose, 1 mM Mg_2SO_4, 0.13% Triton X100l) and lysed by sonication. Cathepsin B and -L were determined as Ca074- and N1760-sensitive activity in assay buffer (50 mM sodium phosphate buffer [pH 5.5], 1 mM EDTA, and 1 mM dithiothreitol) using the fluorogenic substrates Z-Arg-Arg-7-amino-4-methylcoumarin A (10µM, #31213-v, Pepta Nova) and Z-Phe-Arg-7-amino-4-methylcoumarin (10µM, #3095-v, Pepta Nova), respectively. Cathepsin D activity was measured in 50 mM sodium acetate buffer pH 4.0 using the fluorogenic substrate Mca-Gly-Lys-Pro-Ile-Leu-Phe-Phe-Arg-Leu-Lys(Dnp)-D-Arg-NH2 (10µM, #3200-v, Pepta Nova). The release of 7-amido-4-methylcoumarin was kinetically monitored over 10 minutes at the excitation/emission

wavelength of 360/438 nm in a Safire microplate reader (Tecan, Grödig, Austria) by spectrofluorometry. Intra- and extracellular portions of cathepsin activities were normalized to the protein concentration in cell lysates determined by BioRad protein Assay kit.

Subcellular fractionation by isopycnic Percoll density centrifugation and measurement of GLDH activity

To analyze distribution and integrity of mitochondria in subcellular fractions pelleted tumor cells harvested from primary pancreatic tumor cells lines (produced as described above) were resuspended in HS buffer (250mM sucrose, 10 mM citric acid, 0.5 mM EGTA, 0.1 mM MgSO4 [pH 6.0]) and homogenized by 5 strokes using a Dounce homogenizer. After centrifugation at 100g post-nuclear supernatant was applied onto an isotonic 50% (v/v) Percoll/HS buffer solution (described above) at pH 7.27 and subsequently separated by isopycnic centrifugation at 50,000 g for 45 min at 4°C. After separation the percoll gradient was portioned in 46 fractions using a peristaltic pump beginning from the bottom and fractions were stored at -80°C until further use.

Activity of GLDH as a marker of mitochondrial distribution in subcellular fractions was determined spectrophotometrically at 340 nm according to $NADH_2$ oxidation with 2-oxoglutarate and NH_4^+ as a substrate by the method of E. Schmidt [2].

Immunoblotting

For immunoblotting, *Kras*, *A5+/-; Kras*, and *A5; Kras* cells were pelleted and snap frozen. Cell pellets were resuspended in ice cold protein lysis buffer (50mM HEPES pH 7.9, 150mM NaCl, 1mM EDTA pH 8.0, 0.5% NP-40 (Roche), 10% Glycerol) supplemented with protease/phosphatase inhibitors (SERVA), sonicated, and kept on ice. Extracellular proteins secreted into the culture medium were concentrated by trichloroacetic acid precipitation (TCA, final concentration 6 %) in the presence of 2% Na-deoxycholate by the method A. Bensadoun[3]. Concentration was determined by BioRad protein Assay kit and concentration of all samples was set to 4 □g/□l. All samples were cooked for 5min at 95°C in Laemmli buffer (300 mM Tris-HCl, pH 6.8, 10% (w/v) SDS, 50% (v/v) Glycerol, 0.05% (w/v) Bromphenole blue, 5% (v/v) β-mercaptoethanol) except when used for detection of mitochondrial oxidative phosphorylation complexes. Protein lysates were separated by SDS-gel electrophoresis and transferred to PVDF membranes. Following over night incubation with primary antibody at 4°C, proteins were detected using horseradish peroxidase-conjugated secondary antibodies anti-mouse (NA931V GE Healthcare Life Sciences), anti-rabbit (NA934V GE Healthcare Life Sciences) or anti-guinea pig (A7289 Sigma) and ECL reagent (Amersham). The primary antibodies used include: Anti-Atg5 (1/1000) (NB110-53818 Novus Biologicals), anti-p62 (1/1000) (GP62-C Progen), anti-LC3 (1/1000) (PD014

MBL International), anti-Cathepsin B (1/5000) (AF965, R&D Systems), anti-p53 (1/500) (NCL-p53-CM5p Novocastra), anti-Cathepsin L (1/5000) (AF1515, R&D Systems) anti-Cathepsin D (1/5000) (cs-10725, Santa Cruz Biotechnology), anti-phospho-AMPKa (1/1000) (2535 Cell Signaling Technology), anti-AMPKa (1/1000) (2532 Cell Signaling Technology), anti-phospho-S6 (1/1000) (2211 Cell Signaling Technology, anti-SOD2 (1/1000) (ADI-SOD-111 Enzo), anti-BiP (1/1000) (AB21685 Abcam), anti-MitoProfile Total OXPHOS Rodent Western Blot antibody cocktail (1/1000) (MS604 Mitosciences), □nti-β-Actin (1: 2000) (A5441, Sigma).

Histochemistry and immunohistochemistry

For proliferation analysis mice were labeled with 50μg of BrdU (B5002 Sigma) per g body weight by intraperitoneal injection and sacrificed 2h later. Pancreas was fixed in 4% (wt/vol) paraformaldehyde in PBS overnight at 4°C and embedded in paraffin wax. Tissue sections of 2μm thickness were mounted on adhesive-coated slides and stained with H&E.

For immunohistochemistry standard procedures were applied. Briefly, after deparaffinization and rehydration, heat-induced antigen retrieval with 0,01M citrate pH 6.0 was utilized. Endogenous peroxidase was blocked with 3% hydrogen peroxide for 15min at RT in the dark. Unspecific binding was blocked with 5% serum for 1h at RT. Slides were incubated with primary antibodies diluted in blocking solution over night at 4°C. Primary antibodies used include: anti-BrdU (1/250) (MCA2060 AbD Serotec), anti-F4/80 (1/100) (MF-48000 Invitrogen), anti-CK19 (1/200) (TROMA III Developmental Studies Hybridoma Bank), anti-Arginase 1 (1/500) (610708 BD Transduction Laboratories), anti-S100a4 (1/800) (13018 Cell Signaling Technology), anti-MMR/ CD206 (1/100) (AF2535 R&D systems Biotechne), anti-Atg5 (1/100) (NB110-53818 Novus Biologicals), anti-p62 (1/100) (GP62-C Progen), and anti-LC3 (1/100) (PD014 MBL International). Secondary antibodies including biotinylated anti-rabbit in goat (BA 1000 Vector), anti-mouse in goat (BA 9200 Vector), and anti-rat in rabbit (BA 4000 Vector) were applied for 1h at RT and avidin-biotin peroxidase complex for biotinylated secondary antibodies was then added according to manufacturer directions (Vector Laboratories, CA). Staining was developed with DAB reagent (Vector Laboratories, CA). For Arginase 1 and S100a4 detection Streptavidin/Biotin blocking kit (SP2002 Vector) was used during the staining procedure to reduce background, according to manufacturer instructions. Hematoxylin was used for counterstaining.

ADM and PanIN Quantifications

Paraffin-embedded tissue sections from 4-week old *Kras*, *A5+/-; Kras*, *A5; Kras* were stained for H&E and photographed at 100x magnification. The number of Acinar to Ductal Metaplasias was determined in each picture using Zeiss axiovision software. Measurements

from multiple photographs per tissue slide were summed up and expressed as ADM per High Power Field (HPF). Results were then averaged according to genotype. In a similar fashion, paraffin-embedded tissue sections from 9- and 18-week old *Kras*, *A5+/-; Kras*, *A5; Kras* were stained for H&E and photographed at 100x magnification. Pancreatic Intraepithelial Neoplasias (PanINs) were classified according to PanIN-1/-2/-3 and total numbers were expressed as PanIN/HPF. Results were then averaged according to genotype and age group.

Co-immunofluorescence

Cryo-sections of GFP-LC3 transgenic pancreas were processed as described above. Unspecific binding was blocked with 5% serum at RT and incubated over night at 4°C with the primary antibody. Anti-CK19 primary antibody (TROMA III Developmental Studies Hybridoma Bank) was diluted in blocking solution (1/200). At the following day secondary antibody anti-rat in goat Alexa Fluor 568 (1/300) (A11077 Invitrogen) was applied for 1h at RT. In the end, slides were covered with DAPI containing mounting medium (H-1200 Vector Laboratories) and analyzed with fluorescence microscopy (Zeiss Axiovert 200M).

Transmission Electron Microscopy (TEM)

For TEM *Kras* and *A5+/-; Kras* cells were collected and fixed in 2.5% electron microscopy grade glutaraldehyde in 0.1M sodium cacodylate buffer pH 7.4 (Science Services, Munich, Germany), postfixed in 2% aqueous osmium tetraoxide [4], dehydrated in gradual ethanol (30–100%) and propylene oxide, embedded in Epon (Merck, Darmstadt, Germany) and cured for 24 hours at 60°C. Pellets were cut in semithin sections and stained with toluidine blue. Ultrathin sections of 50nm were collected onto 200 mesh copper grids, stained with uranyl acetate and lead citrate before examination by transmission electron microscopy (Zeiss Libra 120 Plus, Carl Zeiss NTS GmbH, Oberkochen, Germany). Pictures were acquired using a Slow Scan CCD-camera and iTEM software (Olympus Soft Imaging Solutions, Münster, Germany)

RNA Extraction and Quantitative Real-Time Polymerase chain reaction (qRT-PCR)

For RNA extraction, *Kras* and *A5+/-; Kras* cells were collected in RLT lysis buffer (1015762 Qiagen) supplemented with 1% β-mercaptoethanol (M6250 Sigma) and snap frozen. Subsequently, RNA was extracted using the RNeasy Mini Kit (74104 Qiagen). SuperScript II Reverse Transcriptase (18064-014 Invitrogen) was used for complementary DNA (cDNA) synthesis. qRT-PCR was carried out using a StepOne Plus Real-Time PCR System (Applied Biosystems) in combination with Power SYBR Green PCR Master Mix (4368577 Applied

Biosystems). Target mRNA expression was normalized to endogenous *cyclophillin* and quantified by the delta-delta CT method. Primer sequences are provided below.
For detection of spliced *Xbp1*, cDNA was subjected to PCR with a primer set detecting both unspliced and spliced *Xbp1* (unspliced *Xbp1u* 171 bp, spliced *Xbp1s* 145 bp). PCR products were separated by agarose gel electrophoresis. *Cyclophilin* was used as control.

Gene	Forward primer	Reverse primer
Sod1	GTCCGTCGGCTTCTCGTCT	CACAACTGGTTCACCGCTTG
Sod2	ACACATTAACGCGCAGATCA	ATATGTCCCCCACCATTGAA
Nrf1	TCTCACCCTCCAAACCCAAC	CCCGACCTGTGGAATACTTG
Nrf2	TTCTTTCAGCAGCATCCTCTCCAC	ACAGCCTTCAATAGTCCCGTCCAG
Xbp1	ACACGCTTGGGAATGGACAC	CCATGGGAAGATGTTCTGGG
Cyclophilin	ATGGTCAACCCCACCGTGT	TTCTGCTGTCTTTGGAACTTTGTC

Microarray Data Analysis

For transcriptomic analysis, *Kras* and *A5+/-; Kras* tumor cells were harvested after PBS-washing in RLT lysis buffer supplemented with 1% β-mercaptoethanol, as described above. Cell suspensions were snap frozen and stored at -80°C. RNA isolation from tumor cell suspensions and Affymetrix GeneChip (*Mus musculus*) Mouse Gene 1.0 ST Array was conducted by the service facility KFB Center of Excellence for Fluorescent Bioanalytics (Regensburg, Germany, www.kfb-regensburg.de). Microarray data were analyzed by using the Gene Set Enrichment Analysis Software (GSEA) provided by the Broad Institute. A Nominal Enrichment Score (NES) of ≥1.0 and a nominal p-value of <0.05 were used to evaluate significantly upregulated pathways according to KEGG and Transcription Factor Binding Motif databases. Pathways were subsequently separated into groups depending on their description in the respective database. A heat map of the most highly regulated genes computed by GSEA was used and the genes were further classified according to their function. Genes belonging to one functional group were depicted as percentage related to the entire number of highly regulated genes. A NES versus nominal p value diagram was provided to indicate the total number of regulated (NES≥0.5) and significantly regulated (NES≥1.4, nominal p value< 0.05) pathways detected in the KEGG database. Microarray data are available in the ArrayExpress database at EMBL-EBI (https://www.ebi.ac.uk/arrayexpress/) under accession number E-MTAB-6275.

Non-targeted metabolomic measurements

LC-MS/MS–based non-targeted metabolomics analysis was conducted at the Genome Analysis Centre, Helmholtz Zentrum München as previously described [5]. About $1x10^6$

pancreatic cancer cells were required for the analysis. In brief, 0.375x10^6 *Kras* or *A5+/-; Kras* cells were seeded in duplicates in a 6-well plate with 2 ml culture medium and grown for 48h until 80-90% confluent and an approximate number of 0.5x10^6 was reached. Cells were washed two times with PBS (37°C). Dry ice cold 80% v/v methanol (400 µl) containing 4 recovery standard compounds to monitor extraction efficiency was added to the cells to cover them immediately. Cells were scraped and the cell suspension was transferred into precooled (dry ice) 2 ml screw cap micro tubes (Sarstedt Micro tube 2 ml, PP (Reference #: 72.694.005)) filled with 160 mg glass beads. Another 100 µl of dry ice cold methanol extraction solvent to wash the well was added and transferred to the micro tube. Suspensions of two 6-wells were pooled into one tube to obtain a sample of 1x10^6 cells in 1 ml cell suspension. The samples were stored immediately at -80°C until metabolomic analysis was performed. The metabolites were assigned to cellular pathways based on PubChem, KEGG, and the Human Metabolome Database. Metabolic pathways were described as significantly up- or down-regulated, when metabolites assigned to those specific pathways were increased or decreased, respectively. Values depicted correspond to the absolute values normalized in terms of raw area counts after LC/MS-based metabolomic analysis.

Oncomine database

The oncomine database (www.oncomine.org) was used to search for autophagy and lysosomal function-associated genes. GO Biological Process-Autophagy or GO Cellular Component-Lysosome was used as concept; primary filters selected were Cancer versus Normal Analysis and Pancreatic Cancer; pathology subtypes M1+, N1+, T4 according to TNM-staging were subsequently applied. DNA Copy Number (log2 copy number units) retrieved from the Cancer Genome Atlas (TCGA Research Network, http://cancergenome.nih.gov/) was used to illustrate copy number gain or loss in human pancreatic cancer samples versus normal pancreas samples.

Measurement of mitochondrial metabolism by seahorse analyzer

Measurements of oxygen consumption rate (OCR) were performed with a XF extracellular flux analyzer as described previously (Oelkrug R, Goetze N, Exner C, Lee Y, Ganjam GK, Kutschke M, Muller S, Stohr S, Tschop MH, Crichton PG, Heldmaier G, Jastroch M, Meyer CW. Brown fat in a protoendothermic mammal fuels eutherian evolution. Nature communications 2013;4:2140). Briefly, *Kras* and *A5+/-;Kras* tumor cells were seeded at a density of 1X10^5 cells per well in a XF24 cell culture microplate. DMEM (4.5 g/L glucose, +L-Glutamine, -Pyruvate, pH 7.6 at RT) supplemented with 10% heat inactivated FBS (Gibco)

and 1% Pen/Strep was used for cell culturing. On the day of assay (24h after seeding), medium was exchanged to non-carbonated Seahorse measurement medium and the XF24 plate was transferred to a temperature-controlled (37 °C) XF24 Extracellular Flux analyzer (Seahorse Bioscience) and equilibrated for 10 min. To determine the basal respiration four assay cycles (1-min mix, 2-min wait and 3-min measuring period) were used. Then oligomycin (4 μ M) was added by automatic pneumatic injection (three assay cycles) to inhibit ATP synthase and thus approximate the proportion of respiration used to drive ATP synthesis versus proton leak-linked respiration. Oligomycin was followed by an injection of FCCP (carbonyl cyanide p-trifluoromethoxyphenylhydrazone) (0.5 μ M) to completely dissipate proton motive force and maximally stimulate mitochondrial respiration (three assay cycles), thus determining spare respiratory capacity and substrate oxidation capacity. An injection of rotenone (4 μ M) and antimycin A (2 μ M) was used to correct for the non-mitochondrial respiration rate (three assay cycles), which was subtracted from all the other rates. Coupling efficiency was calculated as the oligomycin-sensitive fraction of mitochondrial respiratory activity, estimating the proportion of basal respiration used to drive ATP synthesis. To determine extracellular acidification rates (ECARs) for glycolysis, experiments were ended by injection of 2-DG (2-deoxy-D-glucose, 100 mM), correcting for non-glycolytic acidification. Injection of 2-DG enabled calculation of glycolytic acidification. Data obtained after oligomycin treatment induce glycolytic capacity. OCR was plotted against ECAR to illustrate oxidative versus glycolytic metabolism in cancer cells. Raw data were normalized to either protein or DNA content (ng).

Cell morphology analysis and quantification of cell proliferation

To analyze cell morphology, *Kras* and *A5+/-; Kras* were seeded in 6-well plates. 24h after seeding, pictures were acquired with the Zeiss Axiovision Imager A1 using a magnification of 100x. For quantification of proliferation, $5x10^4$ *Kras* and *A5+/-; Kras* cells were seeded per well in a 6-well plate. The culture media was changed every other day. Cells were counted after trypsinization every 24 hours up to 120 hours using the neubauer counting chamber. Full medium Dulbecco's modified Eagle medium (DMEM) supplemented with 10%FBS (#10082147; Gibco), 1% PenStrep (#1500-063; Gibco), 1%NEAA (#11140050; Gibco) was used for cell culture.

Autophagic flux measurement using Cyto-ID

To analyze autophagosome accumulation, *Kras* and *A5+/-; Kras* were seeded in triplicates in 96-well plates and allowed to adhere overnight. Half of the cells were kept in full medium and compared to cells cultivated overnight in serum-free medium. Autophagosome accumulation was analyzed by using the CYTO-ID Autophagy Detection Kit (Enzo, ENZ-51031) according

to the manufacturer's instructions. Fluorescence was detected using a Varioscan Lux (Thermo scientific) microplate reader.

Colony formation and cell treatments

For the cologenic assay, $3x10^2$ *Kras* and *A5+/-; Kras* cells were plated in triplicates six-well plates and grown for 10d in culture media. Colonies were stained with 2% crystal violet (C3886; Sigma), washed with water, and their area was quantified using ImageJ. Treatments during the clonogenic assays include: 10% FCS-containing medium, serum-free HBSS-containing medium (Hanks´Balanced Salt Solution GIBCO-14025092, 1:20 dilution of normal medium), chloroquine in full medium (2μM and 6 μM, C6628 SIGMA), 6-Aminonicotinamide in full medium (10μM and SIGMA-A68203), Rotenone in full medium (15nM and SIGMA-R8875), Galactose and Glutamine in glucose free medium (Galactose 10mM and Glutamine 4mM, D-(+)-Galactose, SIGMA-G5388 and GlutaMAX-I, GIBCO-35050061, DMEM, no glucose, GIBCO-11966-025), High Glucose in glucose free medium (25mM and GIBCO-A2494001).

Anoikis assay

For the anoikis assay, 6-well plates were coated with poly-HEMA (20mg/ml) (P3932; Sigma) dissolved in 96% ethanol. $5x10^5$ *Kras* and *A5+/-; Kras* cells were seeded in triplicates and cultured for 48h in culture media. Surviving cells in the media were calculated using the neubauer counting chamber.

Boyden Chamber Migration Assay

$1.5x10^5$ *Kras* and *A5+/-; Kras* cells were seeded in triplicates in 6-well plates till confluence. 100 μL serum free medium was added to upper chamber and 200 μL cells were added to chamber ($2.5x10^5$/mL in serum free medium). 750 μL full medium was added to lower chamber. Boyden-Chamber Assay plate was incubated at 37ºC for 12-16 hours. After incubation, medium was removed from upper chamber and chambers were washed twice with PBS. Cells were fixed with formaldehyde (3.7% in PBS) for 2 minutes and washed with PBS twice. To permeabilize cells, 100% methanol was added to chambers for 20 minutes. After removing methanol chambers were washed twice with PBS. Chambers were place into wells and stained with Giemsa at room temperature for 15 minutes. After removing Giemsa solution, chambers were washed twice with PBS. Non-migrated cells were scraped off with cotton swabs from the membranes. Migrated cells were counted under a light microscope.

Invasion assay

6.5mm Transwell (#CLS3464; Sigma, Corning Costar, USA) with 8.0 μm Pore polyester

membrane insert was used in 24-well culture plates. The upper surface of the membrane was coated with 100µl mixed matrigel (corning Life Sciences) per well. The matrigel was incubated at 37°C for gelling. 5x10^4 *Kras* and *A5+/-; Kras* cells were seeded in triplicates with 200µl serum-free DMEM in the upper chamber. The lower chamber was filled with 750 µl of culture media. After 48h, the cells were fixed by formaldehyde 3.7% in PBS, permeabilized with 100% methanol and stained with crystal violet. Cells that invaded to the lower surface area of the membrane were calculated by counting stained cells. E64d (100 µM and E3132-SIGMA) was used to inhibit cathepsin activity. Filopodia were quantified after 36h of seeding.

Orthotopic Transplantation

Littermates of *A5+/-; Kras* mice 8 weeks of age were injected orthotopically into the pancreas with 1×10^6 of either *Kras* or *A5+/-; Kras* tumor cell suspensions (resuspended in a solution of Matrigel (Corning 354234)/ DMEM without supplements in a ratio of 4/1) using a 26G needle. The mice were sacrificed 30 d after injection, or earlier when they reached sickness criteria. Pancreatic tissues were collected, embedded in paraffin and stained with haematoxylin and eosin (H&E). Lung, liver, lymph nodes, kidney, spleen, and duodenum were also collected and processed in the same way. Occurrence of tumors and metastasis was quantified and representative macroscopic and microscopic pictures were taken.

Tail vein injection

Littermates of *A5+/-; Kras* mice 8 weeks of age were injected intravenously through the tail vein with 1×10^6 of either *Kras* or *A5+/-; Kras* tumor cell suspensions (resuspended in 0,9% saline solution) using a 26G needle. The mice were sacrificed 20 d after injection, or earlier when they reached sickness criteria. The lungs were collected, embedded in paraffin and stained with haematoxylin and eosin (H&E). Mice were classified as metastasis positive or negative and representative macroscopic and microscopic pictures were taken. Body weight at time of sacrifice was measured to establish levels of cachexia. Metastatic tumor cells were re-isolated from pieces of lung tissue to determine cell morphology and survival capacity.

Liposomal clodronate treatment

For macrophage depletion in wildtype mice, clodronate-loaded liposomes (CP-010-010, Liposoma) were used. As control, mice were injected with control liposomes (PBS). For the experiment, mice were injected intraperitoneally (ml/ mouse) as follows:

Prior to tail vein injection	After tail vein injection

Day -8	Day -4	Day 0	Day 4/ 8	Day 12/16	Day 20
0.2 ml	0.2 ml	0.1 ml	0.1 ml	0.1 ml	0.1 ml

Clodronate and PBS treated mice were injected with *A5+/-;Kras* cells (biological duplicates) into the tail vein (at Day 0 according to the scheme above) to analyze the influence of macrophages on metastasis in the lung. Experiments were performed with at least 5 mice per group. Mice were sacrificed 21 days after tail vein injection due to sickness. Spleens of mice were analyzed after the experiments for F4/80 immunohistochemistry as described above. Lung metastasis was quantified as described below.

Cytokine array

In order to detect cellular cytokine profile supernatants of *Kras* and *A5+/-; Kras* cells were collected and processed as described above for immunoblotting. Lysates were then used according to the manufacturer's instructions (Mouse Cytokine Array Panel A, Catalog Number ARY006, R&D Systems). Pixel intensity of individual plots was quantified using ImageJ software. The average of two spots corresponding to one cytokine was used to compare cytokine profile according to genotype.

Macrophage differentiation assay

To detect the effect of *Kras* and *A5+/-; Kras* cells on macrophage phenotype, *Kras* and *A5+/-;Kras* cells were seeded in 6-well plates and cultivated for 48h. Supernatants were collected and applied on Raw macrophages (RAW 264.7 (ATCC® TIB-71™) cultivated in Dulbecco's modified Eagle medium (DMEM) supplemented with 10%FBS (#10082147; Gibco), 1% PenStrep (#1500-063; Gibco), 1%NEAA (#11140050; Gibco). Macrophage phenotype was monitored and assessed by microscopy as described [6].

For Arginase-1 Immunofluorescence macrophages were treated as described above and subsequently stained with anti-Arginase 1 (1/500) (610708 BD Transduction Laboratories). Briefly, unspecific binding was blocked with 5% serum at RT and cells were incubated over night at 4°C with the primary antibody. At the following day secondary antibody anti-mouse in goat Alexa Fluor 488 (1/300) (A-11001 Invitrogen) was applied for 1h at RT. In the end, slides were covered with DAPI containing mounting medium (H-1200 Vector Laboratories) and analyzed with fluorescence microscopy (Zeiss Axiovert 200M).

Measurement of Ca2+ responses

To measure Ca2+ responses, *Kras* and *A5+/-;Kras* cells were loaded with Fluo-4 by incubation with Fluo-4/AM (5μM) for 60min at room temperature (approximately 23°C) in Na-Hepes-based solution (140mM NaCl, 4.7mM KCl, 1.13mM $MgCl_2$, 10mM HEPES, 10mM

Glucose, 1.8mM $CaCl_2$, pH7.4). After that cells were washed by perfusion (gravity-based perfusion system) with the Na-Hepes-based solution and imaged every 2sec over a time period of 800sec using a Zeiss 510 confocal made (excitation 488nm, emission LP505). Heat Inactivated FBS (0.01% or 0.05% diluted in the Na-Hepes-based solution) was applied when 200sec of recording were reached.

Fluorescent responses (F) were normalized to fluorescence F_0 recorded before the addition of FBS (average fluorescence value for measurements recorded during 190 - 200sec time interval). Amplitude of cytosolic Ca2+ responses was determined by the equation $((F_{max}-F_0)/F_0=\Delta F_{max}/F_0$, with F_{max} corresponding to the maximum Fluo-4 fluorescence measured during the 200-500sec interval. Amplitude of cytosolic Ca2+ responses of each single cell over 5min of FBS application was measured and the amplitudes were then averaged for each genotype (n > 170 cells for each genotype).

Cells responding to FBS were defined as cells exciding 20% elevation threshold of normalized fluorescence (F/F_0) in the first 5min of FBS application.

Quantification of primary tumor and metastasis burden (iv and orthotopic TP; also with liposomal clodronate treatments)

For quantification of primary tumor and metastasis burden (in all orthotopic transplantation and tail vein injection experiments) 2 μm-tissue slices were stained with H&E. Per H&E slide multiple pictures at 100x magnification were taken. Area (μm^2) of tumor foci in pancreas and/ or lung tissues was calculated and expressed as % to all tissue area using a proprietary software package (Zeiss Axiovision, Oberkochen, Germany). Statistical analysis was done in between the genotypes (mean ± standard deviation (SD), Student t test).

Quantification of F4/80-positive and CD206-positive macrophages

For quantification of F4/80-positive macrophages in the lungs of tail vein-injected mice, tissue sections were stained for F4/80 via immunohistochemistry, as described above. Sections were subsequently photographed at 200x magnification. Number of positive cells was determined with Zeiss axiovision software. Sum from multiple photographs per tissue slide were generated and expressed in relation to the number of high power fields counted. Results were then averaged by genotype.

F4/80-positive and CD206-positive macrophages were also quantified in the original tumors of *Kras* and *A5+/-;Kras* mice. For this, tissue slides were stained with the respective antibodies and the % of positive nuclei/ all nuclei were determined.

Human sample analysis

For ATG5 immunoblotting, a total of 67 human PDAC samples (Supplementary Table 2, Cohort 1) collected from the MTBIO tissue bank of the Institute of Pathology at the Technical University Munich, were analyzed as described above. Band density was quantified by using ImageJ and normalized to β-Actin. From these 67 patients, n=56 with known survival were grouped into ATG5 low-moderate expression (ATG5/ β-Actin ratio below 0,5) and high expression (ATG5/ β-Actin ratio equal/ above 0,5) and used for Kaplan-Meier survival analysis with GraphPad Prism.

For ATG5 immunohistochemistry, two different cohorts (Cohort 2 and Cohort 3) were used. Cohort 2 consisted of 26 primary PDACs and their corresponding distant metastases that were resected between 2008 and 2013 at the University Hospital Heidelberg (Supplementary Table 3). The use of this tumor cohort for biomarker analysis has been approved by the ethics commission of the Klinikum rechts der Isar, Technische Universität München (403/17S). Primary tumor samples were used for ATG5 immunohistochemistry as described below for Cohort 3 and 19 of these were evaluated as described below for Cohort 3. In this analysis 4 patients from the Cohort 3 also exhibiting distant metastasis were included as well. The percentages of patients with distant metastasis in the low-moderate and in the high ATG5-expressing groups were calculated as described below for Cohort 3.

Cohort 3 consisted of a patient cohort with primary resected PDACs. The cohort was investigated previously in several studies [7-9] and included 200 individuals (Supplementary Table 4) that received partial pancreatoduodenectomy for PDAC between 1991 and 2006 at the Charité University Hospital Berlin. The use of this tumor cohort for biomarker analysis has been approved by the Charité University ethics committee (EA1/06/2004).

Tissue microarrays of both IHC cohorts were generated as previously described [7, 10]. In detail three tumor cores (diameter 1.5 mm) of representative tumor areas selected by a board certified pathologist on H&E stained slides were punched out of formalin-fixed paraffin embedded (FFPE) tissue blocks and arranged in a newly generated paraffin block. TMAs were made using a tissue microarrayer (Beecher Instruments, Sun Praierie, USA). Staging of both cohorts followed the WHO recommendations at the time of cohort generation (TNM-classification of the 7th edition). Clinical and demographic information was obtained from the respective institutional patient databases, by reviewing medical charts and pathological reports. Patient follow-up data were obtained from clinical records and via direct contact with patients and/ or their relatives. For Immunohistochemistry, 2µm sections prepared with a rotary microtome (HM355S, ThermoFisher Scientific, Waltham, USA) were collected from 134 patients in this cohort (Supplementary Table 3). Immunohistochemistry was performed using a Bond RXm system (Leica, Wetzlar, Germany, all reagents from Leica) with a primary antibody against ATG5 (NB110-53818 Novus Biologicals). Briefly, slides were deparaffinized using deparaffinization solution, pretreated with Epitope retrieval solution 1 (corresponding to

citrate buffer pH 6) for 20 minutes. Antibody binding was detected with a polymer refine detection kit without post primary reagent and visualized with DAB as a dark brown precipitate. Counterstaining was done with hematoxyline. The membranous ATG5 was scored according to the percentage and intensity of positive cells on a 0 to 3+ scale (negative as score 0, faint expression as score 1+, moderate expression as score 2+ and strong expression as score 3+; see Figure 7B for a panel of staining). Kaplan-Meier survival analysis was performed by GraphPad Prism with a total of 79 patients from the 134. Patients with no available survival and patients with no death follow up were removed from the analysis. The two groups in the Kaplan-Meier analysis included low-moderate ATG5-expressing patients (with scores 1 and 2) and high ATG5-expressing patients (score 3). Lymph node status and resection status in these patients was expressed as % patients referring to the total patients belonging to the two groups.

An overview of the three different cohorts used can be found in the following table:

Cohort number	**Status**	**Site**	**Analysis**	**Number of patients**
1	Postoperative	Primary	Western blot	56
2	Palliative/ metastatic	Primary	IHC	23
3	Postoperative	Primary	IHC	79

SUPPLEMENTARY REFERENCES:

1. Cui H, Seubert B, Stahl E, et al. Tissue inhibitor of metalloproteinases-1 induces a pro-tumourigenic increase of miR-210 in lung adenocarcinoma cells and their exosomes. Oncogene 2015;34:3640-50.
2. Schmidt EaS, F.W. Methods of Enzymatic Analysis. Weinheim: Verlag Chemie, 1983.
3. Bensadoun A, Weinstein D. Assay of proteins in the presence of interfering materials. Anal Biochem 1976;70:241-50.
4. Dalton AJ. A chrom-osmium fixative for electron microscopy. Anatomical Record 1955;121:281.
5. Diakopoulos KN, Lesina M, Wormann S, et al. Impaired autophagy induces chronic atrophic pancreatitis in mice via sex- and nutrition-dependent processes. Gastroenterology 2015;148:626-638 e17.
6. **McWhorter FY, Wang T,** Nguyen P, et al. Modulation of macrophage phenotype by cell shape. Proc Natl Acad Sci U S A 2013;110:17253-8.
7. **Noll EM, Eisen C**, **Stenzinger A, Elisa Espinet**, et al. CYP3A5 mediates basal and acquired therapy resistance in different subtypes of pancreatic ductal adenocarcinoma. Nat Med 2016;22:278-87.
8. Schlitter AM, Jesinghaus M, Jager C, et al. pT but not pN stage of the 8th TNM classification significantly improves prognostication in pancreatic ductal adenocarcinoma. Eur J Cancer 2017;84:121-129.
9. **Muckenhuber A, Berger AK**, Schlitter AM, et al. **Christoph Springfeld, and Wilko Weichert**. Pancreatic Ductal Adenocarcinoma Subtyping Using the Biomarkers Hepatocyte Nuclear Factor-1A and Cytokeratin-81 Correlates with Outcome and Treatment Response. Clin Cancer Res 2018;24:351-359.
10. Stenzinger A, Endris V, Klauschen F, et al. High SIRT1 expression is a negative prognosticator in pancreatic ductal adenocarcinoma. BMC Cancer 2013;13:450.

Author names in bold designate shared co-first authorship

Supplementary Figure 1: Relating to Figure 1.

(A) GFP-LC3 and CK19 immunofluorescence of *A5;Kras* mice expressing transgenic *GFP-LC3*; white arrowhead indicates diffuse GFP-LC3 staining; nuclei are detected with DAPI. (B) Macroscopic and microscopic appearance of pancreata from 18-week old *Atg5* deficient (*A5;Kras*) and *Atg5* heterozygous mice (*A5+/-;Kras*) compared to 18-week old *Atg5* proficient mice (*Kras*); oncogenic Kras is expressed in all groups of mice. (C) Pancreas/Body weight ratio in 4-/9-/18/ and more than 18-week old *Kras*, *A5+/-;Kras*, and *A5;Kras* mice (n≥3). (D) Quantification of Acinar-to-Ductal Metaplasia (ADM) per High Power Field (HPF) in 4-week old *Kras*, *A5+/-;Kras*, *A5;Kras* mice (n≥4). (E) Quantification of PanIN-1/-2/-3 per High Power Field (HPF) in 9-/ 18-week old *Kras*, *A5+/-;Kras*, and *A5;Kras* mice (n≥3). (F) Kaplan-Meier survival curve of *Kras* (n=54), *A5+/-;Kras* (n=13), and *A5;Kras* (n=24) mice (Median survival 475, 451, 184 days respectively; ***P<0.0001 comparing *Kras* and *A5;Kras*). Mean±SD, *P<0.05, **P<0.01, ***P<0.001. Scale bars equal 50μm.

Supplementary Figure 2: Relating to Figure 2.

Colony formation assays in *Kras* and *A5+/-;Kras* cells after (A) 10% FCS cultivation, (B) 6-AA (6-Aminonicotinamide), (C) Rotenone, (D) Galactose/ Glutamine, and (E) high glucose treatment. Graphs are shown on the left, representative pictures on the right. Mean±SD (n=3).

Supplementary Figure 3: Relating to Figure 3.

(A) Representative macroscopic and microscopic pictures of pancreatic tumors from wildtype mice after orthotopic transplantation (TP) of *Kras* and *A5+/-;Kras* cells; primary tumors are shown on the top, tumors formed after transplantation in the fourth picture from the top, and CK19 immunohistochemistry on the bottom; Quantification of primary pancreatic tumor burden in mice after orthotopic transplantation of *Kras* and *A5;Kras* cell lines (% area of tumor tissue, n>3) (bottom). (B) Representative macroscopic and microscopic pictures of metastasis (lung, LN=lymph node, spleen) after TP of *A5+/-;Kras* cells into wildtype mice; white arrowheads indicate metastasis (top); metastasis incidence (%) after TP of *Kras* and *A5+/-;Kras* cells (n≥5) (bottom). (C) Representative macroscopic picture of wildtype mice after tail vein (i.v.) injection of *Kras* and *A5+/-;Kras* cells (left), and quantification of body weight in male and females (n≥3) (right). (D) H&E picture of liver and spleen metastasis after i.v. of *A5+/-;Kras* cells; asterisks indicate metastasis (top); representative bright field pictures of *Kras* and *A5+/-;Kras* cells isolated from the lung of wildtype mice after i.v.; asterisk and circle indicate two different cell populations (bottom). (E) Colony formation assay in *Kras*, *A5+/-;Kras*, and *Kras* cells after 58, 94% knockdown (KD) of *Atg5* (n>3) (left); representative pictures are shown (right); cells were cultivated in medium with 10% FCS. Mean±SD, **P*<0.05. Scale bars equal 50µm.

Supplementary Figure 4: Relating to Figure 4.

(A) Classification of significantly enriched gene sets into categories, based on Transcription Factor Binding Motif database for *Kras* (left) and *A5+/-;Kras* (right) cells; pie charts show classification and tables highlight examples of enriched pathways (NES≥1.0, $P<0.05$; *P* value 0.0 indicates $P<0.001$). (B) GSEA diagrams of significantly enriched KEGG pathways found in *Kras* (top) and *A5+/-;Kras* (bottom) cells. (C) Heat map of most highly regulated genes identified by GSEA in *Kras* and *A5+/-;Kras* cells.

Supplementary Figure 5: Relating to Figure 5.

(A) Analysis of phospho-AMPKa, AMPKa, phospho-S6, mitochondrial complexes (COX I, COX II/IV, ATP Core 2), SOD2, and BiP in protein lysates and *Xbp1* splicing (*Xbp1u*=unspliced, *Xbp1s*=spliced) in RNA-preparations from *Kras* and *A5+/-;Kras* cells; β-Actin and *cyclophilin* were used as loading controls. (B) Coupling efficiency (%) of mitochondria in *Kras* and *A5+/-;Kras* cells as measured by seahorse (n≥30). (C) qRT-PCR of *Sod1* and *Nrf2* in mRNA extracts from *Kras* and *A5+/-;Kras* cells; data are normalized to *cyclophilin* (n=3). Mean±SD.

Supplementary Figure 6: Relating to Figure 6.

(A) Proportions of *Kras* and *A5+/-;Kras* cells producing Ca2+ responses after stimulation with 0.01% or 0.05% FBS (n>170). (B) Cathepsin B (CTSB) extracellular activity (% extracellular activity versus total activity) as measured from supernatants of *Kras* and *A5+/-;Kras* cells (n=15). (C) Western blot analysis of Pro-cathepsin B (Pro-CTSB), Pro-cathepsin D (CTSD), and Pro-cathepsin L (Pro-CTSL) in supernatants of *Kras* and *A5+/-;Kras* cells. (D) Colony formation assay in *Kras* and *A5+/-;Kras* cells after cultivation with E64d. (E) Illustration of lysosome-associated DNA copy number gain (red) or loss (blue) (TCGA data) in normal pancreas versus pancreatic ductal adenocarcinoma (PDAC) samples (log2 copy number units). Mean±SD.

Supplementary Figure 7: Monoallelic loss of *Atg5* induces pro-tumorigenic inflammation.

(A) Cytokine profile expression shown by immunoblotting of protein lysates from *Kras* and *A5+/-;Kras* supernatants (left); quantification of average pixel intensity between two dots corresponding to the same cytokine; numbers above graph correspond to dot-position in plot (n=1). (B) Quantification of M1 and M2 macrophages (% of all macrophages) according to their morphology after stimulation with supernatants from *Kras* and *A5+/-;Kras* cells (n≥3); representative bright field pictures are shown indicating morphology of undifferentiated (asterisk), M1 (white arrowhead), and M2 (black arrowhead) macrophages (left); Arginase-1 immunofluorescence in macrophages after stimulation with supernatants from *Kras* and *A5+/-;Kras* cells; nuclei are detected with DAPI (right). (C) Representative immunohistochemistry pictures of F4/80 and CD206 in primary tumors from *Kras* and *A5+/-;Kras* mice (top); quantification of F4/80 and CD206-positive macrophages (% positive nuclei) in *Kras* and *A5+/-;Kras* primary tumors (n>3). (D) Immunohistochemical quantification of F4/80-positive cells per high power field (HPF) in the lungs of mice after i.v. with *Kras* and *A5+/-;Kras* cells (n=20) (left); representative F4/80 and Arginase 1 (Arg1) immunohistochemistry in tissue sections from the lungs of mice after tail vein injection (i.v.) with *Kras* and *A5+/-;Kras* cells; black arrowheads indicate F4/80-positive macrophages (right). (E) Quantification of lung metastasis (% area) after tail vein injection of *A5+/-;Kras* cells into PBS or clodronate-treated wildtype mice (n>3) (left); representative H&E pictures of the lung and F4/80 immunohistochemistry pictures of the spleen after the respective treatments. Mean±SD, **P*<0.05, ***P*<0.01, ****P*<0.001. Scale bars equal 50µm.

Supplementary Table 1: PDAC and Metastasis in *A5+/-;Kras* mice

List of *A5+/-;Kras* mice that were used for Pancreatic Adenocarcinoma (PDAC) and metastasis quantification; mouse number (ID), Gender, Age (days), PDAC incidence, Histology, liver/ lung/ diaphragm metastasis, ascites incidence, and other abnormalities are presented; Male=M, Female=F, Yes=Y, No=N, Ductal=D, Undifferentiated=U, lymph node infiltration=LN, Spleen infiltration=Spl, Kidney infiltration=Kd

ID	Gender	Age	PDAC	Histology	Liver	Lung	Diaphragm	Ascites	Others
7135	F	698	Y	D	N	N	N	N	
9138	F	293	Y	D	Y	N	N	N	LN
9137	F	340	Y	D	Y	Y	Y	Y	LN
9384	F	453	Y	D	Y	Y	Y	Y	Spl
2835	M	389	Y	U	N	N	N	N	
M5683	M	133	N	N	N	N	N	N	
M5681	M	346	Y	D	Y	Y	Y	Y	LN
M5617	F	385	Y	D	N	Y	N	N	
M5618	M	451	Y	D	N	Y	Y	N	
M5551	M	578	Y	D	Y	Y	N	Y	LN
P642	M	673	Y	D	Y	N	Y	Y	LN/Spl/Kd
M6215	F	451	N	N	N	N	N	N	

Supplementary Table 2: Human pancreatic cancer patient cohort (postoperative, Cohort 1).

List of the analyzed human pancreatic cancer samples for ATG5-western blot (n=67), collected from the MTBIO tissue bank of the Institute of Pathology at the Technical University Munich. Histology (Pancreatic Ductal Adenocarcinoma (PDAC)), extent of primary tumor (T), lymph node infiltration (N), metastasis (M), tumor differentiation grade (G), survival (months), ATG5 protein expression normalized to β-Actin and quantified by ImageJ (ATG5), and Tumor stage are shown. Samples marked with red or containing an X were not used in the analysis. The last 4 samples did not have patient data and were excluded from the study.

Histology	T	N	M	G	Survival	ATG5	Stage
PDAC	4	1	1	3	13	1.035	IV
PDAC	3	1	1	3	12	0.304	IV
PDAC	3	1	1	3	9	0.460	IV
PDAC	3	1	1	3	11	0.030	IV
PDAC	3	1	1	2	7	0.000	IV
PDAC	4	1	0	3	9	0.472	III
PDAC	4	1	0	3	12	0.144	III
PDAC	4	1	x	2	17	0.369	III
PDAC	4	1	x	2	5	0.294	III
PDAC	3	1	0	4	13	0.529	III
PDAC	3	1	0	3	26	0.624	IIB
PDAC	3	1	x	3	10	0.554	IIB
PDAC	3	1	x	3	29	0.685	IIB
PDAC	3	1	x	3	29	0.698	IIB
PDAC	3	1	0	3	7	0.873	IIB
PDAC	3	1	0	3	4	0.769	IIB
PDAC	3	1	0	3	5	0.016	IIB
PDAC	3	1	0	3	3	0.488	IIB
PDAC	3	1	0	3	lost to FU	0.621	IIB
PDAC	3	1	0	3	10	0.491	IIB
PDAC	3	1	0	3	4	0.526	IIB
PDAC	3	1	0	3	14	1.308	IIB
PDAC	3	1	0	3	9	0.966	IIB
PDAC	3	1	0	3	17	1.005	IIB
PDAC	3	1	0	3	11	0.428	IIB
PDAC	3	1	0	3	lost to FU	0.838	IIB
PDAC	3	1	0	3	lost to FU	0.042	IIB
PDAC	3	1	0	2	3	0.380	IIB
PDAC	3	1	0	2	29	0.382	IIB
PDAC	3	1	0	2	25	0.350	IIB
PDAC	3	1	0	2	34	0.649	IIB
PDAC	3	1	0	2	46	0.548	IIB
PDAC	3	1	0	2	31	0.758	IIB
PDAC	3	1	0	2	lost to FU	0.167	IIB

PDAC	3	1	0	2	10	0.115	IIB
PDAC	3	1	0	2	40	0.157	IIB
PDAC	3	1	0	2	3	0.964	IIB
PDAC	3	1	x	2	13	0.258	IIB
PDAC	3	1	x	2	10	0.255	IIB
PDAC	3	1	0	1	24	0.777	IIB
PDAC	3	1	0	1	56	0.210	IIB
PDAC	3	1	X		14	0.535	IIB
PDAC	2	1	0	1	23	0.101	IIB
PDAC	1	1	0	3	60	0.047	IIB
PDAC	3	0	0	3	4	0.805	IIA
PDAC	3	0	0	3	31	0.461	IIA
PDAC	3	0	x	3	18	0.486	IIA
PDAC	3	0	x	3	8	0.539	IIA
PDAC	3	0	0	3	76	2.504	IIA
PDAC	3	0	0	3	10	0.653	IIA
PDAC	3	0	0	3	lost to FU	0.502	IIA
PDAC	3	0	0	2	32	0.911	IIA
PDAC	3	0	x	2	21	0.303	IIA
PDAC	3	0	0	2	10	0.052	IIA
PDAC	3	0	x	2	39	0.388	IIA
PDAC	3	0	0	2	36	0.298	IIA
PDAC	3	0	0	2	30	1.674	IIA
PDAC	3	0	0	2	18	0.572	IIA
PDAC	3	0	0	2	lost to FU	0.405	IIA
PDAC	3	0	x	1	23	0.747	IIA
PDAC	3	0	x	1	34	0.181	IIA
PDAC	2	0	0	3	lost to FU	0.533	IB
PDAC	2	0	0	2	23	0.098	IB
PDAC						0.848	
PDAC						0.006	
PDAC						0.312	
PDAC						0.493	

Supplementary Table 3: Human pancreatic cancer patient cohort (palliative/ metastatic, Cohort 2).

List of the analyzed human pancreatic cancer samples for ATG5-immunohistochemistry (n=26). Each row represents one individual diagnosed with PDAC (Pancreatic Ductal Adenocarcinoma, as mentioned beneath the headline Histology) and exhibiting distant metastasis (M1, i.e., HEP=hepatic, PER=peritoneal, SKI=skin, ADR=adrenal). Patients were resected between 2008 and 2013 at the University Hospital Heidelberg. ATG5 protein was detected by immunohistochemistry; membranous ATG5 was scored according to the percentage and intensity of positive cells on a 0 to 3+ scale (negative as score 0, faint expression as score 1+, moderate expression as score 2+ and strong expression as score 3+). The sum score is provided in the second column. Patients without ATG5 score were excluded from the analysis.

Histology	ATG5	M1
PDAC	2.3	HEP, PER
PDAC	3	HEP
PDAC		HEP
PDAC	2.8	HEP
PDAC	1	HEP
PDAC		HEP, PER, ADR
PDAC		HEP
PDAC	2.9	HEP
PDAC		HEP
PDAC	2	PER
PDAC	2	PER
PDAC	2.8	PER
PDAC	3	HEP
PDAC	2.1	HEP
PDAC	1.8	HEP
PDAC	2.5	HEP
PDAC	2	SKI
PDAC	2.9	HEP
PDAC	1.9	HEP
PDAC		HEP
PDAC		HEP
PDAC	3	HEP
PDAC	2.1	HEP
PDAC		SKI
PDAC	3	HEP
PDAC	3	HEP

Supplementary Table 4: Human pancreatic cancer patient cohort (postoperative, Cohort 3).

List of the analyzed human pancreatic cancer samples for ATG5-immunohistochemistry (n=134). Each row represents one individual diagnosed with PDAC (Pancreatic Ductal Adenocarcinoma) at the Charité University Hospital Berlin. Event of death (yes=1, no=0), Survival (days), lymph node status (pN), metastasis status (pM), tumor stage (pT), patient characteristics (gender, age), UICC tumor staging, and resection margin (R) are shown. ATG5 protein was detected by immunohistochemistry; membranous ATG5 was scored according to the percentage and intensity of positive cells on a 0 to 3+ scale (negative as score 0, faint expression as score 1+, moderate expression as score 2+ and strong expression as score 3+). The sum score is provided in the first column. Patients without death event and no registered survival were removed from the analysis.

ATG5	Death	Survival	pN	pM	pT	Gender	Age	Stage	R
2.7	1	431	0	0	2	w	74	Stage I	0
2	1	898	1	0	2	w	75	Stage IIB	0
1	0		0	0	3	w	64	Stage IIA	0
2.7	0	5748	1	0	3	w	56	Stage IIB	1
3	1	278	1	0	3	m	47	Stage IIB	0
1	1	780	1	0	2	m	67	Stage IIB	0
3	1	407	1	0	3	w	62	Stage IIB	0
2.4	1	452	1	1	3	m	31	Stage IV	1
3	1	1166	1	0	2	w	63	Stage IIB	0
2.5	1	215	0	0	2	w	58	Stage I	0
3	1	629	1	0	2	m	53	Stage IIB	1
2.8	1	329	1	0	3	w	62	Stage IIB	0
2.8	1	46	0	0	2	w	61	Stage I	0
2.9	1	406	1	0	3	m	69	Stage IIB	0
2.1	1	236	0	0	2	w	70	Stage I	1
2.6	0	2459	0	0	2	w	71	Stage I	
2.6			1	0	2	m	64	Stage IIB	0
2.2	1	862	1	0	2	w	64	Stage IIB	0
2.3	1	448	1	0	2	m	71	Stage IIB	0
2.5	0	2302	1	0	2	m	64	Stage IIB	
3	1	287	1	0	3	w	47	Stage IIB	1
3	0	305	1	0	3	m	62	Stage IIB	
1.3	1	945	1	0	3	w	75	Stage IIB	0
2.2	1	832	1	0	3	w	62	Stage IIB	0
2.9	1	685	0	0	3	w	59	Stage IIA	
1.2			1	0	3	m	50	Stage IIB	0
2	1		1	0	2	m	60	Stage IIB	
1.3	0	2049	0	0	3	m	63	Stage IIA	0
2.2			1	0	3	m	66	Stage IIB	0
2.9	1	1045	1	0	3	w	49	Stage IIB	0
2.9	0	2104	0	0	2	w	64	Stage I	0
3	1	1743	1	0	2	m	71	Stage IIB	0
2.2			1	0	3	w	59	Stage IIB	0
1.2	0		0	0	3	m	59	Stage IIA	0

2.9	1	744	1	0	3	w	73	Stage IIB	1
3	1	740	1	0	3	m	50	Stage IIB	0
3	1	1258	0	0	3	w	62	Stage IIA	0
2.5	1	809	1	0	3	w	61	Stage IIB	0
3	1	167	1	0	3	m	66	Stage IIB	0
2	1	348	1	0	3	w	59	Stage IIB	1
2.2	1	911	1	0	3	m	64	Stage IIB	0
2.5	1	779	0	0	3	w	69	Stage IIA	0
2.9	1	471	0	0	2	w	76	Stage I	0
2.3	1	125	1	0	3	m	63	Stage IIB	0
2.2	0	1427	0	0	3	m	65	Stage IIA	1
3	1	395	0	0	3	m	60	Stage IIA	0
1.2	1		1	0	2	w	77	Stage IIB	
3	1		1	0	3	m	38	Stage IIB	
2	1		1	0	3	w	76	Stage IIB	1
3	0		1	0	3	m	63	Stage IIB	1
3			1	0	3	w	65	Stage IIB	0
2.6	1	432	0	0	2	w	69	Stage I	0
2.7	1	805	1	0	3	m		Stage IIB	
2.2	0	2644	0	0	3	w	62	Stage IIA	
3	1	496	1	0	3	w	79	Stage IIB	
2.8	1	198	1	0	3	m	49	Stage IIB	0
3	1		1	0	3	m	70	Stage IIB	
3	1	404	1	0	3	m	73	Stage IIB	
2.8	1		0	0	3	w	77	Stage IIA	
2	1	902	1	0	3	w	73	Stage IIB	
2.8	1	112	1	1	3	m	55	Stage IV	0
3	1	715	1	0	3	m	64	Stage IIB	0
3	1	209	1	0	3	w	51	Stage IIB	0
2.8	1	260	1	0	3	m	51	Stage IIB	0
3	1	353	1	0	3	w	67	Stage IIB	0
3	0		1	0	3	m	48	Stage IIB	
1.8	1	611	1	0	3	w	78	Stage IIB	0
2.9	1	98	1	0	3	w	63	Stage IIB	0
2.7	1	28	0	0	3	w	74	Stage IIA	1
2.7	0	2645	1	0	2	m	53	Stage IIB	0
2	0		0	0	2	w	59	Stage I	0
3	0	2609	1	0	3	m	69	Stage IIB	0
2.8	1		1	0	3	m	72	Stage IIB	0
2.8	1	255	1	0	3	m	74	Stage IIB	0
3	1		0	0	3	m	78	Stage IIA	0
2.9	1	184	0	0	4	w	72	Stage III	0
3	1	291	1	0	3	w	69	Stage IIB	0
3	0	1273	0	0	3	m	56	Stage IIA	0
3	1	1183	0	0	3	m	50	Stage IIA	0
2.6	1	96	1	0	3	w	75	Stage IIB	1
3	1		1	0	3	m	57	Stage IIB	0
0.7	1		1	0	4	w	70	Stage III	0
3	1	1064	1	0	3	m	72	Stage IIB	1
2	1	288	1	0	3	w	61	Stage IIB	0
2.8	1	192	1	0	4	m	57	Stage III	1
2.8	1	370	1	0	3	w	74	Stage IIB	0
2.9	1	1186	1	0	3	w	72	Stage IIB	0
3	1	394	0	0	3	m	69	Stage IIA	1

3	0	17	1	0	3	w	68	Stage IIB	1
1	1	369	0	0	3	w	79	Stage IIA	1
2.8			1	0	3	w	62	Stage IIB	1
2.8	0	7	1	0	3	m	60	Stage IIB	1
3	1	59	1	0	3	w	61	Stage IIB	1
3	1	289	1	0	4	m	60	Stage III	1
3			1	0	3	m	70	Stage IIB	0
2.2			0	0	1	m	66	Stage I	0
3	1	222	1	0	3	m	61	Stage IIB	1
2.05	0	415	0	0	3	w	81	Stage IIA	0
3	1	653	1	1	3	w	46	Stage IV	0
2	1	12	1	0	4	m	69	Stage III	1
3			1	0	3	m	59	Stage IIB	1
2.8	0	12	1	0	3	m	67	Stage IIB	0
2.8	1	205	1	0	3	m	69	Stage IIB	1
3			1	0	4	m	73	Stage III	0
2.5	1	615	1	0	3	m	54	Stage IIB	1
2.3	1	263	1	0	3	m	67	Stage IIB	1
2.7			0	0	3	m	65	Stage IIA	0
2	1	915	0	0	3	m	68	Stage IIA	0
3			1	0	3	m	75	Stage IIB	0
2	1	316	1	0	3	m	64	Stage IIB	0
3	1		1	0	2	m	73	Stage IIB	0
1.8	0	1079	1	0	3	w	59	Stage IIB	0
3	1	455	1	0	3	m	56	Stage IIB	0
2.7	0	210	1	0	3	m	43	Stage IIB	1
1.2	1	603	1	0	3	w	58	Stage IIB	1
2.8	0	865	1	0	3	w	57	Stage IIB	0
2.3			1	0	3	m	77	Stage IIB	1
3	0	311	1	0	3	m	61	Stage IIB	0
2.3	1	199	1	1	3	m	41	Stage IV	0
2.9	0	866	0	0	3	m	75	Stage IIA	0
2.2	1	582	1	0	3	m	75	Stage IIB	0
2.1			1	0	3	w	75	Stage IIB	1
2.3	1	265	1	0	4	m	74	Stage III	1
2	0	696	1	0	3	w	66	Stage IIB	0
2.2	1	185	1	0	3	m	51	Stage IIB	1
2.1	1	268	1	0	3	w	81	Stage IIB	0
2.9	0	586	0	0	3	m	69	Stage IIA	0
1.5	0	5	0	0	3	w	69	Stage IIA	0
2.2	1	1104	1	0	3	w	68	Stage IIB	0
2.6	1	324	1	0	3	w	68	Stage IIB	1
2.2	1	380	1	0	3	m	58	Stage IIB	0
2.3	1	249	1	0	3	w	63	Stage IIB	0
2.3	1	166	1	0	3	m	72	Stage IIB	0
2.8	1	216	1	0	3	m	55	Stage IIB	1

SUPPLEMENTARY MATERIALS AND METHODS:

Quantification of relative pancreatic weight, tumor incidence, and metastasis incidence

Kras, *A5+/-; Kras*, and *A5; Kras* mice were sacrificed at 4, 9, and 18 weeks of age or at the time point of sickness. Relative pancreatic weight was calculated from the pancreas and body weight obtained during sacrifice (pancreas weight/ body weight). Tumor incidence and metastasis incidence (% of tumor or metastasis-positive mice relative to all mice sacrificed) was calculated after histological examination. Metastasis-positive mice were mice with metastasis in liver, lung, or diaphragm from the pool of pancreatic tumor-positive mice. Ascites, lymph node, spleen, or kidney infiltration was also evaluated (see Supplementary Table 1).

Detection of GFP-LC3 puncta

GFP-LC3 mice with or without concomitant *Kras* expression were sacrificed after standard fed conditions. Pancreas was snap frozen in freezing medium (Tissue-Tek O.C.T. Compound, Weckert Labortechnik, Germany) and 7-10μm thick cryo-sections were mounted on adhesive-coated slides. Sections were air dried, fixed in 100% ethanol for 8 minutes at RT, washed with PBS and covered with DAPI containing mounting medium (H-1200 Vector Laboratories, CA). Sections were processed and kept in the dark until analysis. Puncta formation was detected by analysis of green fluorescence (EX/EM 470/525nm) with fluorescence microscopy (Zeiss Axiovert 200M).

Tumor cell isolation and cultivation

Primary pancreatic tumor cell lines were established from isolated murine pancreatic tumors. To establish the cell lines, pieces of pancreatic tumor tissue from *Kras*, *A5+/-; Kras*, and *A5; Kras* mice were placed in full culture medium (see below) and tumor cells were allowed to grow out of the tissue. Cell lines were routinely cultured under standard conditions (5% CO_2, 37 C) in culture media (Dulbecco's modified Eagle medium (DMEM) supplemented with 10%FBS (#10082147; Gibco), 1% PenStrep (#1500-063; Gibco), 1% Non-Essential-Amino-Acids (NEAA #11140050; Gibco)). On average, cells were passaged 5 times prior to any experiments.

Knockdown of mAtg5

Experimental procedures were followed as described previously [1]. Briefly:

Transfection of 293T cells for production of lentiviral particles

5 x 10^6 293T cells were seeded in 10 cm dishes. After one day, media was replaced and co-transfection of transfer plasmids purchased from Sigma Aldrich (TRCN0000327456 (54% knockdown, validated), TRCN0000327358 (58% knockdown, validated), TRCN0000363558 (81% knockdown, validated), TRCN0000375754 (86% knockdown, validated), and TRCN0000099432 (94% knockdown, validated)) with lentiviral packaging plasmids (pMD.GP, pRSV-rev, pMD.G) was performed using lipofectamine 2000 (Thermo Fisher Scientific). shRNA that does not target any known human or mouse gene (shNT) was used as a control. Two days later, lentiviral particles were harvested from the supernatant and frozen at -80°C.

Transduction of target cells with mATG5 knockdown constructs

Target *Kras* cells were seeded in 6 cm dishes. One day later, media was aspirated and 1 ml of lentiviral suspension was added to cells in presence of 8 µg/ml Polybrene (Sigma Aldrich). After 2 h at 37°C, 4 ml media was added. Selection of transduced cells was performed using 10 µg/ml puromycin.

Experimental analysis

Cells were tested in western blotting for Atg5, LC3, and β-Actin expression (as described below) and the knockdown percentage was confirmed. Cells with 54%, 58%, 81%, 86%, and 94% mAtg5-knockdown were further used in colony formation (full medium, 10% FCS), Boyden Chamber migration, invasion, and tail vein injection experiments as described below. Experiments were performed in triplicates.

In vitro *cathepsin activity measurements*

Activities of cathepsins B, L, and D were intra- and extracellularly assessed in cell lysates and culture media of primary pancreatic tumor cell lines. Tumor cells were separated from culture media by centrifugation at 1000 g for 10 min. Then, cell pellet and culture medium were snap frozen. After thawing tumor cells were subsequently resuspended in ice-cold homogenization buffer (5 mM MOPS pH 6.5, 250 mM sucrose, 1 mM Mg_2SO_4, 0.13% Triton X100l) and lysed by sonication. Cathepsin B and -L were determined as Ca074- and N1760-sensitive activity in assay buffer (50 mM sodium phosphate buffer [pH 5.5], 1 mM EDTA, and 1 mM dithiothreitol) using the fluorogenic substrates Z-Arg-Arg-7-amino-4-methylcoumarin A (10µM, #31213-v, Pepta Nova) and Z-Phe-Arg-7-amino-4-methylcoumarin (10µM, #3095-v, Pepta Nova), respectively. Cathepsin D activity was measured in 50 mM sodium acetate buffer pH 4.0 using the fluorogenic substrate Mca-Gly-Lys-Pro-Ile-Leu-Phe-Phe-Arg-Leu-Lys(Dnp)-D-Arg-NH2 (10µM, #3200-v, Pepta Nova). The release of 7-amido-4-methylcoumarin was kinetically monitored over 10 minutes at the excitation/emission

wavelength of 360/438 nm in a Safire microplate reader (Tecan, Grödig, Austria) by spectrofluorometry. Intra- and extracellular portions of cathepsin activities were normalized to the protein concentration in cell lysates determined by BioRad protein Assay kit.

Subcellular fractionation by isopycnic Percoll density centrifugation and measurement of GLDH activity

To analyze distribution and integrity of mitochondria in subcellular fractions pelleted tumor cells harvested from primary pancreatic tumor cells lines (produced as described above) were resuspended in HS buffer (250mM sucrose, 10 mM citric acid, 0.5 mM EGTA, 0.1 mM MgSO4 [pH 6.0]) and homogenized by 5 strokes using a Dounce homogenizer. After centrifugation at 100g post-nuclear supernatant was applied onto an isotonic 50% (v/v) Percoll/HS buffer solution (described above) at pH 7.27 and subsequently separated by isopycnic centrifugation at 50,000 g for 45 min at 4°C. After separation the percoll gradient was portioned in 46 fractions using a peristaltic pump beginning from the bottom and fractions were stored at -80°C until further use.

Activity of GLDH as a marker of mitochondrial distribution in subcellular fractions was determined spectrophotometrically at 340 nm according to $NADH_2$ oxidation with 2-oxoglutarate and NH_4^+ as a substrate by the method of E. Schmidt [2].

Immunoblotting

For immunoblotting, *Kras*, *A5+/-; Kras*, and *A5; Kras* cells were pelleted and snap frozen. Cell pellets were resuspended in ice cold protein lysis buffer (50mM HEPES pH 7.9, 150mM NaCl, 1mM EDTA pH 8.0, 0.5% NP-40 (Roche), 10% Glycerol) supplemented with protease/phosphatase inhibitors (SERVA), sonicated, and kept on ice. Extracellular proteins secreted into the culture medium were concentrated by trichloroacetic acid precipitation (TCA, final concentration 6 %) in the presence of 2% Na-deoxycholate by the method A. Bensadoun[3]. Concentration was determined by BioRad protein Assay kit and concentration of all samples was set to 4 □g/□l. All samples were cooked for 5min at 95°C in Laemmli buffer (300 mM Tris-HCl, pH 6.8, 10% (w/v) SDS, 50% (v/v) Glycerol, 0.05% (w/v) Bromphenole blue, 5% (v/v) β-mercaptoethanol) except when used for detection of mitochondrial oxidative phosphorylation complexes. Protein lysates were separated by SDS-gel electrophoresis and transferred to PVDF membranes. Following over night incubation with primary antibody at 4°C, proteins were detected using horseradish peroxidase-conjugated secondary antibodies anti-mouse (NA931V GE Healthcare Life Sciences), anti-rabbit (NA934V GE Healthcare Life Sciences) or anti-guinea pig (A7289 Sigma) and ECL reagent (Amersham). The primary antibodies used include: Anti-Atg5 (1/1000) (NB110-53818 Novus Biologicals), anti-p62 (1/1000) (GP62-C Progen), anti-LC3 (1/1000) (PD014

MBL International), anti-Cathepsin B (1/5000) (AF965, R&D Systems), anti-p53 (1/500) (NCL-p53-CM5p Novocastra), anti-Cathepsin L (1/5000) (AF1515, R&D Systems) anti-Cathepsin D (1/5000) (cs-10725, Santa Cruz Biotechnology), anti-phospho-AMPKa (1/1000) (2535 Cell Signaling Technology), anti-AMPKa (1/1000) (2532 Cell Signaling Technology), anti-phospho-S6 (1/1000) (2211 Cell Signaling Technology, anti-SOD2 (1/1000) (ADI-SOD-111 Enzo), anti-BiP (1/1000) (AB21685 Abcam), anti-MitoProfile Total OXPHOS Rodent Western Blot antibody cocktail (1/1000) (MS604 Mitosciences), □nti-β-Actin (1: 2000) (A5441, Sigma).

Histochemistry and immunohistochemistry

For proliferation analysis mice were labeled with 50μg of BrdU (B5002 Sigma) per g body weight by intraperitoneal injection and sacrificed 2h later. Pancreas was fixed in 4% (wt/vol) paraformaldehyde in PBS overnight at 4°C and embedded in paraffin wax. Tissue sections of 2μm thickness were mounted on adhesive-coated slides and stained with H&E.

For immunohistochemistry standard procedures were applied. Briefly, after deparaffinization and rehydration, heat-induced antigen retrieval with 0,01M citrate pH 6.0 was utilized. Endogenous peroxidase was blocked with 3% hydrogen peroxide for 15min at RT in the dark. Unspecific binding was blocked with 5% serum for 1h at RT. Slides were incubated with primary antibodies diluted in blocking solution over night at 4°C. Primary antibodies used include: anti-BrdU (1/250) (MCA2060 AbD Serotec), anti-F4/80 (1/100) (MF-48000 Invitrogen), anti-CK19 (1/200) (TROMA III Developmental Studies Hybridoma Bank), anti-Arginase 1 (1/500) (610708 BD Transduction Laboratories), anti-S100a4 (1/800) (13018 Cell Signaling Technology), anti-MMR/ CD206 (1/100) (AF2535 R&D systems Biotechne), anti-Atg5 (1/100) (NB110-53818 Novus Biologicals), anti-p62 (1/100) (GP62-C Progen), and anti-LC3 (1/100) (PD014 MBL International). Secondary antibodies including biotinylated anti-rabbit in goat (BA 1000 Vector), anti-mouse in goat (BA 9200 Vector), and anti-rat in rabbit (BA 4000 Vector) were applied for 1h at RT and avidin-biotin peroxidase complex for biotinylated secondary antibodies was then added according to manufacturer directions (Vector Laboratories, CA). Staining was developed with DAB reagent (Vector Laboratories, CA). For Arginase 1 and S100a4 detection Streptavidin/Biotin blocking kit (SP2002 Vector) was used during the staining procedure to reduce background, according to manufacturer instructions. Hematoxylin was used for counterstaining.

ADM and PanIN Quantifications

Paraffin-embedded tissue sections from 4-week old *Kras*, *A5+/-; Kras*, *A5; Kras* were stained for H&E and photographed at 100x magnification. The number of Acinar to Ductal Metaplasias was determined in each picture using Zeiss axiovision software. Measurements

from multiple photographs per tissue slide were summed up and expressed as ADM per High Power Field (HPF). Results were then averaged according to genotype. In a similar fashion, paraffin-embedded tissue sections from 9- and 18-week old *Kras*, *A5+/-; Kras*, *A5; Kras* were stained for H&E and photographed at 100x magnification. Pancreatic Intraepithelial Neoplasias (PanINs) were classified according to PanIN-1/-2/-3 and total numbers were expressed as PanIN/HPF. Results were then averaged according to genotype and age group.

Co-immunofluorescence

Cryo-sections of GFP-LC3 transgenic pancreas were processed as described above. Unspecific binding was blocked with 5% serum at RT and incubated over night at 4°C with the primary antibody. Anti-CK19 primary antibody (TROMA III Developmental Studies Hybridoma Bank) was diluted in blocking solution (1/200). At the following day secondary antibody anti-rat in goat Alexa Fluor 568 (1/300) (A11077 Invitrogen) was applied for 1h at RT. In the end, slides were covered with DAPI containing mounting medium (H-1200 Vector Laboratories) and analyzed with fluorescence microscopy (Zeiss Axiovert 200M).

Transmission Electron Microscopy (TEM)

For TEM *Kras* and *A5+/-; Kras* cells were collected and fixed in 2.5% electron microscopy grade glutaraldehyde in 0.1M sodium cacodylate buffer pH 7.4 (Science Services, Munich, Germany), postfixed in 2% aqueous osmium tetraoxide [4], dehydrated in gradual ethanol (30–100%) and propylene oxide, embedded in Epon (Merck, Darmstadt, Germany) and cured for 24 hours at 60°C. Pellets were cut in semithin sections and stained with toluidine blue. Ultrathin sections of 50nm were collected onto 200 mesh copper grids, stained with uranyl acetate and lead citrate before examination by transmission electron microscopy (Zeiss Libra 120 Plus, Carl Zeiss NTS GmbH, Oberkochen, Germany). Pictures were acquired using a Slow Scan CCD-camera and iTEM software (Olympus Soft Imaging Solutions, Münster, Germany)

RNA Extraction and Quantitative Real-Time Polymerase chain reaction (qRT-PCR)

For RNA extraction, *Kras* and *A5+/-; Kras* cells were collected in RLT lysis buffer (1015762 Qiagen) supplemented with 1% β-mercaptoethanol (M6250 Sigma) and snap frozen. Subsequently, RNA was extracted using the RNeasy Mini Kit (74104 Qiagen). SuperScript II Reverse Transcriptase (18064-014 Invitrogen) was used for complementary DNA (cDNA) synthesis. qRT-PCR was carried out using a StepOne Plus Real-Time PCR System (Applied Biosystems) in combination with Power SYBR Green PCR Master Mix (4368577 Applied

Biosystems). Target mRNA expression was normalized to endogenous *cyclophillin* and quantified by the delta-delta CT method. Primer sequences are provided below.
For detection of spliced *Xbp1*, cDNA was subjected to PCR with a primer set detecting both unspliced and spliced *Xbp1* (unspliced *Xbp1u* 171 bp, spliced *Xbp1s* 145 bp). PCR products were separated by agarose gel electrophoresis. *Cyclophilin* was used as control.

Gene	Forward primer	Reverse primer
Sod1	GTCCGTCGGCTTCTCGTCT	CACAACTGGTTCACCGCTTG
Sod2	ACACATTAACGCGCAGATCA	ATATGTCCCCCACCATTGAA
Nrf1	TCTCACCCTCCAAACCCAAC	CCCGACCTGTGGAATACTTG
Nrf2	TTCTTTCAGCAGCATCCTCTCCAC	ACAGCCTTCAATAGTCCCGTCCAG
Xbp1	ACACGCTTGGGAATGGACAC	CCATGGGAAGATGTTCTGGG
Cyclophilin	ATGGTCAACCCCACCGTGT	TTCTGCTGTCTTTGGAACTTTGTC

Microarray Data Analysis

For transcriptomic analysis, *Kras* and *A5+/-; Kras* tumor cells were harvested after PBS-washing in RLT lysis buffer supplemented with 1% β-mercaptoethanol, as described above. Cell suspensions were snap frozen and stored at -80°C. RNA isolation from tumor cell suspensions and Affymetrix GeneChip (*Mus musculus*) Mouse Gene 1.0 ST Array was conducted by the service facility KFB Center of Excellence for Fluorescent Bioanalytics (Regensburg, Germany, www.kfb-regensburg.de). Microarray data were analyzed by using the Gene Set Enrichment Analysis Software (GSEA) provided by the Broad Institute. A Nominal Enrichment Score (NES) of ≥1.0 and a nominal p-value of <0.05 were used to evaluate significantly upregulated pathways according to KEGG and Transcription Factor Binding Motif databases. Pathways were subsequently separated into groups depending on their description in the respective database. A heat map of the most highly regulated genes computed by GSEA was used and the genes were further classified according to their function. Genes belonging to one functional group were depicted as percentage related to the entire number of highly regulated genes. A NES versus nominal p value diagram was provided to indicate the total number of regulated (NES≥0.5) and significantly regulated (NES≥1.4, nominal p value< 0.05) pathways detected in the KEGG database. Microarray data are available in the ArrayExpress database at EMBL-EBI (https://www.ebi.ac.uk/arrayexpress/) under accession number E-MTAB-6275.

Non-targeted metabolomic measurements

LC-MS/MS–based non-targeted metabolomics analysis was conducted at the Genome Analysis Centre, Helmholtz Zentrum München as previously described [5]. About $1x10^6$

pancreatic cancer cells were required for the analysis. In brief, 0.375x10^6 *Kras* or *A5+/-; Kras* cells were seeded in duplicates in a 6-well plate with 2 ml culture medium and grown for 48h until 80-90% confluent and an approximate number of 0.5x10^6 was reached. Cells were washed two times with PBS (37°C). Dry ice cold 80% v/v methanol (400 µl) containing 4 recovery standard compounds to monitor extraction efficiency was added to the cells to cover them immediately. Cells were scraped and the cell suspension was transferred into precooled (dry ice) 2 ml screw cap micro tubes (Sarstedt Micro tube 2 ml, PP (Reference #: 72.694.005)) filled with 160 mg glass beads. Another 100 µl of dry ice cold methanol extraction solvent to wash the well was added and transferred to the micro tube. Suspensions of two 6-wells were pooled into one tube to obtain a sample of 1x10^6 cells in 1 ml cell suspension. The samples were stored immediately at -80°C until metabolomic analysis was performed. The metabolites were assigned to cellular pathways based on PubChem, KEGG, and the Human Metabolome Database. Metabolic pathways were described as significantly up- or down-regulated, when metabolites assigned to those specific pathways were increased or decreased, respectively. Values depicted correspond to the absolute values normalized in terms of raw area counts after LC/MS-based metabolomic analysis.

Oncomine database

The oncomine database (www.oncomine.org) was used to search for autophagy and lysosomal function-associated genes. GO Biological Process-Autophagy or GO Cellular Component-Lysosome was used as concept; primary filters selected were Cancer versus Normal Analysis and Pancreatic Cancer; pathology subtypes M1+, N1+, T4 according to TNM-staging were subsequently applied. DNA Copy Number (log2 copy number units) retrieved from the Cancer Genome Atlas (TCGA Research Network, http://cancergenome.nih.gov/) was used to illustrate copy number gain or loss in human pancreatic cancer samples versus normal pancreas samples.

Measurement of mitochondrial metabolism by seahorse analyzer

Measurements of oxygen consumption rate (OCR) were performed with a XF extracellular flux analyzer as described previously (Oelkrug R, Goetze N, Exner C, Lee Y, Ganjam GK, Kutschke M, Muller S, Stohr S, Tschop MH, Crichton PG, Heldmaier G, Jastroch M, Meyer CW. Brown fat in a protoendothermic mammal fuels eutherian evolution. Nature communications 2013;4:2140). Briefly, *Kras* and *A5+/-;Kras* tumor cells were seeded at a density of 1X10^5 cells per well in a XF24 cell culture microplate. DMEM (4.5 g/L glucose, +L-Glutamine, -Pyruvate, pH 7.6 at RT) supplemented with 10% heat inactivated FBS (Gibco)

and 1% Pen/Strep was used for cell culturing. On the day of assay (24h after seeding), medium was exchanged to non-carbonated Seahorse measurement medium and the XF24 plate was transferred to a temperature-controlled (37 °C) XF24 Extracellular Flux analyzer (Seahorse Bioscience) and equilibrated for 10 min. To determine the basal respiration four assay cycles (1-min mix, 2-min wait and 3-min measuring period) were used. Then oligomycin (4 μ M) was added by automatic pneumatic injection (three assay cycles) to inhibit ATP synthase and thus approximate the proportion of respiration used to drive ATP synthesis versus proton leak-linked respiration. Oligomycin was followed by an injection of FCCP (carbonyl cyanide p-trifluoromethoxyphenylhydrazone) (0.5 μ M) to completely dissipate proton motive force and maximally stimulate mitochondrial respiration (three assay cycles), thus determining spare respiratory capacity and substrate oxidation capacity. An injection of rotenone (4 μ M) and antimycin A (2 μ M) was used to correct for the non-mitochondrial respiration rate (three assay cycles), which was subtracted from all the other rates. Coupling efficiency was calculated as the oligomycin-sensitive fraction of mitochondrial respiratory activity, estimating the proportion of basal respiration used to drive ATP synthesis. To determine extracellular acidification rates (ECARs) for glycolysis, experiments were ended by injection of 2-DG (2-deoxy-D-glucose, 100 mM), correcting for non-glycolytic acidification. Injection of 2-DG enabled calculation of glycolytic acidification. Data obtained after oligomycin treatment induce glycolytic capacity. OCR was plotted against ECAR to illustrate oxidative versus glycolytic metabolism in cancer cells. Raw data were normalized to either protein or DNA content (ng).

Cell morphology analysis and quantification of cell proliferation

To analyze cell morphology, *Kras* and *A5+/-; Kras* were seeded in 6-well plates. 24h after seeding, pictures were acquired with the Zeiss Axiovision Imager A1 using a magnification of 100x. For quantification of proliferation, $5x10^4$ *Kras* and *A5+/-; Kras* cells were seeded per well in a 6-well plate. The culture media was changed every other day. Cells were counted after trypsinization every 24 hours up to 120 hours using the neubauer counting chamber. Full medium Dulbecco's modified Eagle medium (DMEM) supplemented with 10%FBS (#10082147; Gibco), 1% PenStrep (#1500-063; Gibco), 1%NEAA (#11140050; Gibco) was used for cell culture.

Autophagic flux measurement using Cyto-ID

To analyze autophagosome accumulation, *Kras* and *A5+/-; Kras* were seeded in triplicates in 96-well plates and allowed to adhere overnight. Half of the cells were kept in full medium and compared to cells cultivated overnight in serum-free medium. Autophagosome accumulation was analyzed by using the CYTO-ID Autophagy Detection Kit (Enzo, ENZ-51031) according

to the manufacturer's instructions. Fluorescence was detected using a Varioscan Lux (Thermo scientific) microplate reader.

Colony formation and cell treatments

For the cologenic assay, $3x10^2$ *Kras* and *A5+/-; Kras* cells were plated in triplicates six-well plates and grown for 10d in culture media. Colonies were stained with 2% crystal violet (C3886; Sigma), washed with water, and their area was quantified using ImageJ. Treatments during the clonogenic assays include: 10% FCS-containing medium, serum-free HBSS-containing medium (Hanks´Balanced Salt Solution GIBCO-14025092, 1:20 dilution of normal medium), chloroquine in full medium (2μM and 6 μM, C6628 SIGMA), 6-Aminonicotinamide in full medium (10μM and SIGMA-A68203), Rotenone in full medium (15nM and SIGMA-R8875), Galactose and Glutamine in glucose free medium (Galactose 10mM and Glutamine 4mM, D-(+)-Galactose, SIGMA-G5388 and GlutaMAX-I, GIBCO-35050061, DMEM, no glucose, GIBCO-11966-025), High Glucose in glucose free medium (25mM and GIBCO-A2494001).

Anoikis assay

For the anoikis assay, 6-well plates were coated with poly-HEMA (20mg/ml) (P3932; Sigma) dissolved in 96% ethanol. $5x10^5$ *Kras* and *A5+/-; Kras* cells were seeded in triplicates and cultured for 48h in culture media. Surviving cells in the media were calculated using the neubauer counting chamber.

Boyden Chamber Migration Assay

$1.5x10^5$ *Kras* and *A5+/-; Kras* cells were seeded in triplicates in 6-well plates till confluence. 100 μL serum free medium was added to upper chamber and 200 μL cells were added to chamber ($2.5x10^5$/mL in serum free medium). 750 μL full medium was added to lower chamber. Boyden-Chamber Assay plate was incubated at 37ºC for 12-16 hours. After incubation, medium was removed from upper chamber and chambers were washed twice with PBS. Cells were fixed with formaldehyde (3.7% in PBS) for 2 minutes and washed with PBS twice. To permeabilize cells, 100% methanol was added to chambers for 20 minutes. After removing methanol chambers were washed twice with PBS. Chambers were place into wells and stained with Giemsa at room temperature for 15 minutes. After removing Giemsa solution, chambers were washed twice with PBS. Non-migrated cells were scraped off with cotton swabs from the membranes. Migrated cells were counted under a light microscope.

Invasion assay

6.5mm Transwell (#CLS3464; Sigma, Corning Costar, USA) with 8.0 μm Pore polyester

membrane insert was used in 24-well culture plates. The upper surface of the membrane was coated with 100µl mixed matrigel (corning Life Sciences) per well. The matrigel was incubated at 37°C for gelling. 5x10^4 *Kras* and *A5+/-; Kras* cells were seeded in triplicates with 200µl serum-free DMEM in the upper chamber. The lower chamber was filled with 750 µl of culture media. After 48h, the cells were fixed by formaldehyde 3.7% in PBS, permeabilized with 100% methanol and stained with crystal violet. Cells that invaded to the lower surface area of the membrane were calculated by counting stained cells. E64d (100 µM and E3132-SIGMA) was used to inhibit cathepsin activity. Filopodia were quantified after 36h of seeding.

Orthotopic Transplantation

Littermates of *A5+/-; Kras* mice 8 weeks of age were injected orthotopically into the pancreas with 1×10^6 of either *Kras* or *A5+/-; Kras* tumor cell suspensions (resuspended in a solution of Matrigel (Corning 354234)/ DMEM without supplements in a ratio of 4/1) using a 26G needle. The mice were sacrificed 30 d after injection, or earlier when they reached sickness criteria. Pancreatic tissues were collected, embedded in paraffin and stained with haematoxylin and eosin (H&E). Lung, liver, lymph nodes, kidney, spleen, and duodenum were also collected and processed in the same way. Occurrence of tumors and metastasis was quantified and representative macroscopic and microscopic pictures were taken.

Tail vein injection

Littermates of *A5+/-; Kras* mice 8 weeks of age were injected intravenously through the tail vein with 1×10^6 of either *Kras* or *A5+/-; Kras* tumor cell suspensions (resuspended in 0,9% saline solution) using a 26G needle. The mice were sacrificed 20 d after injection, or earlier when they reached sickness criteria. The lungs were collected, embedded in paraffin and stained with haematoxylin and eosin (H&E). Mice were classified as metastasis positive or negative and representative macroscopic and microscopic pictures were taken. Body weight at time of sacrifice was measured to establish levels of cachexia. Metastatic tumor cells were re-isolated from pieces of lung tissue to determine cell morphology and survival capacity.

Liposomal clodronate treatment

For macrophage depletion in wildtype mice, clodronate-loaded liposomes (CP-010-010, Liposoma) were used. As control, mice were injected with control liposomes (PBS). For the experiment, mice were injected intraperitoneally (ml/ mouse) as follows:

Prior to tail vein injection	After tail vein injection

Day -8	Day -4	Day 0	Day 4/ 8	Day 12/16	Day 20
0.2 ml	0.2 ml	0.1 ml	0.1 ml	0.1 ml	0.1 ml

Clodronate and PBS treated mice were injected with *A5+/-;Kras* cells (biological duplicates) into the tail vein (at Day 0 according to the scheme above) to analyze the influence of macrophages on metastasis in the lung. Experiments were performed with at least 5 mice per group. Mice were sacrificed 21 days after tail vein injection due to sickness. Spleens of mice were analyzed after the experiments for F4/80 immunohistochemistry as described above. Lung metastasis was quantified as described below.

Cytokine array

In order to detect cellular cytokine profile supernatants of *Kras* and *A5+/-; Kras* cells were collected and processed as described above for immunoblotting. Lysates were then used according to the manufacturer's instructions (Mouse Cytokine Array Panel A, Catalog Number ARY006, R&D Systems). Pixel intensity of individual plots was quantified using ImageJ software. The average of two spots corresponding to one cytokine was used to compare cytokine profile according to genotype.

Macrophage differentiation assay

To detect the effect of *Kras* and *A5+/-; Kras* cells on macrophage phenotype, *Kras* and *A5+/-;Kras* cells were seeded in 6-well plates and cultivated for 48h. Supernatants were collected and applied on Raw macrophages (RAW 264.7 (ATCC® TIB-71™) cultivated in Dulbecco's modified Eagle medium (DMEM) supplemented with 10%FBS (#10082147; Gibco), 1% PenStrep (#1500-063; Gibco), 1%NEAA (#11140050; Gibco). Macrophage phenotype was monitored and assessed by microscopy as described [6].

For Arginase-1 Immunofluorescence macrophages were treated as described above and subsequently stained with anti-Arginase 1 (1/500) (610708 BD Transduction Laboratories). Briefly, unspecific binding was blocked with 5% serum at RT and cells were incubated over night at 4°C with the primary antibody. At the following day secondary antibody anti-mouse in goat Alexa Fluor 488 (1/300) (A-11001 Invitrogen) was applied for 1h at RT. In the end, slides were covered with DAPI containing mounting medium (H-1200 Vector Laboratories) and analyzed with fluorescence microscopy (Zeiss Axiovert 200M).

Measurement of Ca2+ responses

To measure Ca2+ responses, *Kras* and *A5+/-;Kras* cells were loaded with Fluo-4 by incubation with Fluo-4/AM (5μM) for 60min at room temperature (approximately 23°C) in Na-Hepes-based solution (140mM NaCl, 4.7mM KCl, 1.13mM $MgCl_2$, 10mM HEPES, 10mM

Glucose, 1.8mM $CaCl_2$, pH7.4). After that cells were washed by perfusion (gravity-based perfusion system) with the Na-Hepes-based solution and imaged every 2sec over a time period of 800sec using a Zeiss 510 confocal made (excitation 488nm, emission LP505). Heat Inactivated FBS (0.01% or 0.05% diluted in the Na-Hepes-based solution) was applied when 200sec of recording were reached.

Fluorescent responses (F) were normalized to fluorescence F_0 recorded before the addition of FBS (average fluorescence value for measurements recorded during 190 - 200sec time interval). Amplitude of cytosolic Ca2+ responses was determined by the equation $((F_{max}-F_0)/F_0=\Delta F_{max}/F_0$, with F_{max} corresponding to the maximum Fluo-4 fluorescence measured during the 200-500sec interval. Amplitude of cytosolic Ca2+ responses of each single cell over 5min of FBS application was measured and the amplitudes were then averaged for each genotype (n > 170 cells for each genotype).

Cells responding to FBS were defined as cells exciding 20% elevation threshold of normalized fluorescence (F/F_0) in the first 5min of FBS application.

Quantification of primary tumor and metastasis burden (iv and orthotopic TP; also with liposomal clodronate treatments)

For quantification of primary tumor and metastasis burden (in all orthotopic transplantation and tail vein injection experiments) 2 μm-tissue slices were stained with H&E. Per H&E slide multiple pictures at 100x magnification were taken. Area (μm^2) of tumor foci in pancreas and/ or lung tissues was calculated and expressed as % to all tissue area using a proprietary software package (Zeiss Axiovision, Oberkochen, Germany). Statistical analysis was done in between the genotypes (mean ± standard deviation (SD), Student t test).

Quantification of F4/80-positive and CD206-positive macrophages

For quantification of F4/80-positive macrophages in the lungs of tail vein-injected mice, tissue sections were stained for F4/80 via immunohistochemistry, as described above. Sections were subsequently photographed at 200x magnification. Number of positive cells was determined with Zeiss axiovision software. Sum from multiple photographs per tissue slide were generated and expressed in relation to the number of high power fields counted. Results were then averaged by genotype.

F4/80-positive and CD206-positive macrophages were also quantified in the original tumors of *Kras* and *A5+/-;Kras* mice. For this, tissue slides were stained with the respective antibodies and the % of positive nuclei/ all nuclei were determined.

Human sample analysis

For ATG5 immunoblotting, a total of 67 human PDAC samples (Supplementary Table 2, Cohort 1) collected from the MTBIO tissue bank of the Institute of Pathology at the Technical University Munich, were analyzed as described above. Band density was quantified by using ImageJ and normalized to β-Actin. From these 67 patients, n=56 with known survival were grouped into ATG5 low-moderate expression (ATG5/ β-Actin ratio below 0,5) and high expression (ATG5/ β-Actin ratio equal/ above 0,5) and used for Kaplan-Meier survival analysis with GraphPad Prism.

For ATG5 immunohistochemistry, two different cohorts (Cohort 2 and Cohort 3) were used. Cohort 2 consisted of 26 primary PDACs and their corresponding distant metastases that were resected between 2008 and 2013 at the University Hospital Heidelberg (Supplementary Table 3). The use of this tumor cohort for biomarker analysis has been approved by the ethics commission of the Klinikum rechts der Isar, Technische Universität München (403/17S). Primary tumor samples were used for ATG5 immunohistochemistry as described below for Cohort 3 and 19 of these were evaluated as described below for Cohort 3. In this analysis 4 patients from the Cohort 3 also exhibiting distant metastasis were included as well. The percentages of patients with distant metastasis in the low-moderate and in the high ATG5-expressing groups were calculated as described below for Cohort 3.

Cohort 3 consisted of a patient cohort with primary resected PDACs. The cohort was investigated previously in several studies [7-9] and included 200 individuals (Supplementary Table 4) that received partial pancreatoduodenectomy for PDAC between 1991 and 2006 at the Charité University Hospital Berlin. The use of this tumor cohort for biomarker analysis has been approved by the Charité University ethics committee (EA1/06/2004).

Tissue microarrays of both IHC cohorts were generated as previously described [7, 10]. In detail three tumor cores (diameter 1.5 mm) of representative tumor areas selected by a board certified pathologist on H&E stained slides were punched out of formalin-fixed paraffin embedded (FFPE) tissue blocks and arranged in a newly generated paraffin block. TMAs were made using a tissue microarrayer (Beecher Instruments, Sun Praierie, USA). Staging of both cohorts followed the WHO recommendations at the time of cohort generation (TNM-classification of the 7th edition). Clinical and demographic information was obtained from the respective institutional patient databases, by reviewing medical charts and pathological reports. Patient follow-up data were obtained from clinical records and via direct contact with patients and/ or their relatives. For Immunohistochemistry, 2µm sections prepared with a rotary microtome (HM355S, ThermoFisher Scientific, Waltham, USA) were collected from 134 patients in this cohort (Supplementary Table 3). Immunohistochemistry was performed using a Bond RXm system (Leica, Wetzlar, Germany, all reagents from Leica) with a primary antibody against ATG5 (NB110-53818 Novus Biologicals). Briefly, slides were deparaffinized using deparaffinization solution, pretreated with Epitope retrieval solution 1 (corresponding to

citrate buffer pH 6) for 20 minutes. Antibody binding was detected with a polymer refine detection kit without post primary reagent and visualized with DAB as a dark brown precipitate. Counterstaining was done with hematoxyline. The membranous ATG5 was scored according to the percentage and intensity of positive cells on a 0 to 3+ scale (negative as score 0, faint expression as score 1+, moderate expression as score 2+ and strong expression as score 3+; see Figure 7B for a panel of staining). Kaplan-Meier survival analysis was performed by GraphPad Prism with a total of 79 patients from the 134. Patients with no available survival and patients with no death follow up were removed from the analysis. The two groups in the Kaplan-Meier analysis included low-moderate ATG5-expressing patients (with scores 1 and 2) and high ATG5-expressing patients (score 3). Lymph node status and resection status in these patients was expressed as % patients referring to the total patients belonging to the two groups.

An overview of the three different cohorts used can be found in the following table:

Cohort number	**Status**	**Site**	**Analysis**	**Number of patients**
1	Postoperative	Primary	Western blot	56
2	Palliative/ metastatic	Primary	IHC	23
3	Postoperative	Primary	IHC	79

SUPPLEMENTARY REFERENCES:

1. Cui H, Seubert B, Stahl E, et al. Tissue inhibitor of metalloproteinases-1 induces a pro-tumourigenic increase of miR-210 in lung adenocarcinoma cells and their exosomes. Oncogene 2015;34:3640-50.
2. Schmidt EaS, F.W. Methods of Enzymatic Analysis. Weinheim: Verlag Chemie, 1983.
3. Bensadoun A, Weinstein D. Assay of proteins in the presence of interfering materials. Anal Biochem 1976;70:241-50.
4. Dalton AJ. A chrom-osmium fixative for electron microscopy. Anatomical Record 1955;121:281.
5. Diakopoulos KN, Lesina M, Wormann S, et al. Impaired autophagy induces chronic atrophic pancreatitis in mice via sex- and nutrition-dependent processes. Gastroenterology 2015;148:626-638 e17.
6. **McWhorter FY, Wang T,** Nguyen P, et al. Modulation of macrophage phenotype by cell shape. Proc Natl Acad Sci U S A 2013;110:17253-8.
7. **Noll EM, Eisen C**, **Stenzinger A, Elisa Espinet**, et al. CYP3A5 mediates basal and acquired therapy resistance in different subtypes of pancreatic ductal adenocarcinoma. Nat Med 2016;22:278-87.
8. Schlitter AM, Jesinghaus M, Jager C, et al. pT but not pN stage of the 8th TNM classification significantly improves prognostication in pancreatic ductal adenocarcinoma. Eur J Cancer 2017;84:121-129.
9. **Muckenhuber A, Berger AK**, Schlitter AM, et al. **Christoph Springfeld, and Wilko Weichert**. Pancreatic Ductal Adenocarcinoma Subtyping Using the Biomarkers Hepatocyte Nuclear Factor-1A and Cytokeratin-81 Correlates with Outcome and Treatment Response. Clin Cancer Res 2018;24:351-359.
10. Stenzinger A, Endris V, Klauschen F, et al. High SIRT1 expression is a negative prognosticator in pancreatic ductal adenocarcinoma. BMC Cancer 2013;13:450.

Author names in bold designate shared co-first authorship

Supplementary Figure 1: Relating to Figure 1.

(A) GFP-LC3 and CK19 immunofluorescence of *A5;Kras* mice expressing transgenic *GFP-LC3*; white arrowhead indicates diffuse GFP-LC3 staining; nuclei are detected with DAPI. (B) Macroscopic and microscopic appearance of pancreata from 18-week old *Atg5* deficient (*A5;Kras*) and *Atg5* heterozygous mice (*A5+/-;Kras*) compared to 18-week old *Atg5* proficient mice (*Kras*); oncogenic Kras is expressed in all groups of mice. (C) Pancreas/Body weight ratio in 4-/9-/18/ and more than 18-week old *Kras*, *A5+/-;Kras*, and *A5;Kras* mice (n≥3). (D) Quantification of Acinar-to-Ductal Metaplasia (ADM) per High Power Field (HPF) in 4-week old *Kras*, *A5+/-;Kras*, *A5;Kras* mice (n≥4). (E) Quantification of PanIN-1/-2/-3 per High Power Field (HPF) in 9-/ 18-week old *Kras*, *A5+/-;Kras*, and *A5;Kras* mice (n≥3). (F) Kaplan-Meier survival curve of *Kras* (n=54), *A5+/-;Kras* (n=13), and *A5;Kras* (n=24) mice (Median survival 475, 451, 184 days respectively; ***P<0.0001 comparing *Kras* and *A5;Kras*). Mean±SD, *P<0.05, **P<0.01, ***P<0.001. Scale bars equal 50μm.

Supplementary Figure 2: Relating to Figure 2.

Colony formation assays in *Kras* and *A5+/-;Kras* cells after (A) 10% FCS cultivation, (B) 6-AA (6-Aminonicotinamide), (C) Rotenone, (D) Galactose/ Glutamine, and (E) high glucose treatment. Graphs are shown on the left, representative pictures on the right. Mean±SD (n=3).

Supplementary Figure 3: Relating to Figure 3.

(A) Representative macroscopic and microscopic pictures of pancreatic tumors from wildtype mice after orthotopic transplantation (TP) of *Kras* and *A5+/-;Kras* cells; primary tumors are shown on the top, tumors formed after transplantation in the fourth picture from the top, and CK19 immunohistochemistry on the bottom; Quantification of primary pancreatic tumor burden in mice after orthotopic transplantation of *Kras* and *A5;Kras* cell lines (% area of tumor tissue, n>3) (bottom). (B) Representative macroscopic and microscopic pictures of metastasis (lung, LN=lymph node, spleen) after TP of *A5+/-;Kras* cells into wildtype mice; white arrowheads indicate metastasis (top); metastasis incidence (%) after TP of *Kras* and *A5+/-;Kras* cells (n≥5) (bottom). (C) Representative macroscopic picture of wildtype mice after tail vein (i.v.) injection of *Kras* and *A5+/-;Kras* cells (left), and quantification of body weight in male and females (n≥3) (right). (D) H&E picture of liver and spleen metastasis after i.v. of *A5+/-;Kras* cells; asterisks indicate metastasis (top); representative bright field pictures of *Kras* and *A5+/-;Kras* cells isolated from the lung of wildtype mice after i.v.; asterisk and circle indicate two different cell populations (bottom). (E) Colony formation assay in *Kras*, *A5+/-;Kras*, and *Kras* cells after 58, 94% knockdown (KD) of *Atg5* (n>3) (left); representative pictures are shown (right); cells were cultivated in medium with 10% FCS. Mean±SD, **P*<0.05. Scale bars equal 50µm.

Supplementary Figure 4: Relating to Figure 4.

(A) Classification of significantly enriched gene sets into categories, based on Transcription Factor Binding Motif database for *Kras* (left) and *A5+/-;Kras* (right) cells; pie charts show classification and tables highlight examples of enriched pathways (NES≥1.0, $P<0.05$; *P* value 0.0 indicates $P<0.001$). (B) GSEA diagrams of significantly enriched KEGG pathways found in *Kras* (top) and *A5+/-;Kras* (bottom) cells. (C) Heat map of most highly regulated genes identified by GSEA in *Kras* and *A5+/-;Kras* cells.

Supplementary Figure 5: Relating to Figure 5.

(A) Analysis of phospho-AMPKa, AMPKa, phospho-S6, mitochondrial complexes (COX I, COX II/IV, ATP Core 2), SOD2, and BiP in protein lysates and *Xbp1* splicing (*Xbp1u*=unspliced, *Xbp1s*=spliced) in RNA-preparations from *Kras* and *A5+/-;Kras* cells; β-Actin and *cyclophilin* were used as loading controls. (B) Coupling efficiency (%) of mitochondria in *Kras* and *A5+/-;Kras* cells as measured by seahorse (n≥30). (C) qRT-PCR of *Sod1* and *Nrf2* in mRNA extracts from *Kras* and *A5+/-;Kras* cells; data are normalized to *cyclophilin* (n=3). Mean±SD.

Supplementary Figure 6: Relating to Figure 6.

(A) Proportions of *Kras* and *A5+/-;Kras* cells producing Ca2+ responses after stimulation with 0.01% or 0.05% FBS (n>170). (B) Cathepsin B (CTSB) extracellular activity (% extracellular activity versus total activity) as measured from supernatants of *Kras* and *A5+/-;Kras* cells (n=15). (C) Western blot analysis of Pro-cathepsin B (Pro-CTSB), Pro-cathepsin D (CTSD), and Pro-cathepsin L (Pro-CTSL) in supernatants of *Kras* and *A5+/-;Kras* cells. (D) Colony formation assay in *Kras* and *A5+/-;Kras* cells after cultivation with E64d. (E) Illustration of lysosome-associated DNA copy number gain (red) or loss (blue) (TCGA data) in normal pancreas versus pancreatic ductal adenocarcinoma (PDAC) samples (log2 copy number units). Mean±SD.

Supplementary Figure 7: Monoallelic loss of *Atg5* induces pro-tumorigenic inflammation.

(A) Cytokine profile expression shown by immunoblotting of protein lysates from *Kras* and *A5+/-;Kras* supernatants (left); quantification of average pixel intensity between two dots corresponding to the same cytokine; numbers above graph correspond to dot-position in plot (n=1). (B) Quantification of M1 and M2 macrophages (% of all macrophages) according to their morphology after stimulation with supernatants from *Kras* and *A5+/-;Kras* cells (n≥3); representative bright field pictures are shown indicating morphology of undifferentiated (asterisk), M1 (white arrowhead), and M2 (black arrowhead) macrophages (left); Arginase-1 immunofluorescence in macrophages after stimulation with supernatants from *Kras* and *A5+/-;Kras* cells; nuclei are detected with DAPI (right). (C) Representative immunohistochemistry pictures of F4/80 and CD206 in primary tumors from *Kras* and *A5+/-;Kras* mice (top); quantification of F4/80 and CD206-positive macrophages (% positive nuclei) in *Kras* and *A5+/-;Kras* primary tumors (n>3). (D) Immunohistochemical quantification of F4/80-positive cells per high power field (HPF) in the lungs of mice after i.v. with *Kras* and *A5+/-;Kras* cells (n=20) (left); representative F4/80 and Arginase 1 (Arg1) immunohistochemistry in tissue sections from the lungs of mice after tail vein injection (i.v.) with *Kras* and *A5+/-;Kras* cells; black arrowheads indicate F4/80-positive macrophages (right). (E) Quantification of lung metastasis (% area) after tail vein injection of *A5+/-;Kras* cells into PBS or clodronate-treated wildtype mice (n>3) (left); representative H&E pictures of the lung and F4/80 immunohistochemistry pictures of the spleen after the respective treatments. Mean±SD, **P*<0.05, ***P*<0.01, ****P*<0.001. Scale bars equal 50µm.

Supplementary Table 1: PDAC and Metastasis in *A5+/-;Kras* mice

List of *A5+/-;Kras* mice that were used for Pancreatic Adenocarcinoma (PDAC) and metastasis quantification; mouse number (ID), Gender, Age (days), PDAC incidence, Histology, liver/ lung/ diaphragm metastasis, ascites incidence, and other abnormalities are presented; Male=M, Female=F, Yes=Y, No=N, Ductal=D, Undifferentiated=U, lymph node infiltration=LN, Spleen infiltration=Spl, Kidney infiltration=Kd

ID	Gender	Age	PDAC	Histology	Liver	Lung	Diaphragm	Ascites	Others
7135	F	698	Y	D	N	N	N	N	
9138	F	293	Y	D	Y	N	N	N	LN
9137	F	340	Y	D	Y	Y	Y	Y	LN
9384	F	453	Y	D	Y	Y	Y	Y	Spl
2835	M	389	Y	U	N	N	N	N	
M5683	M	133	N	N	N	N	N	N	
M5681	M	346	Y	D	Y	Y	Y	Y	LN
M5617	F	385	Y	D	N	Y	N	N	
M5618	M	451	Y	D	N	Y	Y	N	
M5551	M	578	Y	D	Y	Y	N	Y	LN
P642	M	673	Y	D	Y	N	Y	Y	LN/Spl/Kd
M6215	F	451	N	N	N	N	N	N	

Supplementary Table 2: Human pancreatic cancer patient cohort (postoperative, Cohort 1).

List of the analyzed human pancreatic cancer samples for ATG5-western blot (n=67), collected from the MTBIO tissue bank of the Institute of Pathology at the Technical University Munich. Histology (Pancreatic Ductal Adenocarcinoma (PDAC)), extent of primary tumor (T), lymph node infiltration (N), metastasis (M), tumor differentiation grade (G), survival (months), ATG5 protein expression normalized to β-Actin and quantified by ImageJ (ATG5), and Tumor stage are shown. Samples marked with red or containing an X were not used in the analysis. The last 4 samples did not have patient data and were excluded from the study.

Histology	T	N	M	G	Survival	ATG5	Stage
PDAC	4	1	1	3	13	1.035	IV
PDAC	3	1	1	3	12	0.304	IV
PDAC	3	1	1	3	9	0.460	IV
PDAC	3	1	1	3	11	0.030	IV
PDAC	3	1	1	2	7	0.000	IV
PDAC	4	1	0	3	9	0.472	III
PDAC	4	1	0	3	12	0.144	III
PDAC	4	1	x	2	17	0.369	III
PDAC	4	1	x	2	5	0.294	III
PDAC	3	1	0	4	13	0.529	III
PDAC	3	1	0	3	26	0.624	IIB
PDAC	3	1	x	3	10	0.554	IIB
PDAC	3	1	x	3	29	0.685	IIB
PDAC	3	1	x	3	29	0.698	IIB
PDAC	3	1	0	3	7	0.873	IIB
PDAC	3	1	0	3	4	0.769	IIB
PDAC	3	1	0	3	5	0.016	IIB
PDAC	3	1	0	3	3	0.488	IIB
PDAC	3	1	0	3	lost to FU	0.621	IIB
PDAC	3	1	0	3	10	0.491	IIB
PDAC	3	1	0	3	4	0.526	IIB
PDAC	3	1	0	3	14	1.308	IIB
PDAC	3	1	0	3	9	0.966	IIB
PDAC	3	1	0	3	17	1.005	IIB
PDAC	3	1	0	3	11	0.428	IIB
PDAC	3	1	0	3	lost to FU	0.838	IIB
PDAC	3	1	0	3	lost to FU	0.042	IIB
PDAC	3	1	0	2	3	0.380	IIB
PDAC	3	1	0	2	29	0.382	IIB
PDAC	3	1	0	2	25	0.350	IIB
PDAC	3	1	0	2	34	0.649	IIB
PDAC	3	1	0	2	46	0.548	IIB
PDAC	3	1	0	2	31	0.758	IIB
PDAC	3	1	0	2	lost to FU	0.167	IIB

PDAC	3	1	0	2	10	0.115	IIB
PDAC	3	1	0	2	40	0.157	IIB
PDAC	3	1	0	2	3	0.964	IIB
PDAC	3	1	x	2	13	0.258	IIB
PDAC	3	1	x	2	10	0.255	IIB
PDAC	3	1	0	1	24	0.777	IIB
PDAC	3	1	0	1	56	0.210	IIB
PDAC	3	1	X		14	0.535	IIB
PDAC	2	1	0	1	23	0.101	IIB
PDAC	1	1	0	3	60	0.047	IIB
PDAC	3	0	0	3	4	0.805	IIA
PDAC	3	0	0	3	31	0.461	IIA
PDAC	3	0	x	3	18	0.486	IIA
PDAC	3	0	x	3	8	0.539	IIA
PDAC	3	0	0	3	76	2.504	IIA
PDAC	3	0	0	3	10	0.653	IIA
PDAC	3	0	0	3	lost to FU	0.502	IIA
PDAC	3	0	0	2	32	0.911	IIA
PDAC	3	0	x	2	21	0.303	IIA
PDAC	3	0	0	2	10	0.052	IIA
PDAC	3	0	x	2	39	0.388	IIA
PDAC	3	0	0	2	36	0.298	IIA
PDAC	3	0	0	2	30	1.674	IIA
PDAC	3	0	0	2	18	0.572	IIA
PDAC	3	0	0	2	lost to FU	0.405	IIA
PDAC	3	0	x	1	23	0.747	IIA
PDAC	3	0	x	1	34	0.181	IIA
PDAC	2	0	0	3	lost to FU	0.533	IB
PDAC	2	0	0	2	23	0.098	IB
PDAC						0.848	
PDAC						0.006	
PDAC						0.312	
PDAC						0.493	

Supplementary Table 3: Human pancreatic cancer patient cohort (palliative/ metastatic, Cohort 2).

List of the analyzed human pancreatic cancer samples for ATG5-immunohistochemistry (n=26). Each row represents one individual diagnosed with PDAC (Pancreatic Ductal Adenocarcinoma, as mentioned beneath the headline Histology) and exhibiting distant metastasis (M1, i.e., HEP=hepatic, PER=peritoneal, SKI=skin, ADR=adrenal). Patients were resected between 2008 and 2013 at the University Hospital Heidelberg. ATG5 protein was detected by immunohistochemistry; membranous ATG5 was scored according to the percentage and intensity of positive cells on a 0 to 3+ scale (negative as score 0, faint expression as score 1+, moderate expression as score 2+ and strong expression as score 3+). The sum score is provided in the second column. Patients without ATG5 score were excluded from the analysis.

Histology	ATG5	M1
PDAC	2.3	HEP, PER
PDAC	3	HEP
PDAC		HEP
PDAC	2.8	HEP
PDAC	1	HEP
PDAC		HEP, PER, ADR
PDAC		HEP
PDAC	2.9	HEP
PDAC		HEP
PDAC	2	PER
PDAC	2	PER
PDAC	2.8	PER
PDAC	3	HEP
PDAC	2.1	HEP
PDAC	1.8	HEP
PDAC	2.5	HEP
PDAC	2	SKI
PDAC	2.9	HEP
PDAC	1.9	HEP
PDAC		HEP
PDAC		HEP
PDAC	3	HEP
PDAC	2.1	HEP
PDAC		SKI
PDAC	3	HEP
PDAC	3	HEP

Supplementary Table 4: Human pancreatic cancer patient cohort (postoperative, Cohort 3).

List of the analyzed human pancreatic cancer samples for ATG5-immunohistochemistry (n=134). Each row represents one individual diagnosed with PDAC (Pancreatic Ductal Adenocarcinoma) at the Charité University Hospital Berlin. Event of death (yes=1, no=0), Survival (days), lymph node status (pN), metastasis status (pM), tumor stage (pT), patient characteristics (gender, age), UICC tumor staging, and resection margin (R) are shown. ATG5 protein was detected by immunohistochemistry; membranous ATG5 was scored according to the percentage and intensity of positive cells on a 0 to 3+ scale (negative as score 0, faint expression as score 1+, moderate expression as score 2+ and strong expression as score 3+). The sum score is provided in the first column. Patients without death event and no registered survival were removed from the analysis.

ATG5	Death	Survival	pN	pM	pT	Gender	Age	Stage	R
2.7	1	431	0	0	2	w	74	Stage I	0
2	1	898	1	0	2	w	75	Stage IIB	0
1	0		0	0	3	w	64	Stage IIA	0
2.7	0	5748	1	0	3	w	56	Stage IIB	1
3	1	278	1	0	3	m	47	Stage IIB	0
1	1	780	1	0	2	m	67	Stage IIB	0
3	1	407	1	0	3	w	62	Stage IIB	0
2.4	1	452	1	1	3	m	31	Stage IV	1
3	1	1166	1	0	2	w	63	Stage IIB	0
2.5	1	215	0	0	2	w	58	Stage I	0
3	1	629	1	0	2	m	53	Stage IIB	1
2.8	1	329	1	0	3	w	62	Stage IIB	0
2.8	1	46	0	0	2	w	61	Stage I	0
2.9	1	406	1	0	3	m	69	Stage IIB	0
2.1	1	236	0	0	2	w	70	Stage I	1
2.6	0	2459	0	0	2	w	71	Stage I	
2.6			1	0	2	m	64	Stage IIB	0
2.2	1	862	1	0	2	w	64	Stage IIB	0
2.3	1	448	1	0	2	m	71	Stage IIB	0
2.5	0	2302	1	0	2	m	64	Stage IIB	
3	1	287	1	0	3	w	47	Stage IIB	1
3	0	305	1	0	3	m	62	Stage IIB	
1.3	1	945	1	0	3	w	75	Stage IIB	0
2.2	1	832	1	0	3	w	62	Stage IIB	0
2.9	1	685	0	0	3	w	59	Stage IIA	
1.2			1	0	3	m	50	Stage IIB	0
2	1		1	0	2	m	60	Stage IIB	
1.3	0	2049	0	0	3	m	63	Stage IIA	0
2.2			1	0	3	m	66	Stage IIB	0
2.9	1	1045	1	0	3	w	49	Stage IIB	0
2.9	0	2104	0	0	2	w	64	Stage I	0
3	1	1743	1	0	2	m	71	Stage IIB	0
2.2			1	0	3	w	59	Stage IIB	0
1.2	0		0	0	3	m	59	Stage IIA	0

2.9	1	744	1	0	3	w	73	Stage IIB	1
3	1	740	1	0	3	m	50	Stage IIB	0
3	1	1258	0	0	3	w	62	Stage IIA	0
2.5	1	809	1	0	3	w	61	Stage IIB	0
3	1	167	1	0	3	m	66	Stage IIB	0
2	1	348	1	0	3	w	59	Stage IIB	1
2.2	1	911	1	0	3	m	64	Stage IIB	0
2.5	1	779	0	0	3	w	69	Stage IIA	0
2.9	1	471	0	0	2	w	76	Stage I	0
2.3	1	125	1	0	3	m	63	Stage IIB	0
2.2	0	1427	0	0	3	m	65	Stage IIA	1
3	1	395	0	0	3	m	60	Stage IIA	0
1.2	1		1	0	2	w	77	Stage IIB	
3	1		1	0	3	m	38	Stage IIB	
2	1		1	0	3	w	76	Stage IIB	1
3	0		1	0	3	m	63	Stage IIB	1
3			1	0	3	w	65	Stage IIB	0
2.6	1	432	0	0	2	w	69	Stage I	0
2.7	1	805	1	0	3	m		Stage IIB	
2.2	0	2644	0	0	3	w	62	Stage IIA	
3	1	496	1	0	3	w	79	Stage IIB	
2.8	1	198	1	0	3	m	49	Stage IIB	0
3	1		1	0	3	m	70	Stage IIB	
3	1	404	1	0	3	m	73	Stage IIB	
2.8	1		0	0	3	w	77	Stage IIA	
2	1	902	1	0	3	w	73	Stage IIB	
2.8	1	112	1	1	3	m	55	Stage IV	0
3	1	715	1	0	3	m	64	Stage IIB	0
3	1	209	1	0	3	w	51	Stage IIB	0
2.8	1	260	1	0	3	m	51	Stage IIB	0
3	1	353	1	0	3	w	67	Stage IIB	0
3	0		1	0	3	m	48	Stage IIB	
1.8	1	611	1	0	3	w	78	Stage IIB	0
2.9	1	98	1	0	3	w	63	Stage IIB	0
2.7	1	28	0	0	3	w	74	Stage IIA	1
2.7	0	2645	1	0	2	m	53	Stage IIB	0
2	0		0	0	2	w	59	Stage I	0
3	0	2609	1	0	3	m	69	Stage IIB	0
2.8	1		1	0	3	m	72	Stage IIB	0
2.8	1	255	1	0	3	m	74	Stage IIB	0
3	1		0	0	3	m	78	Stage IIA	0
2.9	1	184	0	0	4	w	72	Stage III	0
3	1	291	1	0	3	w	69	Stage IIB	0
3	0	1273	0	0	3	m	56	Stage IIA	0
3	1	1183	0	0	3	m	50	Stage IIA	0
2.6	1	96	1	0	3	w	75	Stage IIB	1
3	1		1	0	3	m	57	Stage IIB	0
0.7	1		1	0	4	w	70	Stage III	0
3	1	1064	1	0	3	m	72	Stage IIB	1
2	1	288	1	0	3	w	61	Stage IIB	0
2.8	1	192	1	0	4	m	57	Stage III	1
2.8	1	370	1	0	3	w	74	Stage IIB	0
2.9	1	1186	1	0	3	w	72	Stage IIB	0
3	1	394	0	0	3	m	69	Stage IIA	1

3	0	17	1	0	3	w	68	Stage IIB	1
1	1	369	0	0	3	w	79	Stage IIA	1
2.8			1	0	3	w	62	Stage IIB	1
2.8	0	7	1	0	3	m	60	Stage IIB	1
3	1	59	1	0	3	w	61	Stage IIB	1
3	1	289	1	0	4	m	60	Stage III	1
3			1	0	3	m	70	Stage IIB	0
2.2			0	0	1	m	66	Stage I	0
3	1	222	1	0	3	m	61	Stage IIB	1
2.05	0	415	0	0	3	w	81	Stage IIA	0
3	1	653	1	1	3	w	46	Stage IV	0
2	1	12	1	0	4	m	69	Stage III	1
3			1	0	3	m	59	Stage IIB	1
2.8	0	12	1	0	3	m	67	Stage IIB	0
2.8	1	205	1	0	3	m	69	Stage IIB	1
3			1	0	4	m	73	Stage III	0
2.5	1	615	1	0	3	m	54	Stage IIB	1
2.3	1	263	1	0	3	m	67	Stage IIB	1
2.7			0	0	3	m	65	Stage IIA	0
2	1	915	0	0	3	m	68	Stage IIA	0
3			1	0	3	m	75	Stage IIB	0
2	1	316	1	0	3	m	64	Stage IIB	0
3	1		1	0	2	m	73	Stage IIB	0
1.8	0	1079	1	0	3	w	59	Stage IIB	0
3	1	455	1	0	3	m	56	Stage IIB	0
2.7	0	210	1	0	3	m	43	Stage IIB	1
1.2	1	603	1	0	3	w	58	Stage IIB	1
2.8	0	865	1	0	3	w	57	Stage IIB	0
2.3			1	0	3	m	77	Stage IIB	1
3	0	311	1	0	3	m	61	Stage IIB	0
2.3	1	199	1	1	3	m	41	Stage IV	0
2.9	0	866	0	0	3	m	75	Stage IIA	0
2.2	1	582	1	0	3	m	75	Stage IIB	0
2.1			1	0	3	w	75	Stage IIB	1
2.3	1	265	1	0	4	m	74	Stage III	1
2	0	696	1	0	3	w	66	Stage IIB	0
2.2	1	185	1	0	3	m	51	Stage IIB	1
2.1	1	268	1	0	3	w	81	Stage IIB	0
2.9	0	586	0	0	3	m	69	Stage IIA	0
1.5	0	5	0	0	3	w	69	Stage IIA	0
2.2	1	1104	1	0	3	w	68	Stage IIB	0
2.6	1	324	1	0	3	w	68	Stage IIB	1
2.2	1	380	1	0	3	m	58	Stage IIB	0
2.3	1	249	1	0	3	w	63	Stage IIB	0
2.3	1	166	1	0	3	m	72	Stage IIB	0
2.8	1	216	1	0	3	m	55	Stage IIB	1